Thin film growth of layered transition metal dichalcogenides, boron nitride and microscopic investigation of thermoelectric and Heusler compound

A Thesis Submitted for the Degree of

Doctor of Philosophy

in the Faculty of Science

by

Badri Vishal

CHEMISTRY AND PHYSICS OF MATERIALS UNIT
INTERNATIONAL CENTRE FOR MATERIALS SCIENCE
JAWAHARLAL NEHRU CENTRE FOR ADVANCED SCIENTIFIC RESEARCH
(A Deemed University)
Bangalore – 560064, INDIA.
December 2019

Dedicated to

My Grandparents

DECLARATION

I hereby declare that the thesis entitled "**Thin film growth of layered transition metal dichalcogenides, boron nitride and microscopic investigation of thermoelectric and Heusler compound**" is an authentic record of research work carried out by me at the Chemistry and Physics of Materials Unit, International Centre for Materials Science, Jawaharlal Nehru Centre for Advanced Scientific Research, Bangalore, India under the supervision of **Prof. Ranjan Datta** and that it has not been submitted elsewhere for the award of any degree or diploma.

In keeping with the general practice in reporting scientific observations, due acknowledgment has been made whenever the work described is based on the findings of other investigators. Any omission that might have occurred due to oversight or error in judgment is regretted.

_____

Badri Vishal

CERTIFICATE

Certified that the work described in this thesis titled "**Thin film growth of layered transition metal dichalcogenides, boron nitride and microscopic investigation of thermoelectric and Heusler compound**" has been carried out by Mr. **Badri Vishal** at the Chemistry and Physics of Materials Unit, International Centre for Materials Science, Jawaharlal Nehru Centre for Advanced Scientific Research, Bangalore, India under my supervision and that it has not been submitted elsewhere for the award of any degree or diploma.

_____

Prof. Ranjan Datta

(Research Supervisor)

Acknowledgements

I take this opportunity to sincerely thank my research supervisor Dr. Ranjan Datta for his constant motivation, guidance and encouragement throughout my Ph.D. His endless enthusiasm for science and hardworking nature has inspired and motivated me at various times.

I sincerely thank Prof. C. N. R. Rao for creating world class facilities at International Centre for Materials Science (ICMS). I specially thank him for providing aberration corrected transmission electron microscope facility at this centre that gave me an excellent opportunity to learn and carry out research on advanced microscopy techniques.

I would like to express my gratitude to Prof. Kanishka Biswas for enthusiastic scientific collaborations and providing high quality Thermoelectric ($Sn_{1-x}Sb_xTe$) that greatly helped my research. I also thank Prof. C. N. R. Rao, Prof. Chandrabhas Narayana, Prof. S. C. Peter and Prof. U. Ramamurty, for fruitful collaborations.

I would like to specially thank all the researchers, Dr. MB Sreedhara, Dr. A. Banik, Dr. V. Rajaji, Dr. S. C. Sarma, and Mr. A. Chaturvedi, for collaborating and for their valuable discussions.

I would like to take this opportunity to specially thank Prof. Umesh V. Waghmare for Computational Materials Science course, Prof. S.M. Shivaprasad for the course on physics of materials, Prof. A Sundaresan for the course on Chemistry physics of materials, and Dr. Ranjan Datta for the course on Transmission Electron Microscopy. These course helped me a lot during my Ph.D.

I thank the past and present chairman of Chemistry and Physics of Materials Unit, Prof. G. U. Kulkarni and Prof. S. Balasubramanian, Prof. Chandrabhas Narayana, and Prof. A Sundaresan for all their invaluable support.

I would like to thank the entire faculty at JNCASR for being a constant source of inspiration with their advanced research. I take this opportunity to thank all my past teachers at school and college level for sharing their knowledge, providing their support and encouragement without which it is impossible for me to be here.

I take this opportunity to thank my past and present labmates, Dr. Loukya, Dr. Dileep, Dr. D. S. Negi, Dr. Rajib, Ms. Usha, Ms. Sharona, Mr. Rajendra, Mr. Ankit sharma, and Mr. Arindam Mukherjee for their useful discussions and creating a cheerful environment.

I extend my gratitude to all the efficient staff at the Library, Academic and Administration sections for their timely help and cooperation.

I would like to thank the Hostel staff, Mess workers, for the homely environment and tasty food during my stay at JNCASR.

I acknowledge and thank all my friends inside and outside JNCASR for their immense support and being with me at all the times. Specially thanks to Akash K Singh and Abhijit Chatterjee.

I finally acknowledge and thank all my family members for their unconditional love, support and encouragement. I am lucky to have wonderful mother Meera Devi and father Rameshvar Prasad. I specially thank my sister Dr. Anubha Jaiswal and brother HariOm Vikash jaiswal and, for their constant support. And my grandparents late. Mrs. Champa Devi and late. Mr. Banarasi lal Jaiswal for unconditional love beyond words.

Last but not the least; I thank God Almighty for showering all his blessings upon me at every point of life and helping me in completing this thesis work. It is impossible for me to be here today without His blessings.

Synopsis

The thesis deals with the epitaxial thin film growth of 2D materials and their hetero-structures, microstructural characterization of Sn-Sb-Te based thermoelectric material and Ni-Mn-Sn based Heusler compound. Chapter 1 is brief introduction and important results to the various contents of the thesis.

In Chapter 2 the controlled growth of MoS_2, WS_2, and ReS_2 epitaxial thin films by pulsed laser deposition (PLD) is presented. Layer number of TMDs can be controlled by the laser pulse duration. Sapphire substrate is found to introduce compressive stress in the layer resulted in increase in band gap in both MoS_2 and WS_2. In case of ReS_2 the growth is found to be vertical and film quality improves significantly while growing on MoS_2 template. In Chapters 3, the epitaxial growth of various of van der Waals heterostructure (vdWs) between TMDs and BN is described. In case of heterostructure between similar TMDs an intense peak around 2.3 eV is observed and is explained due to transition between valence band of BN to conduction band of TMDs. For heterostructure between two different TMDs the intense peaks are split to two and three for two and three different TMDs, respectively. Chapter 4 describes the results on metastable epitaxial *w*-BN thin film by PLD with hardness of 37 GPa. The formation of this metastable w-BN is due to preferential chemical interaction between O atom of sapphire and B atom of BN inducing staggering in the layer leading to w-BN. Chapter 5 contains a detailed study of microstructural features of low thermal conducting thermoelectric $Sn_{1-x}Sb_xTe$. The observation is made on the presence of superlattice structures due to interaction between Sb in Sn site and Sb in Te site in this system responsible for low thermal conductivity. The observation is supported based on density functional theory-based calculation. In Chapter 6, thin film growth of $Ni_{50}Mn_{37/35}Sn_{13/15}$ Heusler alloy, microstructural investigation by HRTEM and magnetic characteristics by HREELS are described. The presence of non-magnetic phases is confirmed by HREELS measurement. A future perspective is provided in Chapter 7.

List of Publications

1. **B Vishal**, R Sahu, U Bhat, R Datta, Investigation of microstructural details in low thermal conducting thermoelectric $Sn_{1-x}Sb_xTe$ alloy, *Journal of Applied Physics*, ***122 (5),*** *055102 (2017).*

2. **B Vishal**, R Singh, A Chaturvedi, A Sharma, MB Sreedhara, R Sahu, U Bhat, U Ramamurty, R Datta, Chemically stabilized epitaxial wurtzite-BN thin film, *Superlattices and Microstructures* ***115****, 197-203 (2018).*

3. **B Vishal,** H Sharona, U Bhat, A Paul, MB Sreedhara, V Rajaji, S C Sarma, C Narayana, S C Peter, R Datta Growth of epitaxial ReS_2 thin film by pulsed laser deposition, *Thin Solid Films* ***685,*** *81–87 (2019).*

4. **B Vishal,** U Bhat, H Sharona, A Mukherjee, S Roy, S C Peter, R Datta, Microstructural and magnetic properties of epitaxial Ni50Mn37/35Sn13/15 Heusler alloy thin films grown by pulsed laser deposition, *Manuscript Under review, Journal of Crystal Growth (2020).*

5. **B Vishal**, U. Bhat, H. Sharona, A. Mukherjee and R. Datta, Heterostructures of hetero-stack of 2D TMDs (MoS2, WS2 and ReS2) and BN, *Manuscript under review, Bulletin of Materials Science (2020).*

6. A Banik, **B Vishal**, S Perumal, R Datta, K Biswas, The origin of low thermal conductivity in $Sn_{1-x}Sb_xTe$: Phonon scattering via layered intergrowth nanostructures, *Energy & Environmental Science* ***9 (6),*** *2011-2019 (2016).*

7. MB Sreedhara, S Gope, **B Vishal**, R Datta, AJ Bhattacharyya, CNR Rao, Atomic layer deposition of crystalline epitaxial MoS_2 nanowall networks exhibiting superior performance in thin-film rechargeable Na-ion batteries, *Journal of Materials Chemistry A* ***6 (5),*** *2302-2310 (2018).*

8. H Sharona, **B Vishal**, U Bhat, A Paul, A Mukherjee, S C Sarma, S C Peter and R Datta, Rich diversity of crystallographic phase formation in 2D $Re_xMo_{1-x}S_2$ ($x < 0.5$) alloy, *Journal of Applied Physics **126** (22), 224302 (2019).*

9. U Bhat, R Singh, **B Vishal**, A Sharma, H Sharona, R Sahu, R Datta, Distinct Photoluminescence in Multilayered van der Waals Heterostructures of $MoS_2/WS_2/ReS_2$ and BN , *Physica status solidi (b) **255** (7), 1700691 (2018).*

10. H Sharona, B Loukya, U Bhat, R Sahu, **B Vishal**, P Silwal, A Gupta, R Datta, Coexisting nanoscale inverse spinel and rock salt crystallographic phases in $NiCo_2O_4$ epitaxial thin films grown by pulsed laser deposition, *Journal of Applied Physics **122** (22), 225301 (2017).*

11. R Sahu, D Radhakrishnan, **B Vishal**, DS Negi, A Sil, C Narayana, R Datta, Substrate induced tuning of compressive strain and phonon modes in large area MoS_2 and WS_2 van der Waals epitaxial thin films, *Journal of Crystal Growth, **410,** 69 (2015).*

12. R Sahu, U Bhat, Nitin M Batra, H Sharona, **B Vishal**, S Sarkar, S AAravindh, S C Peter, I S Roqan, PMFJ Costa, R Datta Nature of low dimensional structural modulations and relative phase stability in $Re_xMo(W)_{1-x}S_2$ transition metal dichalcogenide alloys , *Journal of Applied Physics **470**, 51-57 (2017).*

13. R Sahu, HB Gholap, G Mounika, K Dileep, **B Vishal**, S Ghara, R Datta, Stable p-type conductivity in B and N co-doped ZnO epitaxial thin film, *Physica status solidi (b) **253** (3), 504-508 (2016).*

14. **B Vishal**, R Sahu, R Datta Substrate induced tuning of compressive strain and phonon modes in large area MoS_2 and WS_2 van der Waals epitaxial thin films, *EMSI 2017 Conference Proceedings, **M1,** (2017).*

Contents

Chapter 1

Introduction

This chapter is a brief introduction with important results to the various contents of the thesis. The thesis comprises of epitaxial thin film growth of TMDs and their heterostructures, w-BN epitaxial thin film growth, characterization of superlattice structure in SnTe based thermoelectric material and thin film growth and magnetic phase characterization by HR-EELS of NiMnSn Heusler alloy.

1.1 Epitaxial growth of 2D-TMDs and heterostructures of TMDs and BN

Two-dimensional van der Waals (vdW) materials are a new class of material with immense possibility in the field of ultra-thin transistor, optoelectronic devices and various energy conversion related application [1-4]. Atomically thick 2D layered materials generated immense research interest since the discovery of graphene [3-4]. Due to zero band gap in Graphene the attention shifted towards MoS_2, WS_2, ReS_2 belonging to the family known as layered transition metal dichalcogenides (TMDs) [3-6]. On the other hand, vdW heterostructures emerge as new class of advanced materials by stacking various combination of 2D materials either on top of each other (vertical heterostructure) or zipping at the edges (in-plane heterostructure) [7-8]. This provides an opportunity to tailor the property of such 2D materials beyond the expected opportunities. Coupled quantum wells (CQW) which is supposed to host indirect excitons may also be realized based on such heterostructure system [8]. However, most of the fundamental properties based on 2D-TMDs have been investigated based on mechanically exfoliated and chemically synthesized materials, where dimensions of materials are small and not suitable for the large area practical device fabrication. Therefore, many attempts have been made with various physical crystal growth techniques to grow such vdW materials epitaxially over large area [9-13]. In chapter 2 and 3 we describe the use of PLD growth technique to grow such 2D TMDs and their heterostructure over large area (5×5 mm^2).

Chapter 2 and 3 describe the results on large area epitaxial growth of individual TMDs and heterostructures between TMDs and *h*-BN by pulsed laser deposition (PLD) [11-13]. Results on layer controlled growth of MoS_2 and WS_2 epitaxial thin films by PLD are presented in Chapter 2. Complete control over number of layers including monolayer is achieved by PLD utilizing slower growth kinetics. Sapphire substrate is found to introduce compressive stress in the layer resulted in increase in band gap in both MoS_2 and WS_2. In the case of ReS_2 the growth is found to be vertical and film quality improves significantly while growing on MoS_2 template. [11-12]. In Chapters 3, the epitaxial growth of various of vdW heterostructures between TMDs and BN is presented. The layer numbers of TMDs and BN spacer can be controlled by PLD. The crystal structure of BN in between TMDs depends on the particular TMDs used to grow BN. Photoluminescence (PL) spectra is dominated by peak at 534 nm (2.32 eV) and 580 nm (2.13 eV) for homo-stacks and for hetero stacks heterostructures respectively [13] and this is attributed to

the transition between valence band of BN to conduction band of MoS2 at K-point of Brillouin zone [13].

1.2 Epitaxial *wurtzite* -BN thin film on sapphire substrate

Wurtzite-BN (w-BN) is new advance material with extraordinary properties such as hard material, ultra-wide band gap with thermal and chemical resistant [14-15]. *w*-BN exhibits ultra-high band gap semiconductor with indirect band gap of 5.72 eV (Γ→X), and have potential application in deep UV range optoelectronics, microelectronic and mechanical tooling industry [13,16-17]. Wurtzite form of BN is metastable and requires extreme temperature (1730-3230 °C) and pressure (5-18 GPa) condition to stabilize the phase [15]. Chapter 4 describes results on the formation of epitaxial *w*-BN thin film on sapphire substrate by PLD. This is an accidental finding while growing heterostructures between TMDs and *h*-BN. The formation of such phase of BN is unpredictable under relatively much lower temperature (800 °C) and pressure (10^{-5} torr) condition [14-15]. Detailed investigation by HRTEM and DFT calculation show that preferential chemical interaction between O atom of sapphire and B atom of planar *h*-BN lattice induces staggering in the layer *h*-BN structure which thus mimics along the growth direction to form *w*-BN structure [18]. In terms of practical importance, the hardness of *w*-BN is next to diamond and in many application superior to the diamond.

1.3 Energy material : SnTe based thermoelectric

Harvesting electrical energy from the waste heat will immensely contribute towards environmental preservation [19]. More than two-thirds of the industrial energy is wasted as heat. Thermoelectric materials can directly convert waste heat into electrical power and have attracted significant attention for electricity generation through waste heat recovery [19-20]. SnTe is best alternative for lead-free PbTe, with identical electronic structures and thermoelectric power generation [21]. In chapter 5 we describe results on the microstructure characterisation by HRTEM and its role on the thermoelectric property of $Sn_{1-x}Sb_xTe$ (x = 0.04, 0.08, 0.15) alloys. Sb is found

to replace both Sn site as well as both Te and Sn site. The areas where Sb replace both Sn and Te sites form super structure which is distinct than a regular nanostructure phase usually attributed for high thermoelectric performance [22]. Theory calculation suggests that while regions where Sb replaces regular Sn site gives rise to large thermopower, the areas with superstructure contributes to low lattice thermal conductivity and combined results increases *z*T to ~1.

1.4 Room Temperature magnetic refrigeration

Room Temperature (RT) magnetic refrigeration are essentials and have vital role in cooling technologies, which is energy-efficient and environmentally benign without greenhouse gas emission [23]. Magnetocaloric effect (MCE) for refrigeration and magnetic shape memory effect (SME) for reversibility are essential for RT magnetic refrigeration [24]. For RT application $Ni_{50}Mn_{37}Sn_{13}$ and $Ni_{50}Mn_{35}Sn_{15}$ Heusler alloy have attracted considerable research attention due to large inverse MCE with entropy change (ΔS) of 18 and 15 $JKg^{-1}K^{-1}$ at 299 and 187 K, respectively [25]. For many practical device applications, thin film form of the alloy is required e.g., in magnetic cooling, actuators, sensors, micro-electromechanical system (MEMS) etc. [25-26]. In chapter 6 the results on $Ni_{50}Mn_{37}Sn_{13}$ and $Ni_{50}Mn_{35}Sn_{15}$ epitaxial alloy thin films with two different compositions grown on *c* plane sapphire substrate by pulsed laser deposition are described. The epitaxial relationship between untransformed $L2_1$ and sapphire is α-Al_2O_3 $[01\bar{1}0] \parallel L2_1$ $[011]$. The Curie temperatures of the films are 316 and 334 K, respectively. The microstructure of the films consists of untransformed austenite ($L2_1$) and three different martensite with $L1_0$, $4O$ and $5M$ structures [27]. The relative volume fractions of four predominant phases are ~ 50, 40, 5 and 5 %, respectively at room temperature for both the films. The epitaxial $L2_1$ phase grows under tensile strain on sapphire (0001) substrate and favours the formation of predominantly $L1_0$ over other martensite phases below the transition temperature. The interface between various untransformed and transformed phases are found to be coherent. The overall experimental magnetization of the thin films is comparable the theoretical values. Local HREELS spectra of Mn and Ni $L_{3,2}$ absorption edges confirm the presence of some non-magnetic phases in the structure particularly in $4O$ and $5M$ form of martensite might account for the observed differences with the theoretical value [27].

1.5 Bibliography

[1] K. Fai Mak, C. Lee, J. Hone, J. Shan, T. F. Heinz , Phys. Rev. Lett. 10**5,** 136805(4) (2010).

[2] M. Xu, T. Liang, M. Shi, H. Chen, Chem. Rev. **113,** 3766-3798 (2013).

[3] A. K. Geim, K. S Novoselov, Nat. Mater. **6**, 183−191 (2007).

[4] A. K. Geim, I. V. Grigorieva, Nature **499,** 420 (2013).

[5] M. Rahman, K. Davey, S.Z. Qiao, Adv. Funct. Mater. **27**, 1606129 (2017).

[6] S. Tongay, H. Sahin, C. Ko, A. Luce, W. Fan, K. Liu, J. Zhou, Y.-S. Huang, C.-H. Ho, J. Yan, D. F. Ogletree, S. Aloni, J. Ji, S. Li, J. Li, F.M. Peeters, J. Wu, Nat. Commun **5**, 3252 (2014).

[7] F. Withers, O. Del Pozo-Zamudio, A. Mishchenko, A. P. Rooney, A. Gholinia, K. Watanabe, T. Taniguchi, S. J. Haigh, A. K. Geim, A. I. Tartakovskii & K. S. Novoselov, *Nat. Mater.* **14**, 301 (2015).

[8] E. V. Calman,C. J. Dorow, M. M. Fogler, L. V. Butov, S. Hu, A. Mishchenko and A. K. Geim, Appl. Phys. Lett. **108**, 101901 (2016).

[9] Y. Zhan, Z. Liu, S. Najmaei, P. M. Ajayan, and J. Lou, Small **8,** 966 (2012).

[10] Y. Zhan, Z. Liu, S. Najmaei, P. M. Ajayan, and J. Lou, Small **8,** 966 (2012).

[11] R. Sahu, D. Radhakrishnan, B. Vishal, D. S. Negi, A. Sil, C. Narayana, R. Datta, J. Cryst. Growth **470,** 51–57 (2017).

[12] B. Vishal, H. Sharona, U. Bhat, A. Paul, M. B. Sreedhara, V. Rajaji, S. C. Sarma, C. Narayana, S. C. Peter, and R. Datta, Thin Solid Films, **685,** 81–87 (2019).

[13] U. Bhat, R. Singh, B. Vishal, A. Sharma, S. Horta, R. Sahu, R. Datta, Phys. Status Solidi B **255,** 1700691(2018).

[14] F. P. Bundy, R. H. Wentorf Jr, J. Chem. Phys. **38**, 1144-1149 (1963).

[15] V. L. Solozhenko, D. Häusermann, M. Mezouar, M. Kunz, Appl. Phys. Lett. **72**, 1691-1693 (1998).

[16] N. Izyumskaya, D. O. Demchenko, S. Das, Ü. Özgür, V. Avrutin, H. Morkoç, Adv. Electron. Mater. **3,** 1600485 (2017).

[17] M. Topsakal, E. Aktürk, S. Ciraci, Phys. Rev. B **79**, 115442 (2009).

[18] B. Vishal, R. Singh, A. Chaturvedi, A. Sharma, M.B. Sreedharaa, R. Sahu, U. Bhat, U. Ramamurty, and R. Datta, Superlattices and Microstructures, **115**, 197-203 (2018).

[19] K. Biswas, J. He, I.D. Blum, C.I. Wu, T.P. Hogan, D.N. Seidman, V.P. Dravid, M.G. Kanatzidis, Nature 489, 414 (2012).

[20] G. Tan, L.-D. Zhao, and M. G. Kanatzidis, Chem. Rev. **116,** 12123 (2016).

[21] R. Brebrick and A. Strauss, Phys. Rev. **131,** 104 (1963).

[22] B. Vishal, R. Sahu, U. Bhat and R. Datta, J. Appl. Phys , **122(5)**, 055102 (2013).

[23] O. Gutfleisch, M. A. Willard, E. Brück, C. H. Chen, S. Sankar, and J. P. Liu, Adv. Mater. **23,** 821 (2011).

[24] Y. Zhang, L. Zhang, Q. Zheng, X. Zheng, M. Li, J. Du, and A. Yan, Sci. Rep. **5,** 11010 (2015).

[25] T. Krenke, E. Duman, M. Acet, E. F. Wassermann, X. Moya, L. Mañosa, and A. Planes, Nat. Mater. **4,** 450 (2005).

[26] Z. Wang, E. Guo, C. Tan, X. Tian, W. Cai, and J. Zhu, RSC Adv. **7,** 42866 (2017).

[27] B. Vishal, U. Bhat, H. Sharona, A. Mukherjee, S. Roy, S. C. Peter, and R. Datta, Manuscript Under review, J. Cryst. Growth (2020).

Chapter 2

Epitaxial growth of 2D-TMDs (MoS_2, WS_2 and ReS_2) thin films by PLD

This chapter describes the epitaxial thin film growth of 2D-TMDs, e.g, MoS_2, WS_2 and ReS_2 by pulsed laser deposition (PLD). The films are grown on c-plane sapphire substrate for MoS_2 and WS_2 and both c-plane sapphire and MoS_2 template for ReS_2. The results show that it is possible to grow MoS_2 and WS_2 thin film with control over layer thickness under slower kinetic growth condition. In the case of ReS_2, the growth orientation is vertical on both sapphire and MoS_2 template.

This work has been published in the following documents:

1. ***B. Vishal,*** *H. Sharona, U. Bhat, A. Paul, M. B. Sreedhara, V. Rajaji, S. C. Sarma, C. Narayana, S. C. Peter, and R. Datta, Thin Solid Films,* ***685****, 81–87(2019).*
2. ***B. Vishal****, R. Sahu, and R. Datta, EMSI 2017 Conference Proceedings* ***M01****.*
3. *R. Sahu, D. Radhakrishnan,* ***B. Vishal*** *, D. S. Negi, A. Sil, C. Narayana and R. Datta, Journal of Crystal Growth* ***470,*** *51–57 (2017).*

2.1 Introduction

Atomically thick two-dimensional layer materials generated immense research interest since the discovery of graphene [1-6]. Graphene revealed many unique physical phenomena e.g., linear band structure with momentum, ballistic transport [7-10] and superior chemical catalytic activities etc. [11, 12]. However, graphene is a zero band gap material and the need to open a band gap for practical device application shifted the attention towards MoS_2, WS_2 and similar materials belonging to the family known as layered transition metal dichalcogenides (TMDs) [13, 14]. MoS_2 and WS_2 have various allotropes (2H, 1T, 3R, etc.) but commonly found as 2H phase. ReS_2 also belongs to 2D-TMDs [1-2, 15-17]. But, monolayer structure of ReS_2 is Peierls distorted $1T_d$ (space group: $P\bar{1}$) where four Re atoms are hybridized together to form 2D quasi-periodic superstructure. Schematic Crystal structure of 2H MoS_2, 2H WS_2, and $1T_d$ ReS_2 are shown in Figure 2.01. The lattice parameters of the bulk 2H MoS_2 are a = 3.18 Å and c = 12.85 Å [18]. The lattice parameters of $1T_d$ ReS_2 are: a = 6.41 Å, b = 6.47 Å, c = 6.42 Å, $\alpha = 91.32°$, $\beta = 105.49°$ and $\gamma = 119.03°$ [18,19]. Layer specific band gaps of MoS_2 and ReS_2 are shown in Figure 2.02. MoS_2 and WS_2 exhibit the band gap changes fundamentally from direct to indirect as monolayer to bulk, respectively. MoS_2 shows indirect band gap of 1.27 eV for multilayer and direct band gap of 1.98 eV monolayer [18]. Similarly WS_2 indirect to direct band gap of for 1.29 eV to 1.96 eV for multilayer to monolayer, respectively [20]. However, for ReS_2 the band gap remains direct in more than mono layer form [16]. The band gap of ReS_2 is 1.52 and 1.42 eV in monolayer and multilayer form, respectively [18]. This has been attributed to weak interlayer van der Waals coupling ~18 meV compared to 460 meV in case of MoS_2 [Figure 2.03.(a)] [17]. Due to distorted crystal structure ReS_2 exhibits linearly polarized Excitons and in plane electrical anisotropy shown in Figure 2.03.(b) &(c)] [21-22]. This is beneficial in many applications where retention of the optical direct band gap is desired in two or few layers form of such materials.

Most of the fundamental properties based on this system are investigated primarily on mechanically exfoliated and chemically synthesized materials [23-26] where dimensions of materials are small and are not suitable for large area practical device fabrication. Therefore, many attempts have been made to grow such van der Waals (vdW) materials epitaxial over large area [24-35]. Most of the epitaxial layer growth reported was only in the nano or micrometer length scale along with special treatment of substrate and the application of strain was performed by

external means. For example, large area CVD growth of MoS_2 thin films was reported on SiO_2 substrate [26, 36-38].

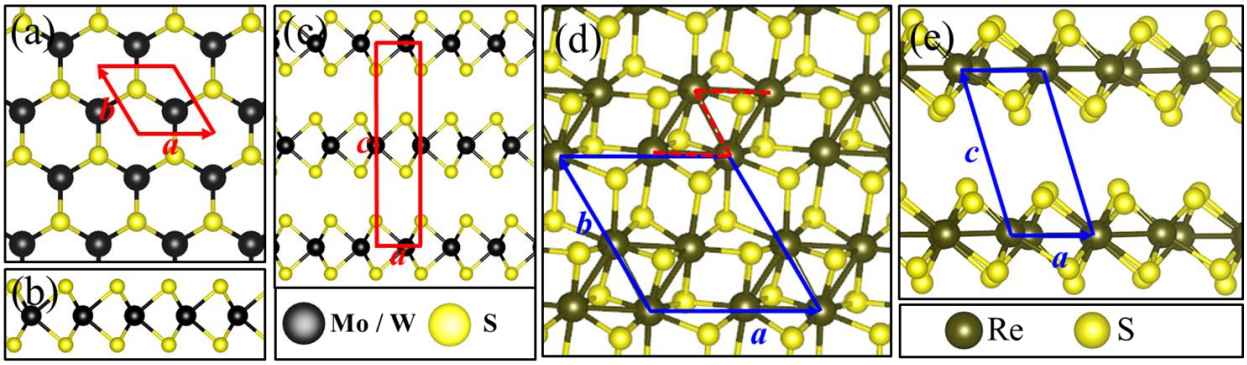

Figure 2.01. *Schematic Crystal structure of (a) monolayer 2H-MoS_2 along <0001>, (b) <11$\bar{2}$0> and (c) Bernal stacking in bulk 2H-MoS_2 along <11$\bar{2}$0>. Schematic Crystal structure of 1T_d ReS_2 (d) along <0001> Z.A., and (e) along <11$\bar{2}$0> Z. A. The lattice parameters of 1T_d ReS_2 are: a = 6.41 Å, b = 6.47 Å, c = 6.42 Å, α = 91.32°, β = 105.49° and γ = 119.03°. Copyright by 2016 AIP Publishing [18]. Copyright by 2019 Elsevier [59].*

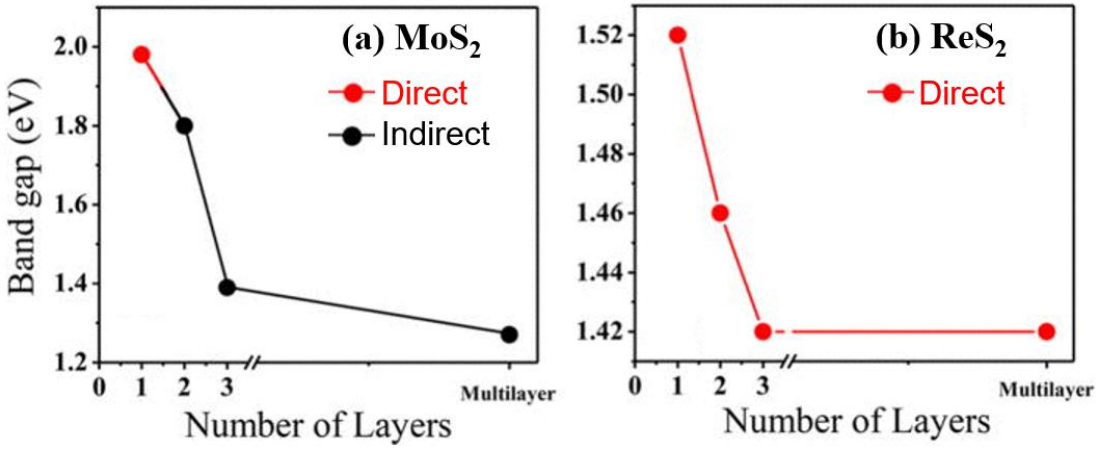

Figure 2.02. *Layer specific plots of band gaps of (a) MoS_2 and (b) ReS_2. Note the direct to indirect band gap crosses for MoS_2 from monolayer to bilayers. Copyright by 2016 AIP Publishing [18].*

Similar fabrication also done by atomic layer deposition (ALD) of MoS_2 and WS_2 is done by Z. Jin *et al.* and T. W. Scharf *et al.* and electrochemical exfoliation by Liu *et al.* shown in Figure 2.04. [26, 39-40].Control over the number of layers was achieved by the duration of oxygen plasma

treatment of SiO_2 substrate. Oxygen plasma treatment was believed to increase the interaction between the MoS_2 and SiO_2 substrate and helps in further growth of subsequent layers [36].

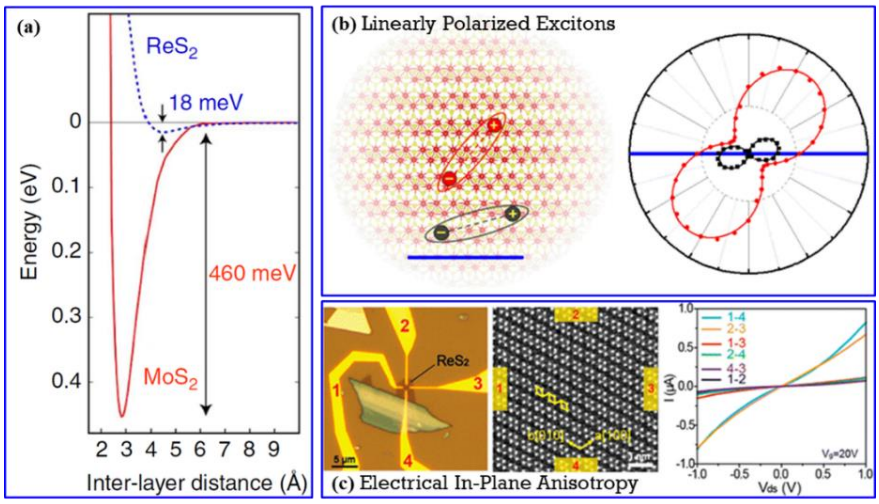

Figure 2.03. *(a) ReS_2 exhibits weak interlayer van der Waals coupling ~18 meV compared to 460 meV in case of MoS_2. Copyright by 2014 Springer Nature [17] (b) distorted crystal of ReS_2 is responsible for linearly polarized Excitons and Copyright by 2015 American Chemical Society [21], and (c) in-plane electrical anisotropy. Copyright by 2015 American Chemical Society [22]*

ReS_2 has potential applications in low dimensional electronics, optoelectronics, energy storage, and catalytic hydrogen production. Ultra-thin 2D materials provide an opportunity to overcome the issues associated with the continuous demand on the miniaturization of transistors. ReS_2 based thin film transistors, field effect transistors (FET), digital logic devices, and photodetectors have been demonstrated [41-43]. Due to its inherent modulated structure, ReS_2 exhibits anisotropic optical and electrical properties. ReS_2 bulk crystal is already in use as polarization dependent photodetectors exploiting its optical anisotropic property [16, 18, 42].

Orientation dependent photo current has been demonstrated in ReS_2 which is promising in integrating electronic and optical devices e.g., as phototransistor part of an integrated circuit [43]. The Maximum anisotropic ratio of 3.1 is reported in ReS_2 based FET devices with competitive values of current on-off ratio and low subthreshold swing [41, 44]. ReS_2 can be used as an efficient photocatalyst. *ab initio* calculations show that both mono and multilayer ReS_2 are stable and efficient photocatalyst for water splitting [45]. ReS_2 supported on carbon is found to be a promising

electrocatalyst for hydrogen evolution reaction (HER) and suggested that perpendicular orientation of ReS_2 flake will improve the performance further [46-47].

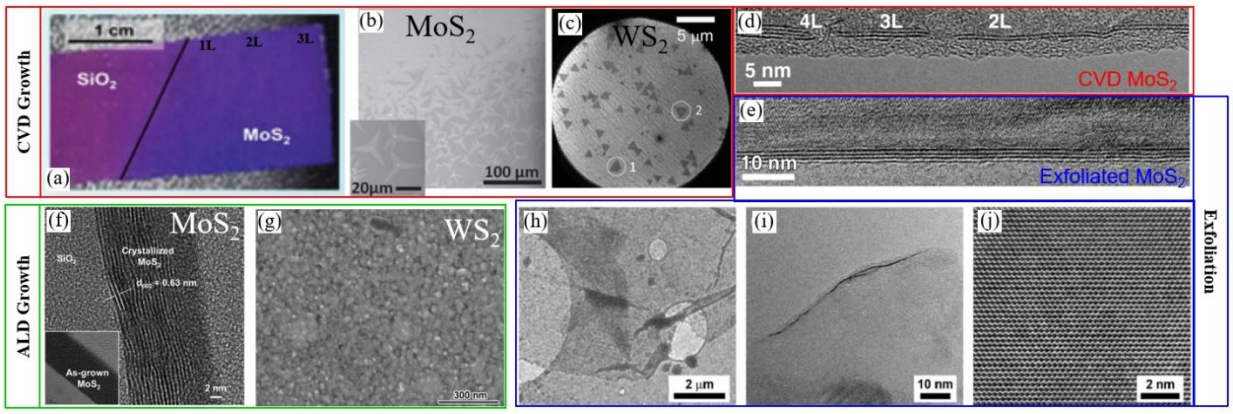

Figure 2.04. *2D-materials and its heterostructure for practical applications requires large area epitaxial growth. For example, here's some from the literature towards this effort. (a-d) Chemical vapor deposition Copyright by 2015 The Royal Society of Chemistry [36]. Copyright by 2012 WILEY-VCH Verlag GmbH & Co. KGaA, Weinheim [37]. Copyright by 2014 American Chemical Society* [38]. *(f-g) atomic layer deposition. Copyright by 2014 The Royal Society of Chemistry* [39].*Copyright by 2004 Materials Research Society* [40]. *And (h-j) electrochemical exfoliation. Copyright by 2014 American Chemical Society* [25]

Therefore, to exploit the unique properties of ReS_2 in device applications, development of growth procedures in the form of large area (commercial substrate scale) mono and few layers is required. Monolayer and few layers of ReS_2 can be synthesized by both bottom-up methods such as chemical vapor deposition (CVD), atomic layer deposition (ALD), pulsed laser deposition (PLD), physical vapor deposition (PVD) and top-down methods such as mechanical, chemical and liquid exfoliations techniques [48-51]. However, the exfoliation methods poses challenges on controlling the dimension of flakes, contamination or residues of exfoliation agents and misalignment in stacking between two or more similar or different types of TMDs while fabricating the heterostructures [16, 52]. For device application, it is important to deposit 2D materials and their heterostructures by crystal growth techniques over large area uniformly [2, 19,53-59]. There are already reports on such attempts to grow large area ReS_2 thin film by physical

and chemical deposition techniques. In this context, ReS_2 was grown by CVD on Si/SiO_2 substrate at 450°C with a mean crystal size of 40 µm. Ammonium per-rhenate and sulphur were used as precursors and argon as carrier gas. Depending upon the temperature of the growth, various size and thickness of the crystal is obtained. The nucleation of the secondary layer is initiated at the centre of the primary crystal and subsequent growth proceeded towards the edge [17]. Te assisted ReS_2 growth was performed in a CVD reactor at 700 °C. Te helps in lowering the melting point (3180 °C) of Re thus enhances its incorporation, which is not the problem with other components with relatively lower melting points [18]. ReS_2 was grown by CVD on a flexible glass substrate at 450 ºC in the absence of catalyst [60]. The ReO_3 powder was used as a precursor which was sulphurized by H_2S for 30 min. Large area uniform ReS_2 thin film was grown by CVD on mica substrate at 600 ºC under ambient pressure. Re metal powder and Re_2S_7 were used as precursors. Re_2S_7 is volatilized above 300ºC, and partial sulphurization provides nucleation sites on the substrate for the subsequent growth of ReS_2. Chemically inert mica substrate reduces nucleation density, atom migration and prevents vertical growth of ReS_2 compared to SiO_2 substrate where growth is predominantly vertical [61, 62]. The film grown on mica substrate grows with optimum flat morphology below 700 ºC and start forming amorphous domains at temperature below 500 ºC. Few layers centimeter scale continuous ReS_2 film was grown on SiO_2/Si substrate by PVD using ReS_2 powder as source material [63]. The ReS_2 film was grown by ALD over large area (5 sq. cm) on Al_2O_3 coated Si (100) substrate at wide temperature range between 120-500 °C. The morphology of films was rough containing both horizontal (*c* plane) and tilted vertical domains. The perpendicular orientation of ReS_2 was found to be beneficial for HER and Li, Li-S batteries though for device application flat orientation is required [47, 64-66].

Direct to indirect crossover occurs for monolayer MoS_2 with applied strain of 1% [67]. On the other hand, application of bi-axial compressive strain was shown to increase the band gap of MoS_2 monolayer and the change in band gap is within 100 meV for every 1% of strain [68]. Nevertheless, from practical point of view it is important to grow such layered compounds epitaxial over large area with complete control over the layer thickness and at the same time inducing strain through the substrate in order to retain the modification in the electronic structure. Both the aspects of large area (we have grown on maximum 8×8 mm^2 size substrate) epitaxial film growth and retaining strained state are demanding and challenging. With this goal, in the present

report we first demonstrate that it is possible to grow epitaxial MoS_2 and WS_2 thin films by pulsed laser deposition (PLD) under slow kinetic condition on '*c*' plane sapphire substrate [69], which has some advantages over the CVD counterpart. Moreover, complete control over layer thickness is possible by this method including the growth of monolayer without requiring any special substrate treatment. The characteristics Raman mode for MoS_2 and WS_2 are different for the thin films grown on the substrate compared to the bulk suggesting the substrate induced van der Waals and long range Coulomb interaction. Most of the reports show softening of the Raman modes upon decreasing the number of layers grown on the widely used SiO_2 substrate. Among various reports on the tuning the electronic structure by strain is one where externally applied uniaxial tensile strain on a fabricated MoS_2 bending device resulted in phonon mode softening. This phonon mode softening was associated with the decrease in band gap by ~ 45 meV and ~120 meV for every 1% of strain for monolayer and bilayers MoS_2, respectively. Sapphire substrate significantly influences the two important Raman modes i.e. A_{1g} and E^1_{2g} in MoS_2 and WS_2 epitaxial thin film grown by PLD. We have observed significant stiffening of two Raman active modes i.e. A_{1g} and E^1_{2g} for MoS_2 thin film and mostly A_{1g} for WS_2 and the two modes stiffens further with decreasing layer thickness. This translates to a maximum compressive strain of 0.52 % & 0.53 % and increases the band gap to 1.73 eV and 1.68 eV for monolayer MoS_2 and WS_2, respectively and falls off with increasing the layer thickness. The HRTEM imaging from the interface directly reveals the nature of atomic registry and strain between the films and substrate. The overall results are extremely encouraging and show a practical route to engineer the phonon modes and retain the strain in such van der Waals compounds which can be exploited to tune the opto-electronic properties and fabrication of large area practical devices.

As already pointed out that from the practical device fabrication point of view, it is desirable to grow/deposit such 2D materials uniformly over a substrate with simpler methods involving less chemicals and process parameters. In this context, large area (10×10 mm^2) epitaxial growth of MoS_2 and WS_2 thin film with control over layer numbers was demonstrated by PLD [19]. In this chapter, the growth of large area (10×10 mm^2) ReS_2 thin film by PLD is investigated. The major difference between ReS_2 and with growth of MoS_2 and WS_2 by PLD is that the melting point of ReS_2 is 390 ºC which is much smaller compared to 1185 °C (1250°C) of MoS_2 (WS_2). Two different substrates were used in the present investigation: *c-plane* sapphire substrate and

MoS_2 template deposited on *c-plane* sapphire. It is found that depending on the growth temperature the film can be vertically oriented $[(0001)ReS_2 \perp (0001)Al_2O_3$ and $(0001)ReS_2 \perp (0001)MoS_2 \parallel (0001)Al_2O_3]$, a composite of vertical and poly-crystalline, and completely polycrystalline films. The quality of the layer is improved significantly when grown on MoS_2 template. Detailed structural characterizations and optical property evaluation by high resolution transmission electron microscopy (HRTEM), X-ray diffraction (XRD), Raman spectroscopy, and cathodoluminescence (CL) techniques are presented.

2.2 Experimental Methods

Thin films of MoS_2, WS_2 and ReS_2 are grown by pulsed laser deposition (PLD). Schematic of the steps of PLD shown in Figure 2.05. First the target pellet preparation of MoS_2, WS_2 will be discussed, and then ReS_2 for PLD due to low melting point compare to MoS_2 and WS_2. We have used 8×10 mm^2 size of substrate for the present study but little bigger substrate can also be used in our system. MoS_2 and WS_2 target pellets were prepared from powders obtained from Sigma Aldrich (99.9%) by first cold pressing and then sintering at 500 °C for 5 hours in a vacuum chamber (~10^{-5} Torr).

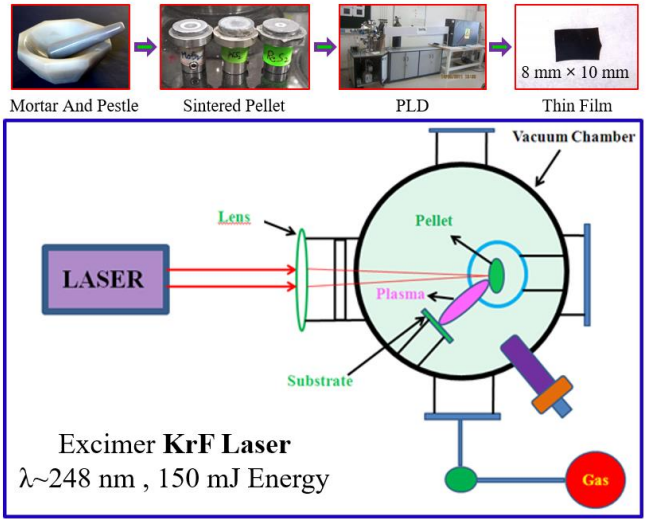

Figure 2.05. *Schematic of the steps of Pulsed Laser deposition (PLD), Where TMDs grind by mortar and pestle, then shapes as pellet and sintered. This pellet will be used as PLD target inside*

the PLD chamber where Laser (Excimer KrF Laser λ~248 nm, 150 mJ Energy) will be ablated on pellet and create plasma plume. Plasma plume will be deposited on substrate and form thin film.

The sintering under large vacuum chambers with continuously running pumps prevents oxidation of compounds as well as re-deposition of vapor species back on the pellet surface compared to sintering performed in a sealed quartz tube. This was a successful method for system containing highly volatile elements [70,71,72]. Growth was followed by three step process originally developed for ZnO but with a different temperature and kinetic settings [69]. The final growth scheme for (a) MoS_2 and WS_2 at 400 °C (b) ReS_2 and (c) ReS_2 on MoS_2 at various deposition temperature with slow kinetics of laser ablation (1Hz) shown in Figure 2.06. The temperature for nucleation layer was 400 °C with a laser ablation rate of 1 Hz. The temperature for final growth was 400 °C and at 1Hz laser ablation rate. Both the nucleation layer and slower laser frequency rate are important to obtain epitaxial large area film as we found that faster laser ablation rate leads to formation of polycrystalline MoS_2 films [19].

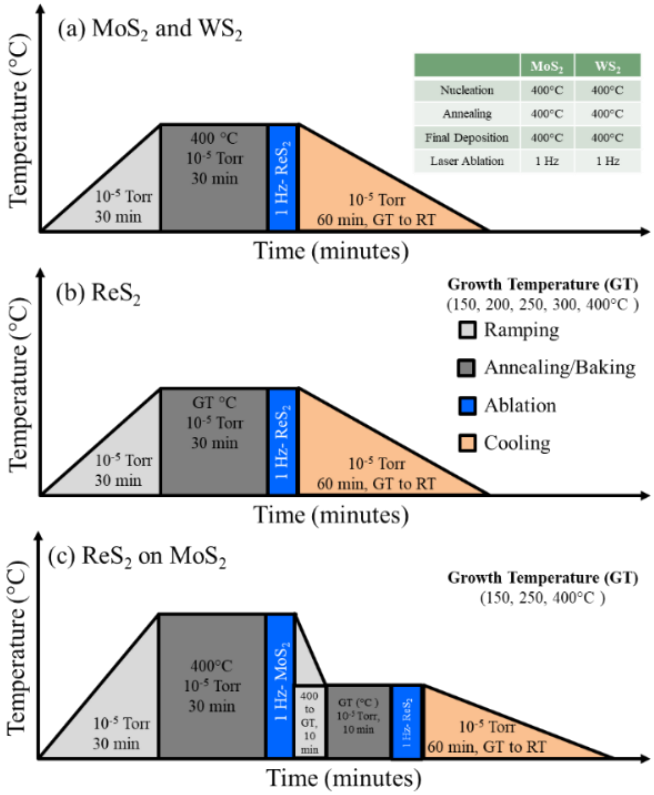

***Figure 2.06**. The final growth scheme for (a) MoS_2 and WS_2 at 400 °C (b) ReS_2 and (c) ReS_2 on MoS_2 at various deposition temperature with slow kinetics of laser ablation (1Hz).*

ReS_2 thin films were grown by PLD on two different surface; *c-plane* sapphire substrate and 20 nm thick *c-plane* MoS_2 template deposited on *c-plane* sapphire substrate following the procedure already described in Ref. 19. ReS_2 target pellet was used to ablate and grow the thin film. For the preparation of PLD target, ReS_2 compound was first synthesized by directly heating mixture of pieces of elemental Re cut from the wire (1mm diameter, 99.97%, Alfa Aesar) and S powder (-325 mesh, 99.5% Alfa Aesar) in the stoichiometry ratio (1:2) sealed in a quartz tube at 10^5 mbar pressure to 200 ºC in 15 h followed by annealing at that temperature for 2 h. The step involving slow heating was necessary to avoid possible explosion due to high vapour pressure of S. Slow ramping reduces the thermal shock between the quartz tube and heating surface. Then the temperature was increased stepwise to 400 °C and finally to 900 °C over a period of 10 h and 24 h, respectively. The sample was held at 900 ºC for 120 h to ensure homogeneity. The black powder thus obtained was then cold pressed in a die and vacuum sintered at temperature 200 °C for 4 h to prepare the PLD target. The temperature and sintering duration were comparatively lower compare to MoS_2 and WS_2 pellets due to the low melting temperature (380°C) of ReS_2. The sintering in a vacuum chamber with continuously running pump in the background prevents oxidation of compound and deposition of vapor specifics (decomposition of volatiles or surface reaction products) back on the pellet surface compared to the case for sintering performed in a sealed quartz tube. The deposition of the entire ReS_2 thin film was carried out at the same temperature and pressure (1.33×10^{-3} Pa, back ground gas is N_2) with laser ablation frequency of 1 Hz. Substrate size used was 10×10 mm^2. Slow laser ablation rate allows enough time for kinetic relaxation of the nucleation layer which helps in establishing the epitaxial relationship with the substrate thus removing misaligned crystallites. This was already demonstrated in the case of ZnO and its alloys, MoS_2 and WS_2 [19]. The ReS_2 thin film was grown at various deposition temperatures: 100 to 400 °C and is listed in the Table 3. The PLD route has advantages over CVD and PVD counterparts in the sense that the films may be free from any parasitic deposition (crystal formation in the vapor phase depositing on the substrate common to CVD or metal organic CVD processes). The method is scalable and economical [73,74].

As we know slow laser ablation rate allows sufficient time for kinetic relaxation of the nucleation layer in order to establish epitaxial relationship with the substrate thus removing misaligned crystallites. This is even more important for van der Waals compounds because the

2D-nucleations do not have any strong attachment with the underlying substrate and is relatively more mobile during the deposition compared to non-layered or three dimensional covalently bonded materials. The method described above was successful for the epitaxial growth of ZnO alloyed with Co, Mn, S and Te on sapphire [69-72]. The pressure was kept constant at ~10^{-5} Torr throughout the growth schedule. There are few recent reports on using sapphire substrate for growing TMDs films [75-77]. The PLD method of growth has some benefits over chemical vapor deposition (CVD) or physical vapor deposition (PVD) counterparts in the sense that the films will be free from any parasitic deposition. Moreover, the technique is economical and scalable even on a larger substrate than mentioned here in the present study [73,74]. The epitaxial quality of thin films is confirmed by X-ray diffraction, high resolution transmission electron microscopy and electron diffraction techniques. Raman spectra were recorded using a custom built Raman spectrometer using a 532 nm laser excitation and a grating of 1800 lines/mm at room temperature [78]. The laser power at the sample was approximately 1 mW. Micro PL (photoluminescence) measurement was performed in a state of the art LabRAM HR (UV) system. All the films were investigated by HRTEM, XRD, Raman spectroscopy, and CL techniques. HRTEM images were recorded in a double aberration corrected FEI TITAN 80-300 kV microscope [Figure 2.07.]. TEM cross-sectional specimens were prepared by first mechanical thinning to 90 μm and then tripod polishing down to 20 μm. The final thinning to perforation was carried out in a Gatan PIPs (precision Ar ion polishing system, Gatan, Inc.) operating at 4.5 kV to generate electron transparent thin area. Special care was taken during the sample preparation to prevent delamination of weak van der Waals layers from the substrate. XRD patterns were recorded in a Panalytical instrument (Empyrean diffractometer) using Cu Kα1 radiation (λ = 1.5404Å) with the scan speed of 0.006 step/second and PIXcel^{3D} solid-state hybrid pixel detector. CL measurement was done using a Gatan mono CL (serial mode) installed in a FEI quanta field emission scanning electron microscope. All the CL spectra were collected with Peltier cooled (-25ºC) photomultiplier tube (PMT) with 1 nm step size and accusation time of 0.6 s/step. Entrance and exit slits size of the spectrometer was kept at 1 mm.

Figure 2.07. *FEI TITAN^{3TM} 80-300 kV at International Centre for Materials Science (ICMS), Jawaharlal Nehru Centre for Advanced Scientific Research (JNCASR), Bangalore. It has double Cs corrector technology with both image and probe corrector systems [79].*

Cross-sectional thin film TEM samples were prepared by conventional mechanical polishing and Ar ion milling to perforation so as to obtain a large electron transparent thin area. Different steps of sample preparation are described in Figure 2.08. First step involves the face-to-face gluing of films to prepare a sandwich. The assembly is then mounted on a brass block with a temporary mounting wax having melting point of 135 ºC. The second step involves mechanical polishing along the cross-sectional direction shown in the Figure 2.08. in order to shape it to fit within 3 mm Cu grid and to reduce the thickness to below 80 µm. Mechanical polishing was done using SiC polishing papers. In the next step, the thickness is further reduced to < 20 µm using diamond polishing sheets of varying grit sizes from 30 to 6 µm. The sample is then mounted on to a copper grid and milled in the precision Ar ion polishing machine to perforation. The beam settings used were ±7° and 4 keV energy. The voltage was reduced to 3 kV at the end to remove any surface amorphous layer. Similar procedure of mechanical polishing and Ar ion milling is followed in the case of plan view sample preparation except that face-to-face gluing of the films is not done. The polishing is done from the substrate side and thinned down to < 20-30 µm before

ion milling to perforation. Here both the Ar ion gun beams are set at +7° and 4 keV with no modulation [69,79]. Special care was taken during the sample preparation as it was found that van der Waals layers can easily be detached from the substrate. The relative movement between two cross sectional pieces was made almost absent to ensure their presence on the substrate till the end of sample preparation.

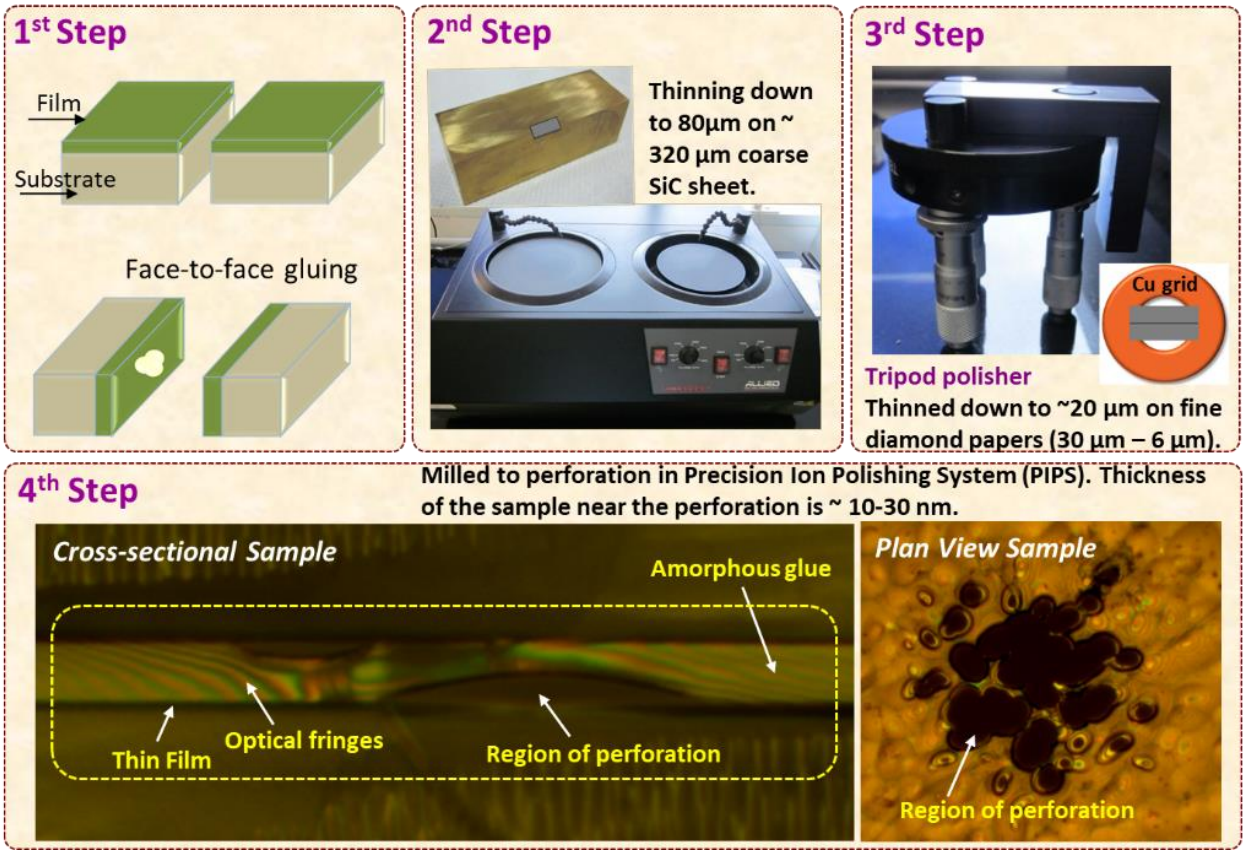

Figure 2.08. *Step-by-step procedure of thin film TEM cross-sectional sample preparation. First two steps involve face-to-face gluing and mechanical polishing of the sample to thin down to 80 µm. In the third step, sample is further thinned down to < 20 µm using a hand held tripod polisher. The sample is then mounted on copper grid and milled to perforation in a Gatan Precision Ion Polishing System (PIPS) to obtain an electron transparent thin area as shown in the figure as a part of 4th step. The optical images of both cross-sectional and plan view samples at the region of perforation are shown [79].*

2.3 Results and Discussion

2.3.1 Epitaxial growth of MoS_2 and WS_2 thin films

2.3.1.1 Structural details of MoS_2 and WS_2 thin films

We have used HRTEM imaging to confirm the formation of epitaxial film, number of layers and stacking information in addition to routinely practiced Raman spectroscopy. On the other hand, X-ray signal does not show up from such one or two layers of films, while spectra from the thick films confirms the formation of large area epitaxial film on sapphire substrate [Figure 2.10.][19].

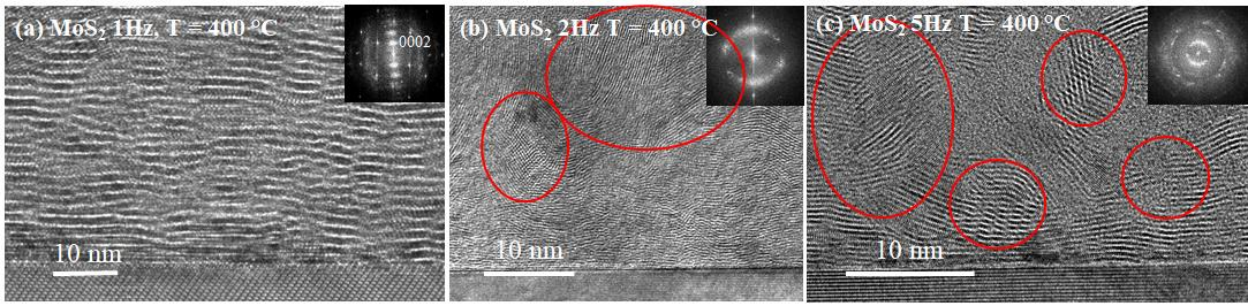

Figure 2.09. *HRTEM images showing formation of epitaxial film can only be ensured under (a) slow kinetic growth (1Hz) for growth flat and uniform growth MoS_2 , whereas in case of faster kinetics such as (b)2Hz and (c) 5 Hz of lases ablation will gives polycrystalline films . Copyright by 2017 Elsevier [19].*

TEM is extremely powerful technique and can provide information from 40-50 μm length scale considering four quadrants of the thin areas in a cross sectional TEM specimen. As already mentioned in the TEM sample preparation method, special care must be undertaken during sample preparation in order to retain the weakly held van der Waals layers on the substrate until the end.

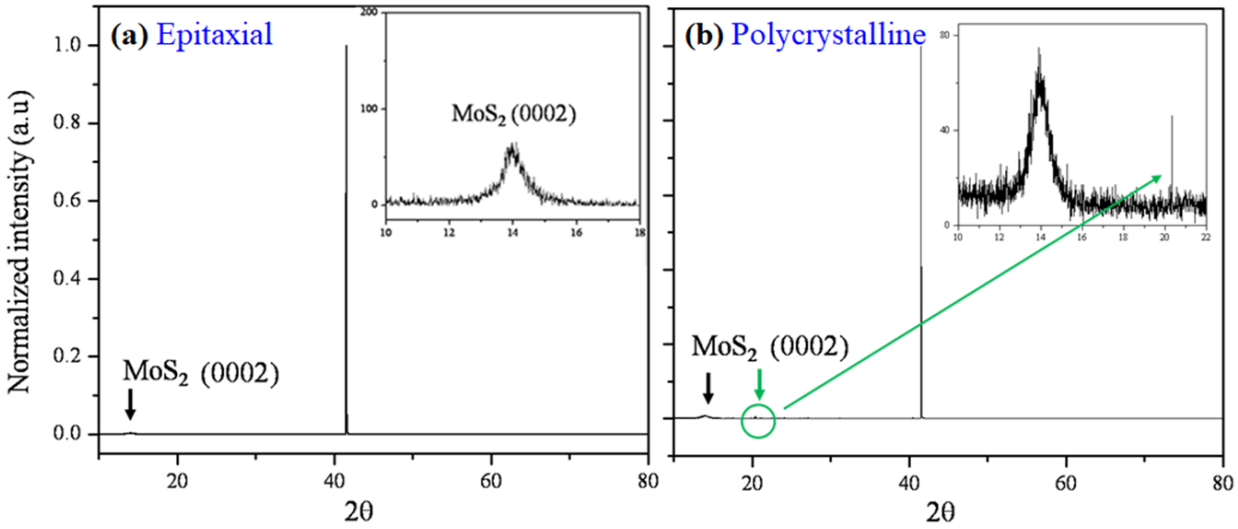

Figure 2.10. *X-ray spectra confirming the formation of (a) large area epitaxial MoS_2 thin film on c- plane sapphire. (0002) and (0004) peaks corresponding to MoS_2 and Al_2O_3 are marked. For mono layer and bilayers it was not possible to obtain a clear signal by X-ray. The reason for this is that for coherent Bragg X-ray diffraction at least few numbers of layers is required to obtain any out of plane peaks. (b) Polycrystalline MoS_2 thin film is observed in case of faster kinetics growth. Copyright by 2017 Elsevier [19].*

HRTEM images with various numbers of layers for MoS_2 films and WS_2 film are shown in Figure 2.11. and Figure 2.12.. Both the electron diffraction pattern and FFT of HRTEM images are placed in the inset for the thick films. Diffraction pattern shows <0002> spots parallel to the growth direction. Aberration corrected negative C_S imaging at the interface regions is carried out to probe the nature of layer bonding with the substrate, strain and interlayer stacking information [Figure 2.13.] [80,81]. For the thick film the stacking structure of MoS_2 and WS_2 are of 2H poly-type. It can be seen that the sapphire substrate is Al terminated and at the end it will be explained that the interaction between the periodic dangling bonds at Al atoms and bottom S layers of MoS_2/WS_2 is responsible for the substrate induced compressive strain and associated phonon mode hardening.

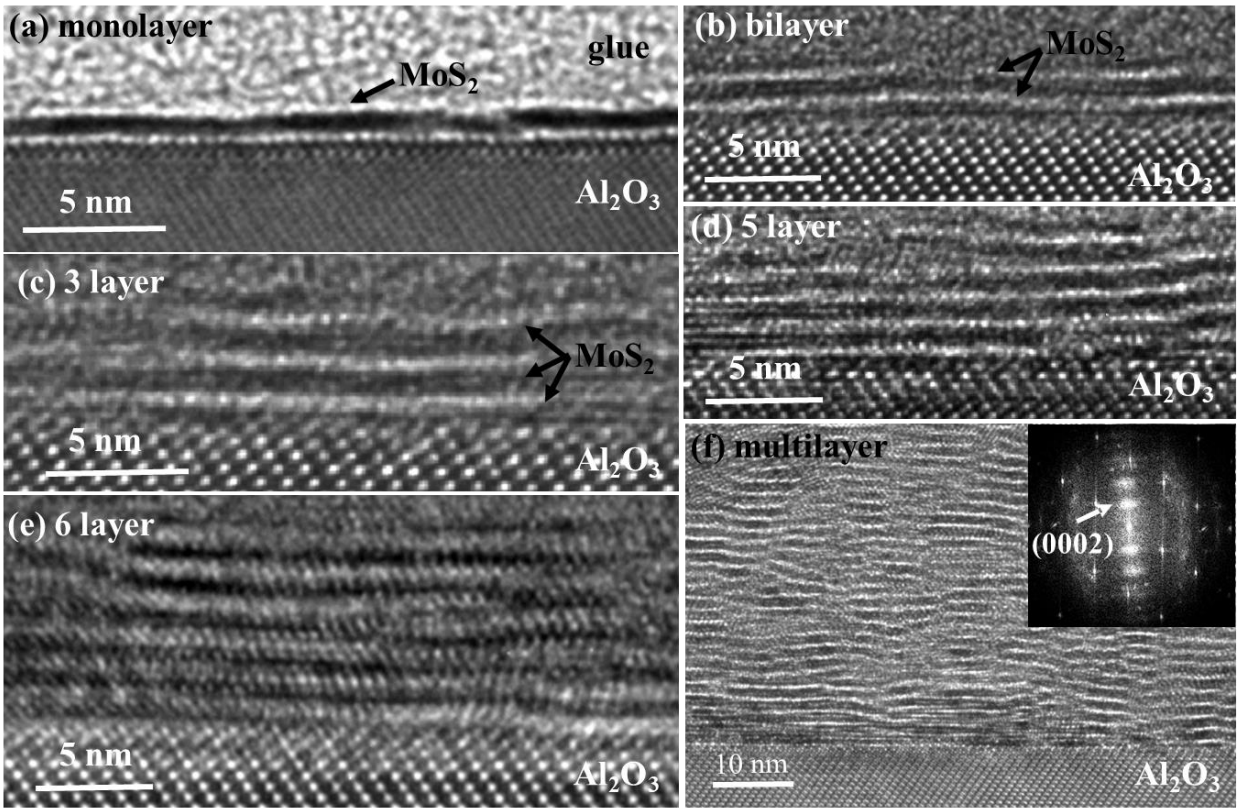

Figure 2.11. *HRTEM images showing (a) monolayer, (b) bilayers, (c) few layers, and (d) thick epitaxial films of MoS_2 on 'c' plane sapphire. Epitaxial monolayer WS_2 on 'c' plane sapphire is shown in (e). Both the electron diffraction and X-ray spectra confirm the formation of large area epitaxial thin film on sapphire. (X-ray spectra can be found in the* ***Figure 2.09****.). Copyright by 2017 Elsevier [19].*

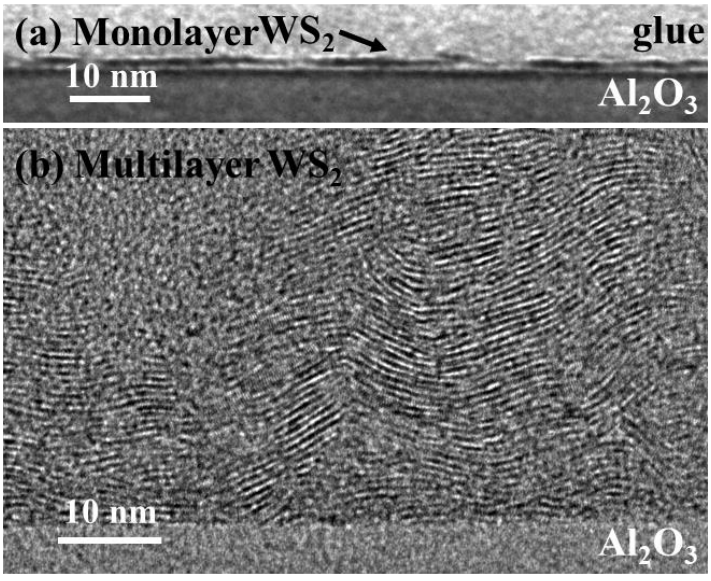

Figure 2.12. *HRTEM images Epitaxial (a) monolayer and (b) multilayer epitaxial thin films of WS_2 on 'c' plane sapphire. Copyright by 2017 Elsevier [19].*

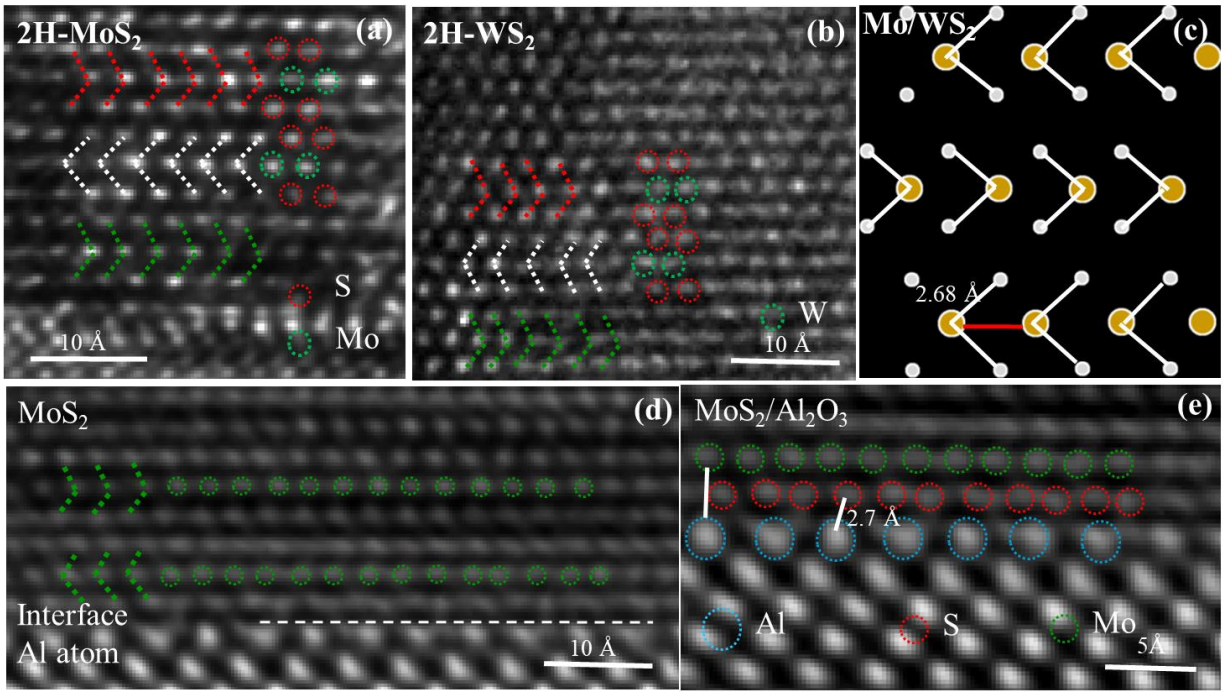

Figure 2.13. *HRTEM imaging from the interface regions of epitaxial MoS_2 and WS_2 films along $< 11\bar{2}0 >$ Z.A. of sapphire. (a) & (b) showing the 2H poly-type interlayer stacking for MoS_2 and WS_2, respectively. (d) Example image from MoS_2/sapphire interface markings atoms over a distance from place to place to derive strain information from such images. (e) Close up interface image showing that substrate is Al terminated and the typical distance between Al and S is ~ 2.7 Å. A modulated in plane S-S (marked with red dotted circle) inter-atomic distance over Al (marked turquoise dotted circle) atoms can be observed. Copyright by 2017 Elsevier [19].*

2.3.1.2 Substrate induced layer specific stiffening in E^1_{2g} and A_{1g} Raman modes

E^1_{2g} and A_{1g} Raman modes of both MoS_2 and WS_2 for different layer thickness in shown Figure 2.14.. Hardening of E^1_{2g} and A_{1g} Raman modes indicates the presence of compressive strain [82]. We have observed substrate induced compressive strain in both MoS_2 and WS_2 layers with the maximum strain present for the monolayer and the strain decreases with increasing the number of layers. Other than stiffening, systematic anomalous shift in the Raman modes are also observed as the number of layers is decreased which is consistent with the earlier reports [67]. Figure 2.14. Summarizes the shift in E^1_{2g} and A_{1g} Raman modes of MoS_2 and WS_2 as a function

of film thickness grown on '*c*' plane sapphire [Table 1 and Table 2 for tabulated numbers]. The frequency of these two phonon modes for bulk starting powder samples used to grow films in our case and the values from the literature are also listed for the comparison purpose [67]. The Raman shifts of these two modes are slightly different for the powder sample (379.9 and 405.7 cm^{-1}, Sigma Aldrich) used for the present investigation in comparison to the literature values (379.2 and 404.7 cm^{-1}) [67].

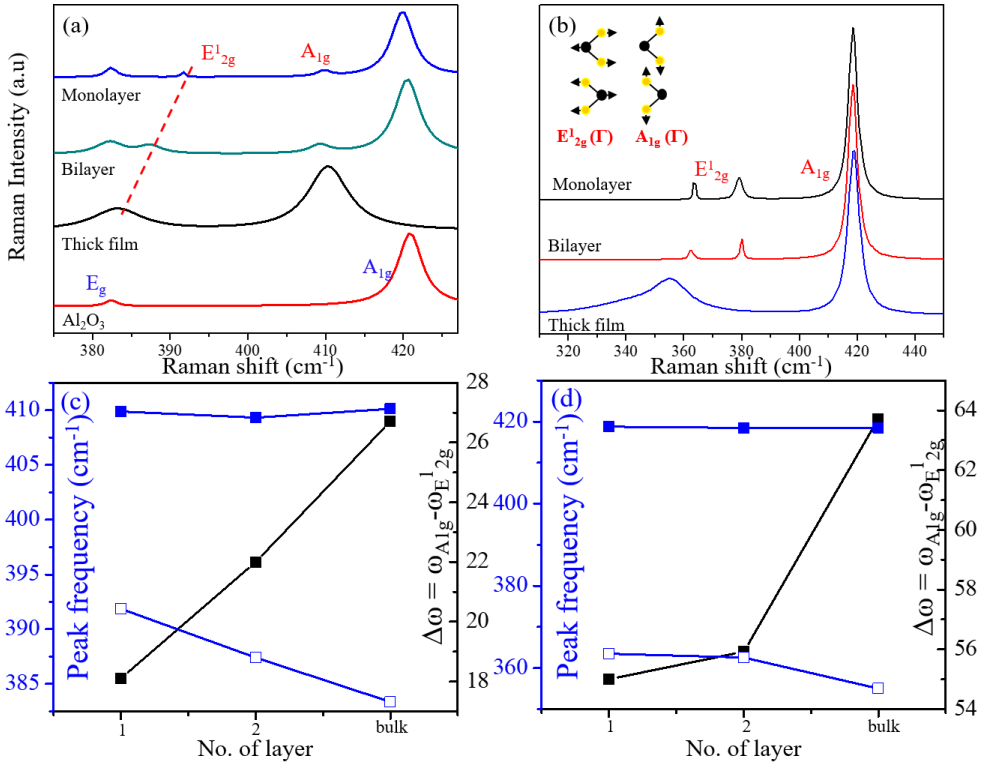

Figure 2.14. *The A_{1g} and E^1_{2g} Raman modes for monolayer, bilayer and thick films for (a) MoS_2, and (b) WS_2. For comparison the Raman modes of bare sapphire is also shown in (a). The inset of (b) shows the atomic displacements of the Raman modes. Peaks marked with the asterisks are from sapphire substrate. Raman shifts of A_{1g} and E^1_{2g} modes for monolayer, bilayers and thick films for (c) MoS_2 and (d) WS_2, showing stiffening due to compressive strain with decreasing number of layers. The difference between the A_{1g} and E^1_{2g} peaks showing anomalous peak shift with decreasing number of layers is also plotted (blue). Copyright by 2017 Elsevier [19].*

The difference between the two modes ($\Delta = A_{1g}$-E_{2g}) for the above mentioned two different samples are 25.8 and 25.5 cm^{-1}, respectively, and almost close to each other. The difference in

absolute values of these two modes between the present powder and the bulk samples may be due to the morphological effect, as powders are composed of particles which are hundreds of microns in size compared to the flat finite size few layer bulk samples reported in the literature. The thicker MoS_2 film grown in our case (~ 100 nm or ~ 140-150 number of layers) has the E^1_{2g} and A_{1g} values as 383.4 and 410.1 cm^{-1} with $\Delta = 26.7$. The absolute values are almost close to the literature [67] reported multilayer values except slightly larger Δ may be because of large number of layers over large areas (at least 8×8 sq. mm) compared to the previous reports [Figure 2.14.]. This possibly introduces stronger long range Coulomb force compared to the micrometer sized bulk powder and softens the E^1_{2g} mode further and consequently increases the band gap. The frequency values shifts to the higher wave numbers or stiffens with decreasing the number of layers as seen for the Raman shift of E and A modes in MoS_2 with shifts for monolayer/bilayer being 391.8/387.3 and 409.9/409.3 cm^{-1} [Figure 2.14.]. The difference between the Raman shifts of the two modes, Δ is 18.1 and 21.9 compared to the reported values of 17.2 and 21.4 cm^{-1}, respectively for monolayer and bilayer [67].

Thus Raman spectroscopy also confirms the formation of monolayer and bilayers MoS_2 large area epitaxial thin film in the present case in addition to TEM imaging. We also observe anomaly in the shifts in two Raman modes for MoS_2 films on sapphire substrate with number of layers as reported earlier except E^1_{2g} mode in our case stiffens significantly from 383.4 in the thick film to 387.3 and 391.8 cm^{-1} for the bilayers and monolayer, respectively whereas A_{1g} mode softens from 410.1 for the thick film to 409.9 for the monolayer.

Table 1: Raman shift for the characteristic A_{1g} and E^1_{2g} Raman modes of MoS_2. *Copyright by 2017 Elsevier [19]*.

MoS_2	E^1_{2g}	A_{1g}	Δ	Comp.strain w.r.t literature	Comp.strain w.r.t thick film	Band gap (eV)
Thick Film	383.4	410.1	26.7			
Bi layer	387.4	409.3	22	0.27%	0.28%	1.4
Mono layer	391.8	409.9	18.1	0.51%	0.52%	1.736
Literature (bulk)	383.5	408.2		24.75		

Table 2: Raman shifts for the characteristic A_{1g} and E^1_{2g} Raman modes of WS_2. *Copyright by 2017 Elsevier [19]*.

WS_2	E^1_{2g}	A_{1g}	Δ	Comp.strain w.r.t literature	Comp.strain w.r.t thick film	Band gap (eV)
Thick Film	355.0	418.8	63.7			
Bi layer	362.6	418.5	55.9	0.44%	0.47%	
Mono layer	363.4	418.5	56.1	0.49%	0.52%	1.678
Literature (bulk)	355.5	420.5	65.0			

For monolayer, the difference in the two Raman modes between literature and the present case is 3.9 and 2.5 for the E^1_{2g} and A_{1g} modes, respectively [67]. This difference in Raman modes translates into equivalent compressive strain of 0.52 % in the monolayer film on sapphire substrate. To best of our knowledge this is the only report on the substrate induced strain and its retention and this is important for tuning of optoelectronic property of such material in an effective and efficient way. It has already been predicted that introducing compressive stress will increase the band gap of the system. The change in band gap is expected to be 1.73 eV (1.68 eV without strain in PBE-GGA) for the monolayer MoS_2 [19]. The corresponding indirect band gap also increases from 1.88 eV to 1.93 eV. The origin of strain based on HRTEM imaging is discussed in the subsequent section.

PL spectra shows clear emission at 1.98 eV from monolayer film but no clear signal is obtained from bilayer and thick films suggesting that monolayer property is retained on sapphire substrate but crossover takes place after depositing subsequent layers on top of [19]. For WS_2 it is already reported that the A_{1g} (Γ) mode stiffens with increasing the number of layers which is similar to the behavior of MoS_2. This stiffening of A_{1g} mode is due to the increase in restoring force caused by band renormalization through interlayer Coulomb coupling and van der Waals interaction [83]. On the other hand the E^1_{2g} phonon mode shows only subtle changes with the number of layers. The bulk WS_2 micron size powders used in our case shows frequency corresponding to E^1_{2g} and A_{1g} as 352.6 and 420.5 cm^{-1}, respectively and the values reported in the literature are 355.5 and 420.5 cm^{-1} [46] [84] with Δ being 67.9 and 65.0 cm^{-1}, respectively. WS_2 thin films grown on sapphire substrate do not show any significant changes in the frequency of A_{1g}

mode, but E^1_{2g} mode is observed to harden significantly on decreasing the number of layers with the shifts being 363.5 and 362.6 cm^{-1} with $\Delta = 55$ and 55.9 for monolayer and bilayer, respectively. This is significantly different than reported values for monolayer i.e. 355.9 and 417.5 cm^{-1}, with a frequency difference 61.6 cm^{-1}. This shows the significant influence of sapphire substrate on the WS_2 layer. This difference in Raman modes translates into an equivalent compressive strain of 0.53 % in the monolayer film on sapphire substrate. The band gaps of monolayer WS_2 are 1.68 eV for direct. However, with 0.53 % compressive strain it is at the edge of cross over from direct (1.682 eV) to indirect (1.678 eV) band gaps [19]. Clear PL emission peak at 1.97 eV is obtained in the case of monolayer WS_2 as well and the state of the material at the edge of crossover did not disturb the probability of emission across the direct band gap. The situation is different from the case of MoS_2 where crossover is expected to take place at a compressive strain of ~ 2% [85]. This is because the rate of change of both types of band gaps with compressive strain is different for WS_2 and MoS_2. The band gap modification in both the cases can be understood in terms of coupling between various S and Mo valence orbitals [85]. Few reports exist on the stiffening of the Raman modes and associated increase in compressive strain [30,35,62]. In previous reports, strain was applied by external means. But in our case the strain is induced by substrate and can be retained which will be useful for practical device engineering of this material. The origin and nature of this substrate induced strain is discussed next.

2.3.1.3 Nature of substrate induced strain and interlayer stacking

It is interesting that though both MoS_2 and WS_2 are van der Waals compounds, sapphire substrate is capable of inducing compressive strain in this material. Generally, van der Waals interaction is comparatively very weak compared to usual ionic or covalent chemical bonding and for this force, it may seem difficult to sustain the strain. However, the theoretical calculation for 0.52% compressive strain corresponding to monolayer MoS_2 shows that the strain energy cost is only 10 meV, which is much lower compared to interlayer van der Waals force of 460 meV for MoS_2. The Photoluminescence (PL) spectra of monolayer MoS_2 and WS_2 epitaxial thin film on c-plane sapphire shown in Figure 2.15 [19]. The increases the band gap to 1.74 eV from 1.68 eV obtained using PBE-GGA potential based calculation and a value of 1.98 eV obtained by PL

measurement [19]. This implies that, there must be interaction existing between MoS_2 and the underlying substrate [19]. Negative C_s HRTEM imaging directly reveals the interfacial structure of both MoS_2 and sapphire. We present only results based on MoS_2 and similar result can be expected for WS_2. Figure 2.13. shows the atomic resolution interface image of MoS_2 on c-plane sapphire. MoS_2 has following orientation relationship with sapphire substrate i.e. $< 11\bar{2}0 > Al_2O_3 \parallel < 01\bar{1}0 > MoS_2$. The schematic model is shown in Figure 2.13. and a strain of 1.11±0.43 and 0.74±0.33 % can be derived for the first and second layer, respectively from the image. From the HRTEM images, layer specific variation of compressive strain has been estimated averaging over 15 atoms at different regions. The strain derived from HRTEM images are different from the strain derived from the Raman spectra i.e. 0.52 and 0.25 % for monolayer and bilayers, respectively.

The possible discrepancy between Raman and HRTEM could be very small area (nanometers) information probed by HRTEM compared to large area (microns) probed by Raman spectroscopy. Strain can also be in-homogenously distributed in the films. Strain fades gradually as one goes away from the film-substrate interface along the '*c*' direction. From the HRTEM imaging it is found that this interaction also translates to the third layer and beyond and reduces with the thickness of the film. The interlayer stacking is found to be Bernal stacking (2H poly-type, Figure 2.13.). Earlier reports mentioned about wide range of misoriented domains of MoS_2 grown epitaxially on a substrate and this was explained based on subtle difference in energies between different orientations [73,74]. However, in our case both by HRTEM and X-ray only one type of oriented grains are observed probably due to the slower kinetics employed [69].

Nevertheless, question remains regarding the role of substrate and its polarity on the band gap of such material. In this context, it was already shown theoretically that O dangling bond affects most among various dangling bonds in MoS_2 thin films on SiO_2 substrate [86]. O dangling bonds reduces the indirect band gap for both the monolayer and multi layers films significantly compared to direct band gap but for Si- terminated surface or H-passivated surface, changes are subtle and direct band gap remains fundamental. Thus, as it is clear from the HRTEM imaging that in the present case the substrate is Al- terminated and it is the interaction between Al dangling bonds and S which introduces the strain in these films. Based on the recent theoretical results in Ref. 86, Al terminated sapphire substrate influences the electronic structure of MoS_2 only weakly.

The experimental Al-S distance is found to be ~2.7 Å which is almost close to 2.6 Å predicted by theory [87].

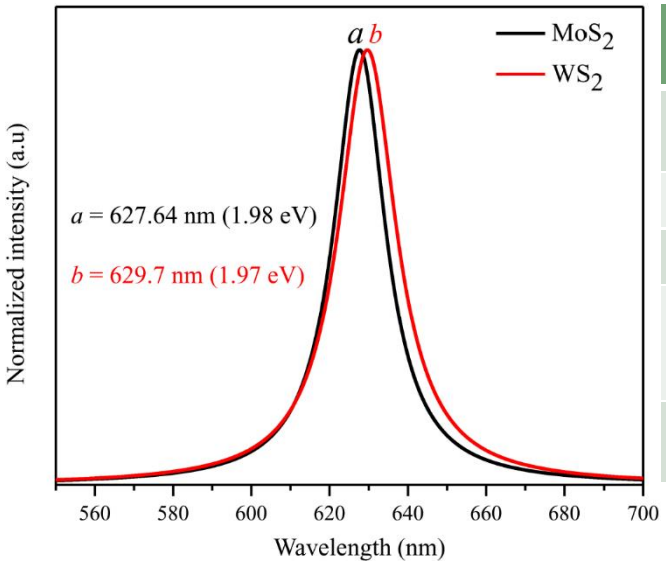

	Experimental	Theoretical (DFT)
(Monolayer TMD)	PL	GGA-PBE
MoS_2	1.90 eV [13]	1.68 eV (D)
0.52%MoS_2	1.98 eV	1.73 eV (D)
WS_2	1.968 eV [20]	1.68 eV (D) 1.682 eV (ID)
0.53%WS_2	1.97 eV	1.678 eV (ID)

***Figure 2.15**. Photoluminescence spectra of monolayer MoS_2 and WS_2 epitaxial thin film on 'c' plane sapphire, with band gap by PL and DFT [13, 20]. Copyright by 2017 Elsevier [19].*

The theoretical calculation also shows that MoS_2 can grow on sapphire with different degree of misorientation due to small energy difference between them. From our HRTEM imaging at the interface it is clearly visible that pairing of two S atoms around the Al atoms due to strain [Figure 2.13.]. Therefore, in the presence of compressive strain the difference between the direct and indirect gaps will increase as expected and remain suitable for practical device exploration and application.

2.3.2 ReS_2 Thin film

2.3.2.1 ReS_2 thin film on *c*-plane sapphire substrate

ReS_2 belongs to the family of materials known as two-dimensional transition metal dichalcogenides (2D-TMDs) [1-2,15-17]. The monolayer structure of ReS_2 is Peierls distorted $1T_d$ (space group: $P\bar{1}$) Where four Re atoms are hybridized together to form 2D quasi-periodic superstructure [Figure 2.01.]. We begin with the structural characterization of ReS_2 thin films by TEM. Figure 2.17. (a)-(f) are the low magnification cross-sectional bright field TEM images of ReS_2 thin film on *c-plane* sapphire at various growth temperatures: 150, 200, 250, 300 and 400°C, respectively. The thickness of the films is in the range of ~ 30-50 nm except the film grown at 150 °C (300 nm). The films are smooth and continuous but at discrete places on the surface 3D growth of crystals can be observed turning the film rough.

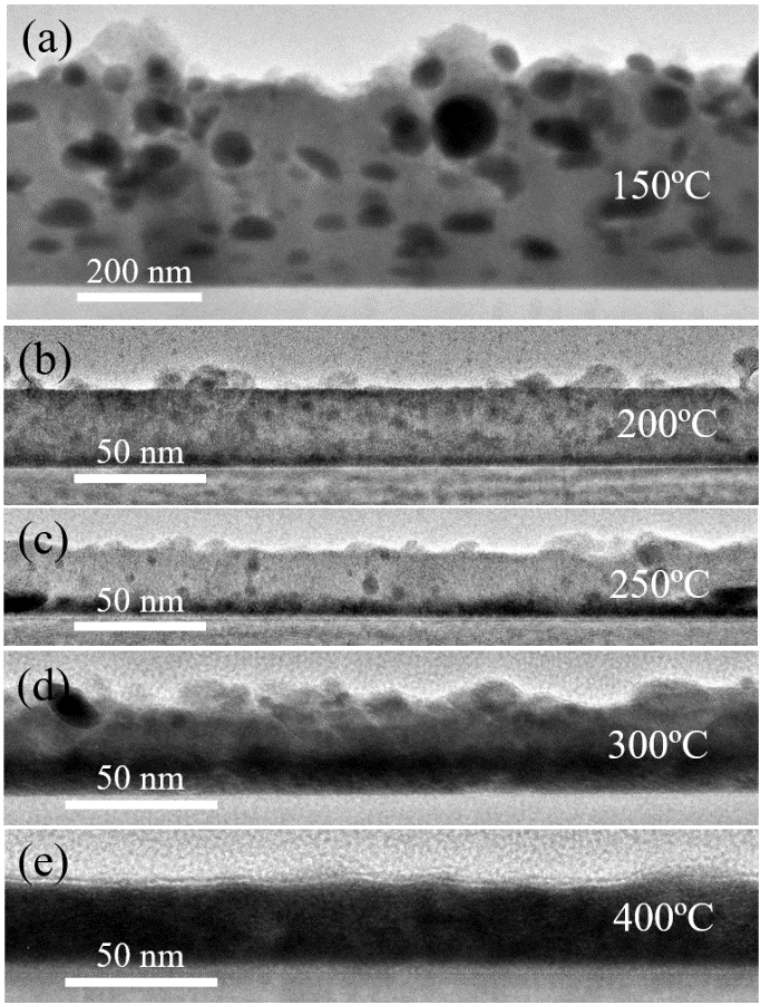

Figure 2.17. *(a)-(e) Low magnification cross sectional TEM bright field images of ReS_2 thin film grown on sapphire substrate at various deposition temperatures. The films are smooth and from place to place formation of 3D particles at the surface making the film rough. The thickness of the films is ~ 20-30 nm except the film grown at 150 °C (300 nm). Copyright by 2019 Elsevier [59].*

Formation of 3D crystals on the surface is more predominant at lower deposition temperatures and is suppressed with increasing growth temperature till 300°C. Scattered dark particles can be observed throughout the volume of the film and these are found to be Re metals. Next are the details on the orientation relationship between film and substrate, identification of the dispersed dark particle and nature of surface 3D crystals by HRTEM.

HRTEM image of the ReS_2 thin film (150°C) along $< 2\bar{1}\bar{1}0 >$ zone axis (Z.A.) of sapphire. Both the image and corresponding fast Fourier transform (FFT) pattern confirm that the (0001) plane of ReS_2 is perpendicular to the (0001) plane of sapphire shown in Figure 2.18. (a) is the. The epitaxial relationship is thus$(0001)ReS_2 \perp (0001)Al_2O_3$. The vertical planes start forming at the interface and continue towards the surface. Scattered particles with dark contrast marked with white circle can be observed throughout the film. These particles are identified as hexagonal Re metals (space group P63/mmc, d_{0002} = 2.22 Å) [Figure 2.18. (b)]. the appearance of particles is dark because Re has higher average atomic number (Z = 75) per unit volume compared to ReS_2 thus scattering more electrons out of the aperture (mass-thickness contrast).

Table 3. List of samples deposited on two different substrates and various deposition temperatures. Nature of the films observed also mentioned. *Copyright by 2019 Elsevier [59]*.

Substrates	Deposition Temperature (°C)	Nature of the Film
c Al_2O3	150	$(0001)ReS_2 \perp (0001)Al_2O_3$
c Al_2O3	200	$(0001)ReS_2 \perp (0001)Al_2O_3$ with branching
c Al_2O3	250	$(0001)ReS_2 \perp (0001)Al_2O_3$ onset of polycrystal formation near the interface
c Al_2O3	300	Polycrystalline layer near the interface
c Al_2O3	400	Re metal polycrystalline film
c Al_2O_3/MoS_2	150	$(0001)ReS_2 \perp (0001)MoS_2$
c Al_2O_3/MoS_2	250	$(0001)ReS_2 \perp (0001)MoS_2$
c Al_2O_3/MoS_2	400	Re metal polycrystalline film

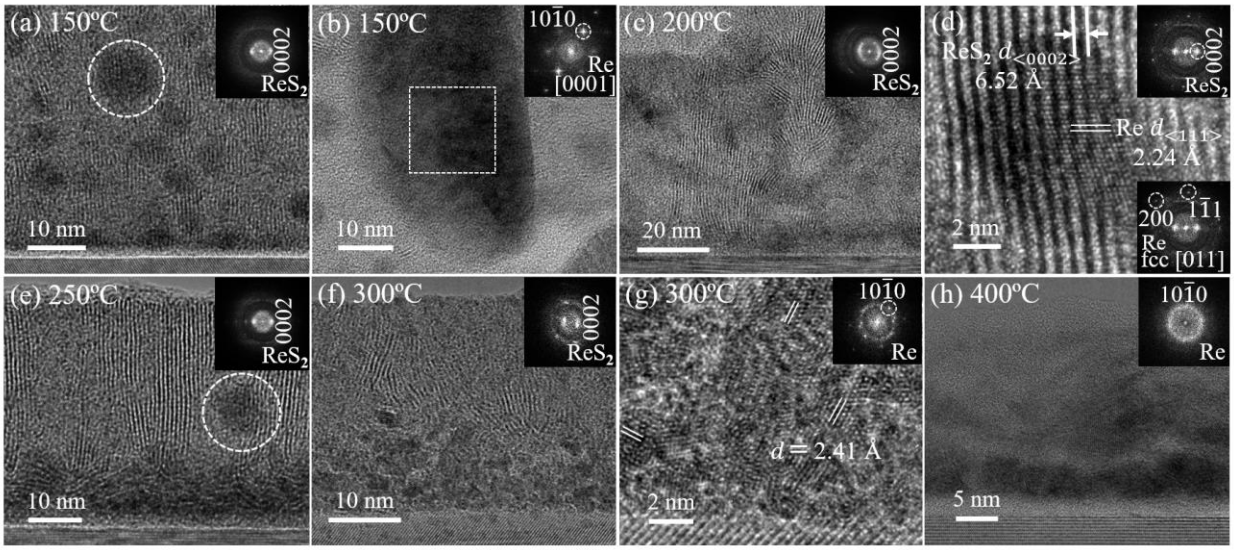

Figure 2.18. *HRTEM images of ReS_2 films grown on sapphire at various deposition temperatures. The films are grown with c-plane perpendicular to the film substrate interface at growth temperature (a) T = 150 °C, (b) Dispersed hexagonal Re metal particles are marked with dotted white squire (T = 150 °C). (c) & (e) Branching of ReS_2 layers can be seen in films grown at 200 and 250°C. (d) Metastable fcc Re metal (a = 3.89 Å) of ~3 nm size is observed. (f) & (g) film is polycrystalline grown at 250 °C near the interface and vertical planes above it is meandering towards the surface. (h) Polycrystalline Re metal film is obtained at growth temperature of 400 °C. Copyright by 2019 Elsevier [59].*

The lattice parameters of hexagonal Re is a = 2.76 Å and c = 4.45 Å. The size of the particles is ~ 30 nm. The 3D crystals formation on the surface for film grown at 150 °C leading to rough morphology is also found to be hexagonal Re metals. The possible origin of Re metals could be from the ReS_2 target pellet. During vacuum sintering there is a prospect for S loss and formation of local Re rich areas which may subsequently form Re metals nano particles during laser ablation and dispersed throughout the film. XRD of ReS_2 pellet reveals the presence of Re metal in the pellet [Figure 2.19. (a)]. Therefore, formation of Re metal particles in the film volume can be avoided if ReS_2 target pellets can be fabricated without such Re rich local regions and this may be achieved with an improved sintering process preventing S loss. In some places, the films are found to be amorphous coexisting with the crystalline regions [Figure 2.20.(a)].

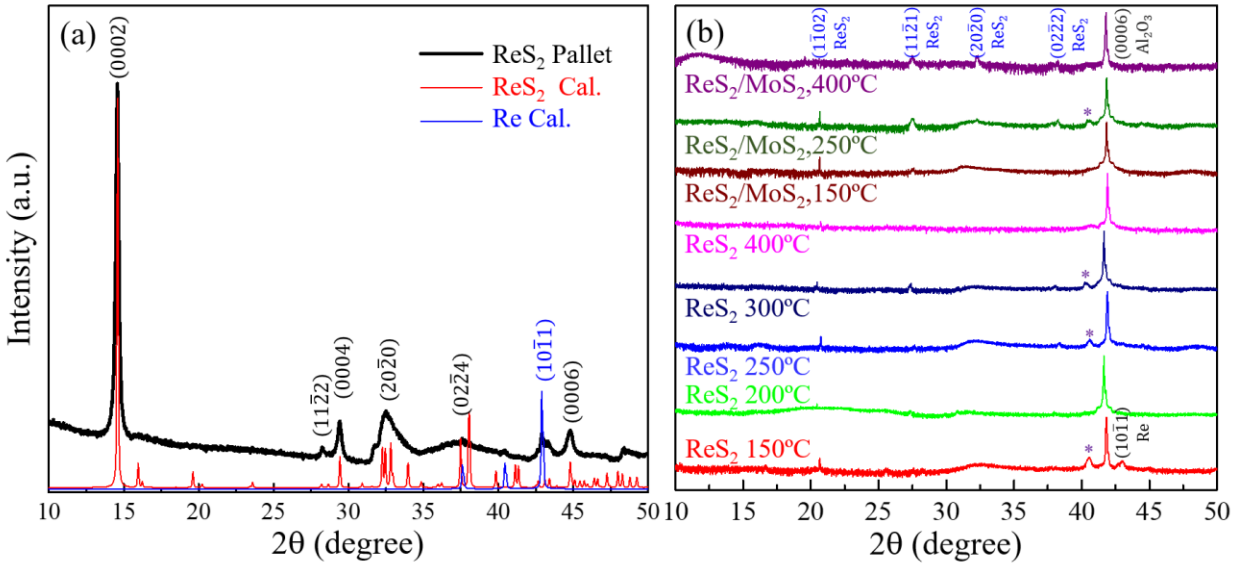

Figure 2.19. *(a) XRD of ReS_2 pellet reveals minor presence of Re. (b) X-ray diffraction pattern of various ReS_2 thin films grown on both sapphire substrate and MoS_2 template at different temperatures. Copyright by 2019 Elsevier [59].*

The film grown at 200 °C shows similar features of film grown at 150 °C but from place to place the *c* planes start branching away from the vertical direction and forming a dome like structure at the surface [Figure 2.18.(c) & Figure 2.20.(b)&(c)]. In some areas, Re metal with cubic crystal structure is detected though the hexagonal form is the predominant phase [Figure 2.18.(d)]. The lattice parameter of metastable fcc Re is 3.89 Å. The formation of metastable Re phase might have been due to phase transformation from hcp to fcc structure following Bain transformation [88]. With increasing deposition temperature to 250 °C, the branching start dominating near the interface [Figure 2.18.(e)]. This led to the formation of films consisting of both vertical domains and tilted domains. This is also reflected in the XRD pattern in terms of additional peaks [Figure 2.19.(b)]. However, the most favoured vertical orientation is maintained, and domains of rotating vertical planes can be observed. The region near the interface of the film grown at 300 °C is polycrystalline made of mostly ReS_2 crystal (~ 5 nm size) with vertical planes on top of it meandering towards the surface [Figure 2.18.(f) & (g)]. Finally, the film grown at 400 °C, which is above the melting point of ReS_2 is completely polycrystalline and made of Re metals [Figure 2.18.(h)].

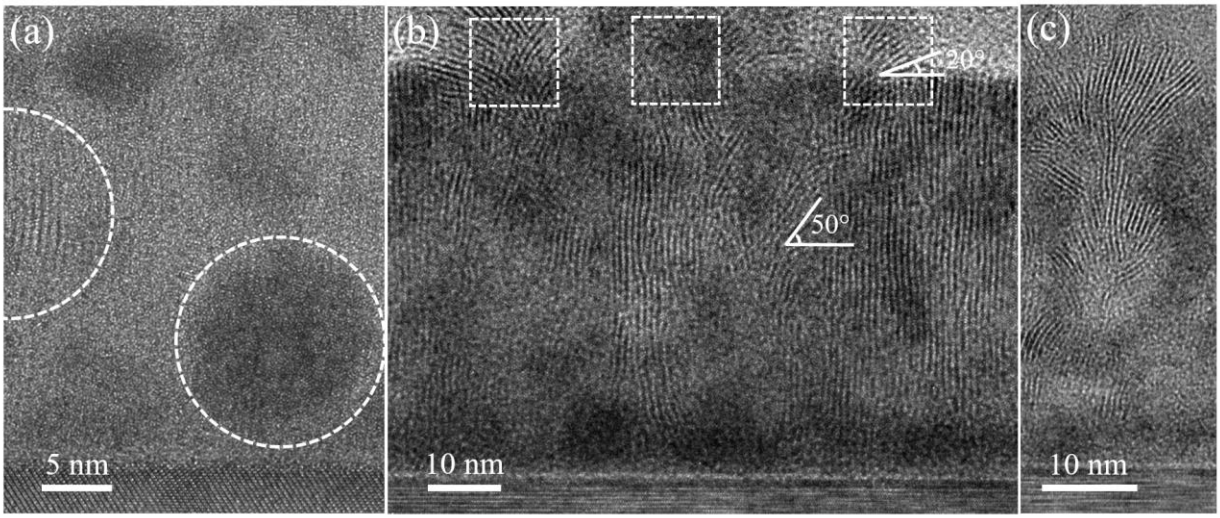

Figure 2.20. *(a) In some places of ReS_2 film grown at 150 °C films are found to be amorphous coexisting with the crystalline regions may be due to lower deposition temperature. (c) & (d) Branching in ReS_2 in several direction which is reflected as different peaks in XRD pattern [shown in* ***Figure 2.19.****]. From place to place the c planes start branching away from the vertical direction and creating a dome-like structure at the surface for the film grown at 200 °C. Copyright by 2019 Elsevier [59].*

2.3.2.2 ReS_2 thin film on MoS_2

Low magnification TEM images of the ReS_2 thin film grown on MoS_2 template at three different temperatures: 150, 250, and 400 °C, respectively shown in Figure 2.21. The thickness and growth temperature of the MoS_2 template layer is 20 nm and 400 °C, respectively following the procedure already described in Ref. 19. Two different layers can be identified from the mass-thickness contrast. ReS_2 appears darker compared to MoS_2 due to higher average atomic mass. The surface and interface are smooth and free from dome like morphology compared to films directly grown on the sapphire substrate except for the film grown at 400 °C. The thickness of the ReS_2 films is ~ 20 nm.

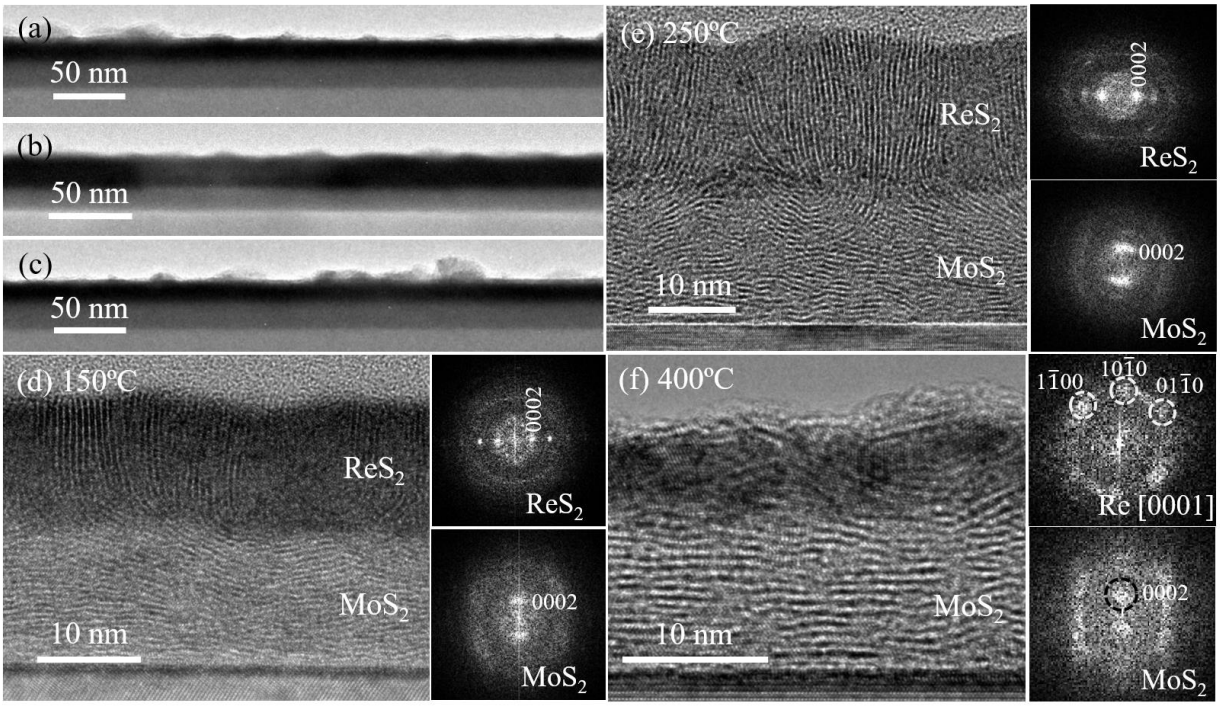

Figure 2.21. *(a)-(c) low magnification cross sectional TEM bright field images of ReS_2 films grown on MoS_2 template at three different temperatures: 150, 250 and 400 °C. Films are smooth for films grown at 150 and 250 °C. Roughness is more for film grown at 400°C. (e)-(f) HRTEM images from three different films. Epitaxial relationship is* $(0001)ReS_2 \perp (0001)MoS_2 \parallel (0001)Al_2O_3$ *for films grown at 250 and 300 °C. The film is polycrystalline at 400°C. Copyright by 2019 Elsevier [59].*

Figure 2.21.(d)-(f) are the HRTEM images from three different ReS_2 films grown on MoS_2 template. From the images and the FFT patterns, it can be observed that the *c-plane* of MoS_2 film is parallel to the interface whereas in case of ReS_2, the *c-plane* is perpendicular for films grown at 150 and 250 °C. The epitaxial relationship is the same as in the case of sapphire. The nucleation of ReS_2 occurs at the terminating edges of the MoS_2 planes and propagates along the vertical direction. The film grown at 400°C is polycrystalline as the temperature is above the melting point of ReS_2 and consisting of Re metals like the case of the film grown on sapphire substrate.

XRD pattern of ReS_2 films grown on both sapphire substrate and MoS_2 template at various temperatures are shown in Figure 2.19.(b). The number of peaks is restricted due to specific orientations of both film and substrate. Sapphire (0006) peak appears at $2\theta = 41.8°$. The peak at

32.2° is from $(20\bar{2}0)$ plane of vertically oriented ReS_2 film. Other peaks of ReS_2 identified at 20.4, 27.3, and 38.1° are corresponding to$(1\bar{1}02)$,$(11\bar{2}1)$, and $(02\bar{2}2)$ planes respectively. The peak at $2\theta = 42.9°$ corresponding to hexagonal Re $(1\bar{1}01)$ is dominating for film grown at 150 °C due to large thickness compared to other films. The peak at 40.4° marked with * possibly from shifted (0002) plane of ReS_2 as many inclined orientations can be observed from the HRTEM images which have contributed to this peak intensity [Figure 2.20.(b) & (c)].

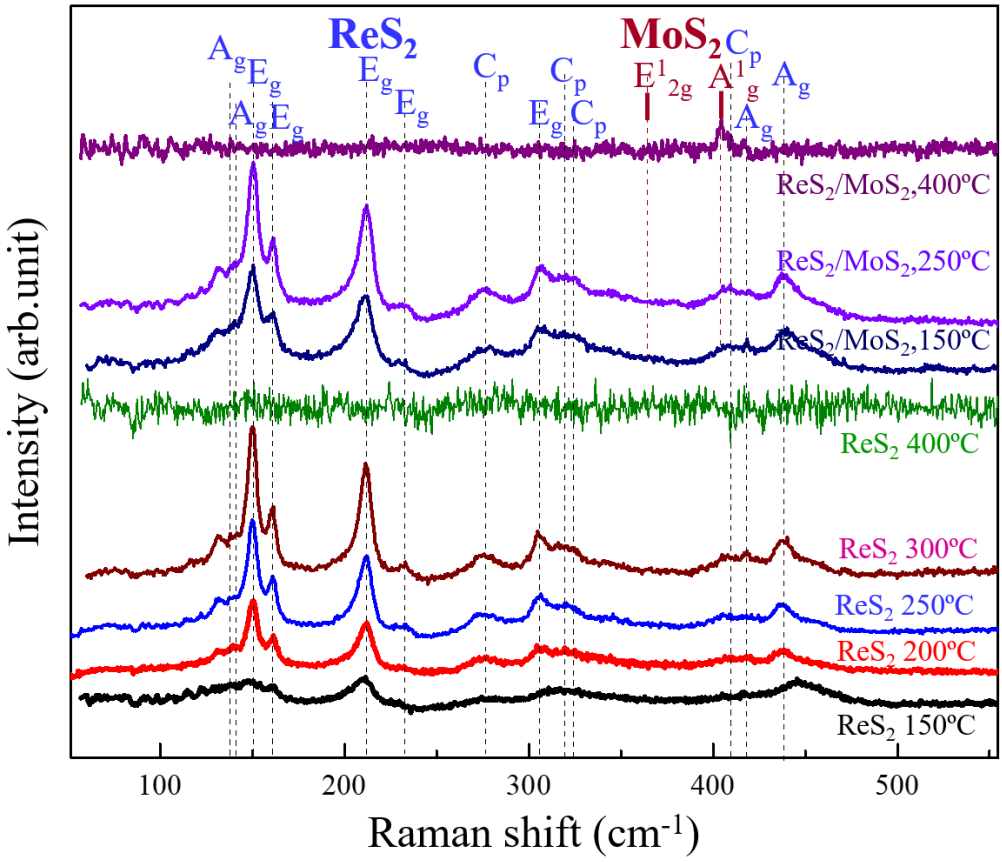

Figure 2.22.*Raman spectra of various ReS_2 thin films grown on sapphire substrate and MoS_2 template at different temperatures. No peaks corresponding to ReS_2 are observed for the films grown at 400°C. Copyright by 2019 Elsevier [59].*

Raman spectra of all the ReS_2 films are given in Figure 2.22. The modes corresponding to ReS_2 and MoS_2 are indicated in the thirteen Raman actives modes of ReS_2 are observed. These are five in-plane (E_g), four out-of-plane (A_g) and in-plane and out-of-plane coupled (C_p) vibrational modes. No modes corresponding to ReS_2 are observed for the film grown at 400 °C. This is

consistent with the observation of Re metals in the films grown at 400 °C. The E_g modes at 150.5, 161.3, 212.4 and 233.2 cm^{-1} are due to in-plane vibrations of Re atoms, while the modes at 304.8 cm^{-1} is due to in-plane vibrations of S atoms. A_g modes located at 138.5 and 141.7 cm^{-1} are related to out-of-plane vibrations of Re atoms, while the modes at 418.7 and 437.4 cm^{-1} are from the out-of-plane vibrations of S atoms. The C_p modes at 278.3 cm^{-1} are due to couple in and out-of-plane vibration of Re and S atoms, while 320.6, 324.9 and 407.3 cm^{-1} are the couple in-plane and out-of-plane vibration of S atoms [16, 89]. In case of MoS_2, characteristic A_{1g} and E^1_{2g} modes located at 378.8 and 405.8 cm^{-1} are indicated. E^1_{2g} modes located at 378.8 cm^{-1} is due to the vibration of two S atoms in the opposite direction, while A_{1g} mode located at 405.8 cm^{-1} is due to the out-of-plane vibration of S atoms along opposite directions [90].

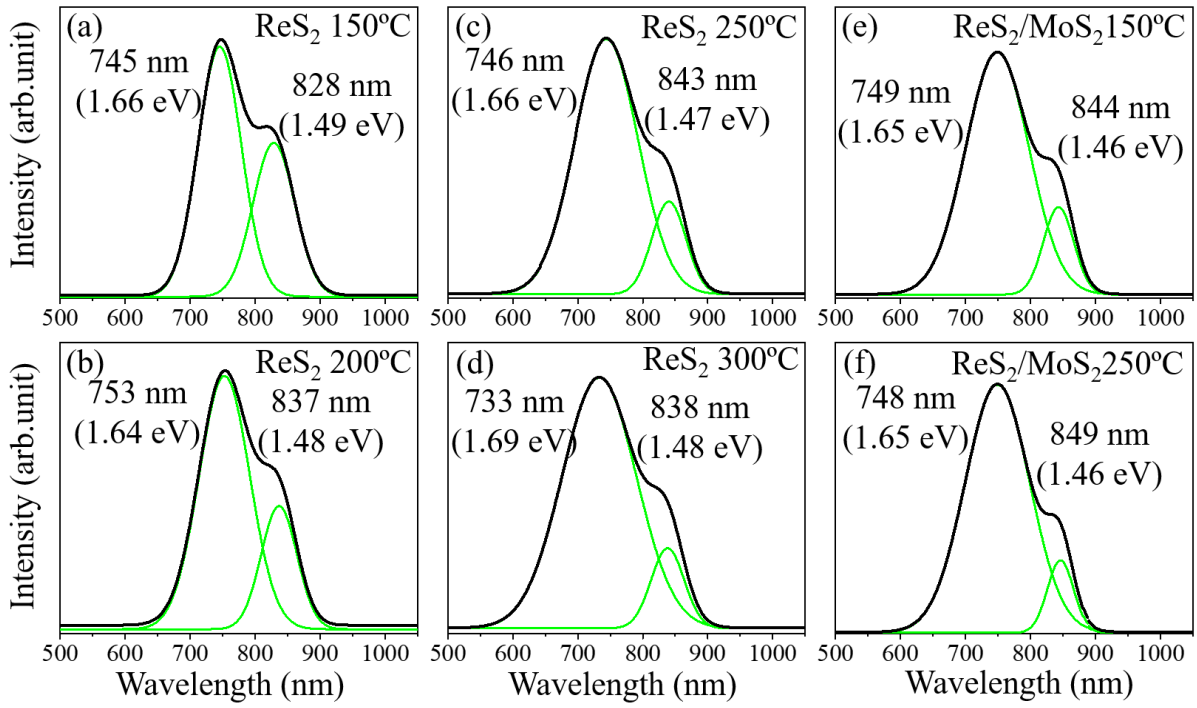

Figure 2.23.*CL spectra from various ReS_2 thin films showing two emission peaks around 1.67 and 1.47 eV. The relative intensity difference between the peaks increases for the films grown on MoS_2 template. Copyright by 2019 Elsevier [59].*

CL spectra of ReS_2 films grown on sapphire and MoS_2 template are shown in *Figure 2.23.* Two distinct emission peaks are observed at around1.67 and 1.47 eV with some variation in peak position for different films. The intensity ratio of the peaks increases for films grown on MoS_2 template compared to sapphire substrate. Though the films are not monolayer but observing peaks corresponding to both monolayer and multilayers may be because of film orientation which is truncated 0001 plane and presence of both interlayer layer coupling and decoupling effect. CL confirms that all the thin films are optically active material except for the films grown at 400 °C which consists of Re metals and may find wide applications. However, the challenge remains on the growth of flat ReS_2 film by PLD, may be the choice of substrate, control over kinetic and process parameters need to be explored further.

2.4 Conclusion

In summary, we have grown large area epitaxial thin films of van der Waals compounds MoS_2 and WS_2 on '*c*' plane sapphire by pulsed laser deposition with control over the number of layers. Substrates induced compressive strain is responsible for the stiffening of both the Raman modes with implication in increase in the direct band gap of these materials and their retention. The results demonstrate a practical way to engineer the optoelectronic property of such materials for large area device fabrication and application. Growth of ReS_2 thin films on sapphire substrate and MoS_2 template by PLD has been investigated at various deposition temperatures. The films grow *c-plane* perpendicularly with respect to the film substrate interface on both the substrates at lower deposition temperatures. The films are polycrystalline and contain mostly Re metals grown at temperature above 400 °C. The quality of the film is better grown on MoS_2 template compared to sapphire substrate. The results demonstrate that PLD can be used to grow ReS_2 thin film for any possible device application.

2.5 Bibliography

[1] A. K. Geim, K. S Novoselov, Nat. Mater. **6**, 183−191 (2007).

[2] A. K. Geim, I. V. Grigorieva, Nature **499,** 420 (2013).

[3] C. N. R. Rao, A. K. Sood, R. Voggu, K. S. Subrahmanyam, J. Phys. Chem. Lett. **1,** 572–580 (2010).

[4] P. Vogt, P. De Padova, C. Quaresima, J. Avila, E. Frantzeskakis, M. C. Asensio, A. Resta, B. D. Ealet, G. L. Lay, Phys. Rev. Lett. **108,** 155501(2012).

[5] Y. Xu, B. Yan, H. Zhang, J. Wang, G. Xu, P. Tang, W. Duan, S. Zhang, Phys. Rev. Lett. **111,** 136804 (2013).

[6] E. Bianco, S. Butler, S. Jiang, O. D. Restrepo, W. Windl, J. D. Goldberger, ACS Nano **7,** 4414-4421 (2013).

[7] K. S. Novoselov, A. K. Geim, S. V. Morozov, D. Jiang, M. I. Katsnelson, I. V. Grigorieva, S. V. Dubonos. A. A. Firsov. Nature **483**, 197- 200 (2005).

[8] S. D. Sarma, S. Adam, E. H. Hwang, E. Rossi, Rev. Mod. Phys. **83,** 407-470 (2011).

[9] K. S. Novoselov, A. K. Geim, S.V. Morozov, D. Jiang, Y. Zhang, S. V. Dubonos, I. V. Grigorieva, A. A. Firsov, Science **306,** 666-669 (2004).

[10] Y. Zhang, Y. Tan, H. Stormer, P. Kim, Nat. Lett. **438**, 201-203 **(**2005).

[11] L. Qu, Y. Liu, J. Baek, L. Dai, ACS Nano **4**, 1321-1326 (2010).

[12] K. S. Kim, Y. Zhao, H. Jang, S. Y. Lee, J. M. Kim, K. S. Kim, J. Ahn, P. Y. Jae-Young Choi, B. H. Hong, Nature **457,** 706-710 (2009).

[13] K. Fai Mak, C. Lee, J. Hone, J. Shan, T. F. Heinz , Phys. Rev. Lett. 10**5,** 136805(4) (2010).

[14] M. Xu, T. Liang, M. Shi, H. Chen, Chem. Rev. **113,** 3766-3798 (2013).

[15] C.N.R. Rao, K. Gopalakrishnan, U. Maitra, ACS Appl. Mater. Interfaces **7**, 7809–7832 (2015).

[16] M. Rahman, K. Davey, S.Z. Qiao, Adv. Funct. Mater. **27**, 1606129 (2017).

[17] S. Tongay, H. Sahin, C. Ko, A. Luce, W. Fan, K. Liu, J. Zhou, Y.-S. Huang, C.-H. Ho, J. Yan, D. F. Ogletree, S. Aloni, J. Ji, S. Li, J. Li, F.M. Peeters, J. Wu, Nat. Commun **5**, 3252 (2014).

[18] K. Dileep, R. Sahu, S. Sarkar, S. C. Peter, R. Datta, J. Appl. Phys. **119,** 114309 (2016).

[19] R. Sahu, D. Radhakrishnan, B. Vishal, D. S. Negi, A. Sil, C. Narayana, R. Datta, J. Cryst. Growth **470,** 51–57 (2017).

[20] W. Zhao, Z. Ghorannevis, L. Chu, M. Toh, C. Kloc, P.-H. Tan, G.Eda, ACS Nano, **7** 791–797 (2013).

[21] O. B. Aslan, D. A. Chenet, A. M. van der Zande, J. C. Hone,T. F. Heinz, ACS Photonics **3**, 96 (2015).

[22] Y.-C. Lin, H.-P. Komsa, C.-H.Yeh, T.Bjorkman, Z.-Y. Liang, C.-H. Ho, Y.-S. Huang, P.-W. Chiu, A. V. Krasheninnikov, K. Suenaga, ACS Nano **9**, 11(2015).

[23] H. S. S. Ramakrishna Matte, A. Gomathi, Arun K. Manna, Dattatray J. Late, R. Datta, S. K. Pati, and C. N. R. Rao, Angew. Chem. **122**4153 –4156 **(**2010).

[24] Y. Zhan, Z. Liu, S. Najmaei, P. M. Ajayan, and J. Lou, Small **8,** 966 (2012).

[25] N. Liu, P. Kim, J. H. Kim, J. H. Ye, S. Kim, and C. J. Lee, ACS Nano **8**, 6902-6910 (2014).

[26] Y. H. Lee, X. Q. Zhang, W. Zhang, M. T. Chang, C. T. Lin, K. D. Chang, Y. C. Yu, J. T. W. Wang, C. S. Chang, L. J. Li, and T. W. Lin, Adv. Mater. **24,** 2320 (2012).

[27] S. B. Desai, S. R. Madhvapathy, A. B. Sachid, J. P. Llinas, Q. Wang, G. H. Ahn, G. Pitner, M. J. Kim, J. Bokor, C. Hu, H.-S. P. Wong, A. Javey, Science **354,** 6308 (2017).

[28] R. Browning, P. Padigi, R. Solanki, D. J. Tweet, P. Schuele, and D. Evans, Mater. Res. Express **2,** 0355006 (2015).

[29] K. He, C. Poole, K. F. Mak, and J. Shan, Nano Lett. **13,** 2931(2013).

[30] A. C. Gomez, R. Roldán, E. Cappelluti, M. Buscema, F. Guinea, H. S. J. van der Zant, and G. A. Steele, Nano Lett. **13** 5361 (2013).

[31] H. Pan, and Y. W. Zhang, J. Phys. Chem. C **116,** 11752 (2012).

[32] C. H. Chang, X. Fan, S. H. Lin, and J. L. Kuo, Phys. Rev. B **88,** 195420 (2013).

[33] W. S. Yun, S. W. Han, S. C. Hong, I. G. Kim, and J. D. Lee, Phys. Rev. B **85,** 033305(2012).

[34] C. Rice, R. J. Young, R. Zan, and U. Bangert, D. Wolverson, T. Georgiou, R. Jalil, and K. S. Novoselov Phys. Rev. B **87**, 081307(R) (2013).

[35] C. R. Zhu, G. Wang, B. L. Liu, X. Marie, X. F. Qiao, X. Zhang, X. X. Wu, H. Fan, P. H. Tan, T. Amand, and B. Urbaszek, Phys.Rev. B **88,** 121301(R) (2013).

[36] J. Jeon, S. K. Jang, S. M. Jeon, G. Yoo, Y. H. Jang, J. H. Park, and S. Lee, Nanoscale **7,** 1688-1695 (2015).

[37] Y.-H. Lee, X.-Q. Zhang, W. Zhang, M.-T. Chang, C.-T. Lin, K.-D. Chang, Y.-C. Yu, J. T.-W. Wang, C.-S. Chang, L.-J. Li, T.-Wu Lin, Adv. Mater. **24**, 2320-2325 (2012).

[38] M. Okada, T. Sawazaki, K. Watanabe, T. Taniguch, H. Hibino, H. Shinohara, R. Kitaura, ACS Nano **8,** 8273–8277 (2014).

[39] Z. Jin, S. Shin, D. H. Kwon, S. J. Han, Y. S. Min, Nanoscale **6**,14453 (2014).

[40] T.W. Scharf, S.V. Prasad, T.M. Mayer, R.S. Goeke, and M.T. Dugger, J.mat.research 19 3443-3446 (2004).

[41] E. Liu, Y. Fu, Y. Wang, Y. Feng, H. Liu, X. Wan, W. Zhou, B. Wang, L. Shao, C.-H. Ho, Y-S. Huang, Z. Cao, L. Wang, A. Li, J. Zeng, F. Song, X. Wang, Y. Shi, H. Yuan, H. Y. Hwang, Y. Cui, F. Miao & D. Xing, Nat. Comm. **6**, 6991 (2015).

[42] J. Shim, A. Oh, D.H. Kang, S. Oh, S.K. Jang, J. Jeon, M.H. Jeon, M. Kim, C. Choi, J. Lee, Adv. Mater. **28,** 6985-6992 (2016).

[43] F. Liu, S. Zheng, X. He, A. Chaturvedi, J. He, W.L. Chow, T.R. Mion, X. Wang, J. Zhou, Q. Fu, H. J. Fan , B. K. Tay , L. Song , R-H. He, C. Kloc, P. M. Ajayan, Z. Liu, Adv. Funct. Mater. **26,** 1169-1177 (2016).

[44] D. Ovchinnikov, F. Gargiulo, A. Allain, D.J. Pasquier, D. Dumcenco, C.-H. Ho, O.V. Yazyev, A. Kis, Nat. Commun, **7,** 12391 (2016).

[45] H. Liu, B. Xu, J.-M. Liu, J. Yin, F. Miao, C.-G. Duan, X. Wan, Phys. Chem. Chem. Phys. **18,** 14222-14227 (2016).

[46] L. Wang, Z. Sofer, J. Luxa, D. Sedmidubský, A. Ambrosi, M. Pumera, Electrochem. Commun. **63**, 39-43 (2016).

[47] J. Gao, L. Li, J. Tan, H. Sun, B. Li, J.C. Idrobo, C.V. Singh, T.-M. Lu, N. Korathar, Nano Lett. **16,** 3780 (2016).

[48] B. Jariwala, D. Voiry, A. Jindal, B. A. Chalke, R. Bapat, A. Thamizhavel, M. Chhowalla, M. Deshmukh, A. Bhattacharya, Chem. Mater. **28,** 3352 (2016).

[49] K. Keyshar, Y. Gong, G. Ye, G. Brunetto, W. Zhou, D.P. Cole, K. Hackenberg, Y. He, L. Machado, M. Kabbani, A. H. C. Hart , B. Li , D. S. Galvao , A. George , R. Vajtai , C. Sekhar Tiwari, P.M. Ajayan, Adv. Mater. **27**, 4640-4648 (2015).

[50] F. Cui, C. Wang, X. Li, G. Wang, K. Liu, Z. Yang, Q. Feng, X. Liang, Z. Zhang, S. Liu, Z. Lei ,Z. Liu, H. Xu, J. Zhang, Adv. Mater. **28,** 5019-5024 (2016).

[51] M. Hafeez, L. Gan, H. Li, Y. Ma, T. Zhai, Adv. Funct. Mater. **26**, 4551 (2016).

[52] N. Al-Dulaimi, E. A. Lewis, D. J. Lewis, S. K. Howell, S. J. Haigh,P. O'Brien, Chem. Commun. **52**, 7878 (2016).

[53] U. Bhat, R. Singh, B. Vishal, A. Sharma, S. Horta, R. Sahu, R. Datta, Phys. Status Solidi B **255,** 1700691(2018).

[54] T.A.J. Loh, D.H.C. Chua, ACS Appl. Mater. Interfaces **6,** 15966−15971 (2014).

[55] G. Siegel, Y.P.V. Subbaiah, M.C. Prestgard, A. Tiwari, APL Materials **3,** 056103 (2015).

[56] A. Barvat, N. Prakash, G. Kumar, D. K. Singh, A. Dogra, S.P. Khanna, P. Pal, Curr. Appl. Phys. **18,** 170 (2018).

[57] Y.-T. Ho, C.-H. Ma, T.-T. Luong, L.-L. Wei, T.-C. Yen, W.-T. Hsu, W.-H. Chang, Y.-C. Chu, Y.-Y. Tu, K.P. Pande, E. Y. Chang, Phys. Status Solidi Rapid Res. Lett. **9,** 187-191 (2015).

[58] A. Barvat, N. Prakash, B. Satpati, S. S. Singha, G. Kumar, D. K. Singh, A. Dogra, S.P. Khanna, A. Singha, P. Pal, J. Appl. Phys. **122,** 015304 (2017).

[59] B. Vishal, H. Sharona, U. Bhat, A. Paul, M. B. Sreedhara, V. Rajaji, S. C. Sarma, C. Narayana, S. C. Peter, and R. Datta, Thin Solid Films, **685,** 81–87 (2019).

[60] Y. Kim, B. Kang, Y. Choi, J.H. Cho, C. Lee, 2D Materials, **4**, 025057 (2017) .

[61] X. Li, F. Cui, Q. Feng, G. Wang, X. Xu, J. Wu, N. Mao, X. Liang, Z. Zhang, J. Zhang, H. Xu, Nanoscale **8,** 18956-18962 (2016).

[62] J.-K. Qin, W.-Z. Shao, Y. Li, C.-Y. Xu, D.-D. Ren, X.-G. Song, L. Zhen, RSC Adv. **7,** 24188-24194 (2017).

[63] F. Qi, Y. Chen, B. Zheng, J. Zhou, X. Wang, P. Li, W. Zhang, Materials Letters **184,** 324-327 (2016).

[64] M. B. Sreedhara, S. Gope, B. Vishal, R. Datta, A. J. Bhattacharyya, C. N. R. Rao, J. Mater. Chem. A **6,** 2302 (2018).

[65] J. Hämäläinen, M. Mattinen, K. Mizohata, K. Meinander, M. Vehkamäki, J. Räisänen, M. Ritala, M. Leskelä, Adv. Mater. 1703622 (2018).

[66] Q. Zhang, S. Tan, R. G. Mendes, Z. Sun, Y. Chen, X. Kong, Y. Xue, M. H. Rümmeli, X. Wu, S. Chen, L. Fu, Adv. Mater. **28**, 2616 (2016).

[67] H. J. Conley, B. Wng, J. I. Ziegler, R. F. Haglund, S. T. Pantelides, and K. I. Bolotin, Nano Letters **13**, 3626-3630 (2013).

[68] Y. Y. Hui, X. Liu, W. Jie, N. Y. Chan, J. Hao, Y. T. Hsu, L. J. Li, W. Guo, and S. P. Lau, ACS Nano **8,** 7126-7131 (2013).

[69] B. Loukya, P. Sowjanya, K. Dileep, R. Shipra, S. Kanuri, L. S. Panchakarla and R. Datta, J. Crys. Growth **329,** 20-26 (2011).

[70] K. Dileep, R. Sahu, K. K. Nagaraja and R. Datta, J. Crys. Growth **402,** 124-129 (2014).

[71] R. Sahu, K. Dileep, D. S. Negi, K. K. Nagaraja, S. Shetty, and R. Datta, J. Crys. Growth **410** 69-76 (2015).

[72] D. S. Negi, B. Loukya, K. Dileep, M. Kesaria, N. Kumar, and R. Datta, Superlatt. Microstruct. **63,** 289-297 (2013).

[73] J. A. Greera, M. D. Tabat, J. Vac. Sci. Technol. A **13,** 1175(1995).

[74] M. Lorenz, H. Hochmuth, D. Natusch, H. Börner, G. Lippold, K. Kreher, W. Schmitz, Appl. Phys. Lett. **68,** 3332 (1996).

[75] Q.Ji, M. Kan, Y. Zhang,Y. Guo, D. Ma, J. Shi, Q. Sun, Q. Chen, Y. Zhang, Z. Liu, Nano Lett. **15,** 198−205 (2015).

[76] D. Dumcenco, D. Ovchinnikov, K. Marinov, P. Lazi_c, M. Gibertini, N. Marzari, O. L. Sanchez, Y. Kung, D. Krasnozhon, M. Chen, S. Bertolazzi, P. Gillet, A. F. Morral, A. Radenovic, A. Kis, ACS Nano **4**, 4611-4620 (2015).

[77] C. R. Serrao, A. M. Diamond, S. Hsu, L. You, S. Gadgil, J. Clarkson, C. Carraro, R. Maboudian, R.; C. Hu, S. Salahuddin, Appl. Phys. Lett. **106,** 052101(2015).

[78] G. V. P. Kumar, C. Narayana, Current Science. **93,** 778-781 (2007).

[79] B. Loukya, Electron Magnetic Circular Dichrosim of epitaxial magnetic thin film at nanoscale, Ph.D Thesis (2015).

[80] C. L. Jia, M. Lentzen, K. Urban, Science **299,** 870 (2007).

[81] R. Datta, S. Kanuri, V. Karthik, D. Mazumdar, J. X. Ma, A. Gupta, Appl. Phys. Lett. **97,** 071907 (2010).

[82] Y. Yu Hui, X. Liu,W. Jie, N. Yui Chan, J. Hao, Y. Hsu, H. Li, W. Guo, S. P. Lau, ACS Nano **7,** 7126-7131 (2013).

[83] H. Zhong, S. Gao, J. Shi, L. Yang, Phys. Rev. B **92,** 115438 (2015).

[84] H. R. Gutiérrez,N. Perea-López, A.L. Elías, A. Berkdemir, B. Wang, R. Lv, F. López-Urías, V. H. Crespi, H. Terrones, M. Terrones, Nano Lett. **13,** 3447−3454 (2013).

[85] B. Amin,T. P. Kaloni, U. Schwingenschl¨ogl; RSC Adv. **4,** 34561–34565 (2014).

[86] H. Sung, D. Choe, K. J. Chang, New J. Phys. **16,** 113055 (2014).

[87] A. K. Singh, R. G. Hennig, A. V. Davydov, A. Tavazza. Appl. Phys. Lett. **107,** 053106 (2015).

[88] S. Schönecker, X.-Q. Li, K. Koepernik, B. Johansson, L. Vitos, M. Richter, RSC Adv. **5,** 69680 (2015).

[89] Y. Feng, W. Zhou, Y. Wang, J. Zhou, E. Liu, Y. Fu, Z. Ni, X. Wu, H. Yuan, F. Miao, Phys. Rev. B **92,** 054110 (2015).

[90] S. J. Sandoval, D. Yang, R. F. Frindt, J. C. Irwin, Phys. Rev. B **44,** 3955 (1991).

Chapter 3

Thin film growth of van der Waals heterostructure of TMDs and BN

This chapter describes the growth of large area van der Waals heterostructure between. TMD and BN (where TMDs are MoS_2, WS_2, ReS_2) on c-plane sapphire substrate by PLD. The heterostructure stack is repeated from mono to multilayers of combinations along with stacks consisting different TMDs. The details structural investigation along with optical properties of such stacks are presented in this chapter.

This work has been published in the following journals:

1. ***B. Vishal**, U. Bhat, H. Sharona, A. Mukherjee and R. Datta, Heterostructures of hetero-stack of 2D TMDs (MoS_2, WS_2 and ReS_2) and BN, Manuscript under review Bulletin of Materials Science (2020).*

2. *U. Bhat, R. Singh, **B. Vishal,** A. Sharma, S. Horta,R. Sahu and R. Datta, physica status solidi (b) **255 (7),** 1700691 (2018).*

3.1 Introduction

Van der Waals heterostructures are artificial class of materials where various combination of 2D materials is used [1, 2]. This can be either stacked on top of each other called vertical van der Waals (vdW) heterostructure or zipped through the active side edge called planar heterostructure [1]. Many unique properties based on 2D materials such as graphene and TMDs show promising novel device applications [1, 3-6]. A. Geim *et al.* propose 2D crystals to be analogous to Lego blocks and construction of a huge variety of layered structures [Figure 3.01.(a)] [1]. As per transport properties, 2D vdW have wide range of material for example, Graphene has extreme ballistic properties and hope of shrinking the device dimension following Moore's law [2], semiconductors (e.g., MoS_2, WS_2, ReS_2, etc. which belong to the family known as transition metal dichalcogenides (TMDs)) insulator (*h*-BN) [8,9]. These vdW heterostructures (vertical or in-plane) of various vdW compounds and superlattices have emerged as a new class of material system with immense possibility of tuning the existing properties of the individual layer and exploring new physical phenomena [10-13]. The example of heterostructure devices of coupled quantum wells (CQW) and multiple quantum wells (MQW) is shown in Figure 3.01.(b) [14]. The motivation for research on van der Waals heterostructure got momentum after the demonstration of significant increase in the mobility of graphene on *h*-BN substrate [15]. *h*-BN substrate also increased the mobility of MoS_2, WSe_2 [16]. Moreover, insulation of graphene between *h*-BN sheets, mimicking the layered superconductor structure with greater scope for varying the materials parameters, exploration of fundamental physical phenomena e.g., Hofstadter butterfly effect in G/*h*-BN heterostructure, secondary Dirac points etc. have already been demonstrated [17-19].

Addition of TMDs, particularly MoS_2, WS_2, and ReS_2 in the library of useful 2D materials broadened the horizons of van der Waals heterostructure significantly. Integration of TMDs with *h*-BN and G, offers the possibility to investigate the fundamental physical phenomena e.g., Bose-Einstein Condensation (BEC) of excitons and to realize various novel heterostructure devices like field effect tunneling transistors based on G/*h*-BN & G/WS_2 vertical stacking [20,21], resonant tunneling diodes (MoS_2/BN), light emitting diodes, devices based on coupling between spin and valley degrees of freedom, strong light matter interaction and distinct exciton behavior [22,23].

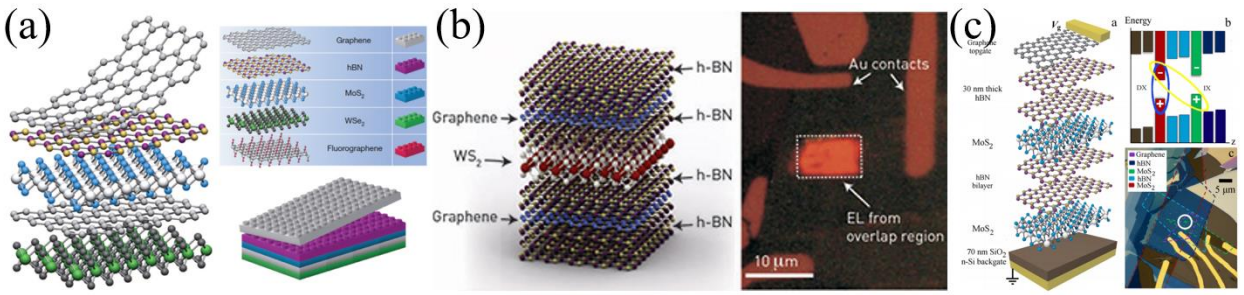

Figure 3.01*.(a) 2D crystals to be analogous to Lego blocks (right panel), the construction of a huge variety of layered structures becomes possible. Conceptually, this atomic-scale Lego resembles molecular beam epitaxy but employs different 'construction' rules and a distinct set of materials. Copyright by 2013 Springer Nature [1]. (b) Schematic diagram Heterostructure devices with MQW and Optical image of the device. Copyright by 2015 Springer Nature [14] (c) The coupled quantum well van der Waals heterostructure. Layer, and energy-band and diagrams with Microscope image showing the layer pattern of the device Copyright by 2016 AIP Publishing LLC. [23].*

Thinnest *p-n* junction based on MoS_2-WSe_2 vertical heterostructure has been demonstrated [24]. Among various device options, *p-n* junction forming type-II heterostructure can convert photon into e^--h^+ pairs and extremely useful for solar photovoltaic and photodetector applications [25-28]. Type-II heterostructure are based on various combinations of TMDs e.g., tuning the optical emission in MoS_2/WSe_2, MoS_2/WS_2, fast interlayer energy transfer in $MoSe_2/WS_2$ for optical amplification and energy harvesting have been demonstrated [29-31]. On the other hand, it is the type-I heterostructure which was reported to form between MoS_2-$ReS_2$with long charge transfer time of the order of 1ps [32]. The type-I heterostructure is suitable for optoelectronic devices like light emitting diodes (LEDs) and laser diodes (LDs). There are reports on the heterostructure between *h*-BN and TMDs [29, 33-35]. Electronic decoupling occurs between MoS_2/WSe_2 heterostructure with more than two layers of *h*-BN in-between. Theoretically, type-I heterostructure has been reported to form between *h*-BN and MoS_2. However, experimental verification on the formation of type-I heterostructure between TMDs and *h*-BN is not reported so far.

Nevertheless, arranging such vdW 2D-materials on top of each other or zipping on the sides is not straightforward. Early attempts involved a stacking procedure, first by isolating

individual layers on a thin transparent polymer film and sticking them face to face [36]. The steps are lengthy and prone to contamination at the interface between vdW layers. From the practical point of view, large area wafer scale thin film crystal growth methods like chemical vapor deposition (CVD), pulsed laser deposition (PLD), atomic layer deposition (ALD) are the viable options. Micrometer sized large crystals and their heterostructure of MoS_2/*h*-BN, have been grown by CVD [37-39]. PLD has been employed under slow kinetic condition to grow epitaxial films of MoS_2 and WS_2 over large area on *c*-plane sapphire substrate with control over layer numbers with the retention of substrate induced strain and resulting modification in the band gap [40,41]. The success of the slow growth kinetics of PLD has been extended further to deposit different multilayered heterostructure stacks of MoS_2/WS_2/ReS_2 and BN on *c*-plane sapphire substrate. Such stacks are essential not only for energy and optoelectronic applications but also to form coupled quantum wells (CQW) heterostructure. CQW provides a system to explore indirect excitons (IXs) which may form between the electrons and holes located at different layers separated by a distance [23,42]. IXs may originate quantum degenerate Bose gas Figure 3.01.(c)[23].

In this chapter, formation of large area vertical heterostructure between three different TMDs and *h*-BN is demonstrated with repeat between similar TMDs and different TMDs. Transmission electron microscopy imaging confirms the formation of such heterostructure systems. In case of similar TMD based structure a strong emission peak around 2.3 eV in the PL spectra irrespective of the TMD/BN system and is close to the most intense peak of the solar spectrum [43]. In case of stack of different TMD/BN heterostructure of hetero-stack [Table 2 and Figure 3.02], two strong emission peaks around near 2.13 eV and 2.16 eV for two hetero-stack TMD/BN, and three peaks near 2.13, 2.16 and 2.23 eV for three hetero-stack TMD/BN PL spectra is observed . Which indicate the each type of TMD stack is optically active. In the case of stack consisting of two or three different TMDs the intense peak split closely around 2.3 eV to two and three corresponding to number of different TMDs in the stack. The emission peaks observed are explained in terms of various band to band recombination processes and considering relative orientation of Brillouin Zones of TMDs and BN.

3.2 Experimental Methods

Different types of mixed vdW heterostructure of MoS_2 (or WS_2 or ReS_2)/BN/MoS_2 (or WS_2 or ReS_2)/BN were grown by PLD technique under slow kinetic condition are shown in Table 1. Before going to multiple stacks of TMD/BN, we try to grow a single stack of MoS_2 /BN and WS_2/BN, as proof of concept that "Growth of multiple stacks of TMD/BN is possible". We have categorized the vdW heterostructure in two types of growth as it is shown in Table 1. First Homo-stack of vdW heterostructure is a single type of TMDs stack with *h*-BN spacer, whereas in the hetero-stack of vdW heterostructure, different types of TMDs stack with *h*-BN were grown. MoS_2, WS_2, and *h*-BN target pellets were prepared from powders obtained from Sigma Aldrich (99.9% purity) by first cold pressing and then sintering at 500 °C for 5 hours in a vacuum chamber (~10^{-5} Torr). Sintering in the vacuum chamber prevents oxidation of compounds as well as re-deposition of vapor species back on the pellet surface unlike sintering performed in a sealed quartz tube. The ReS_2 target pellets were prepared following a procedure already reported in '**Chapter 2** Experimental Methods' and reported by K. Dileep *et al.* [44].

Table1. List of the vdW heterostructure with different type of homo and Hetero-stacking on sapphire substrate grown by PLD.

Homo-stack of vdW Heterostructure	MoS_2/BN/MoS_2/BN
	WS_2/BN/WS_2/BN
	ReS_2/BN/ReS_2/BN
Hetero-stack of vdW Heterostructure	MoS_2/BN/WS_2/BN
	MoS_2/BN/ReS_2/BN
	MoS_2/BN/WS_2/BN/ReS_2/BN

The epitaxial growth method of all the heterostructure was followed from the procedure based on PLD already developed for epitaxial growth of MoS_2 and WS_2 thin films on the *c*-plane sapphire substrate [41]. However, the number of pulses required to control layer numbers were further optimized for the growth of different TMDs and BN layers on top of each other. Kindly note that the PLD method was not utilized before to grow such van der Waals heterostructure, which was done either by physically stacking layers on top of each other or by CVD process to grow only two different layers [36, 37-39].. The laser ablation frequency was 1 Hz to ensure smooth film of such vdW layers with the underlying substrate and layers on top of each other. The

number of layers of TMDs was one and in-between, one to four layers of *h*-BN were deposited. The top layer was encapsulated with *h*-BN layer to minimize external interaction.

Cross sectional transmission electron microscopy (TEM) specimen preparation was carried out by first mechanical polishing and then Ar ion milling to perforation to generate large electron transparent thin area. Following a procedure already reported in '**Chapter 2** Experimental Methods'. Special care was taken during sample preparation to maintain the vdW stacks intact which is otherwise extremely difficult as they delaminate with slight shear. Imaging was carried out, using double C_s aberration-corrected transmission electron microscope. Raman spectra were recorded using a custom-built Raman spectrometer using a 514.5 nm laser excitation and grating of 1800 lines/mm at room temperature. The laser power at the sample was approximately 1mW. Micro PL measurement was performed in a dedicated micro PL instrument at 325 nm excitation (He-Cd laser) with grating of 1200 lines/mm.

3.3 Results and Discussion

We have grown three major types of vdW heterostructure, Single-stack, Homo-stack, and Hetero-stack of vdW Heterostructure with two and three stacks of TMDs. Schematic representation of vdW heterostructure with different types of homo and Hetero-stacking on sapphire substrate is shown in Figure 3.02. Single-stack are (i) MoS_2/BN and (ii) WS_2/BN. Single stack growth is done to confirm that "growth of multiple stack of TMDs/BN is possible" for fabrication of homo-stack of MoS_2/BN/MoS_2/BN, WS_2/BN/WS_2/BN and ReS_2/BN/ReS_2/BN CQW grown by PLD. Furthermore, for Hetero-stack mixed TMDs stack has been fabricated such as MoS_2/BN/WS_2/BN, MoS_2/BN/ReS_2/BN and three stack MoS_2/BN/WS_2/BN/ReS_2/BN. The final growth scheme for of vdW heterostructure with different type of homo and Hetero-stacking on sapphire substrate is shown in Figure 3.03.

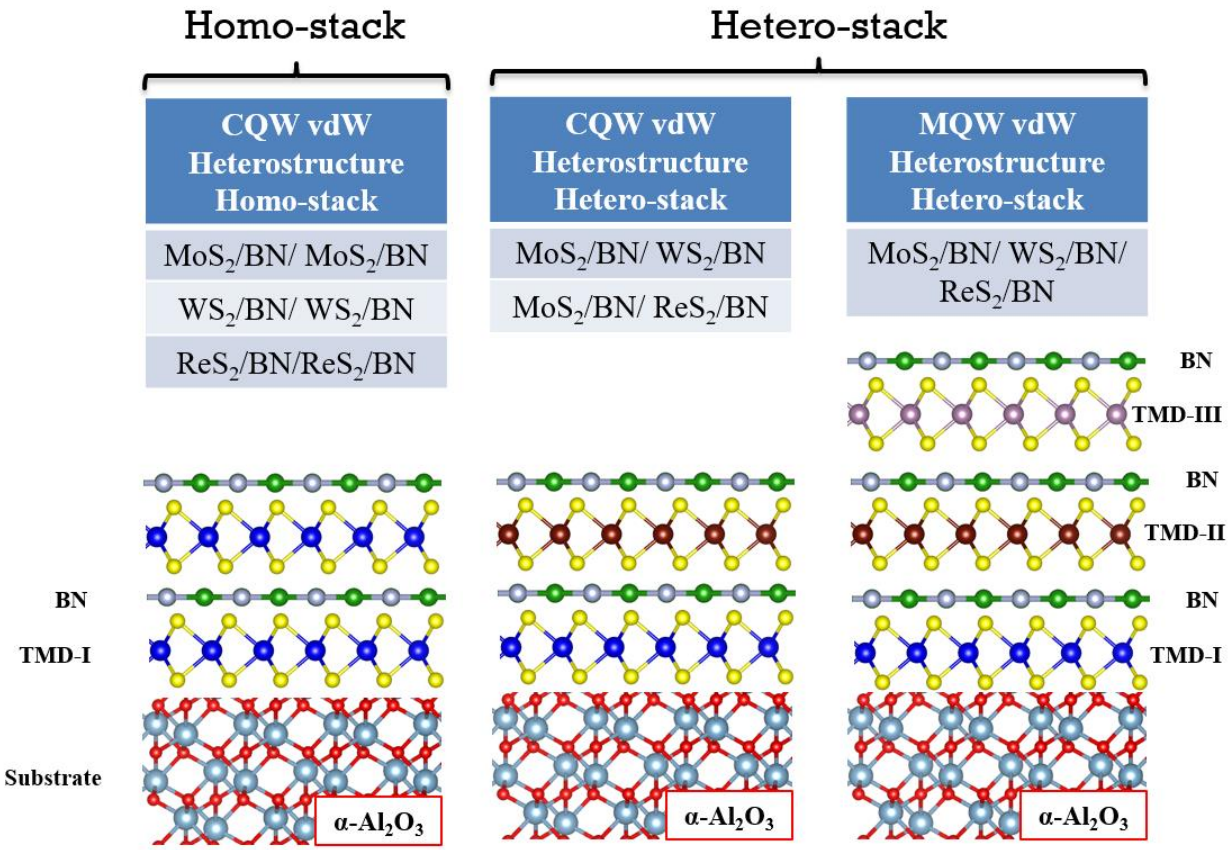

Figure 3.02. *Schematic representation of vdW heterostructure with different type of homo and Hetero-stacking on sapphire substrate.*

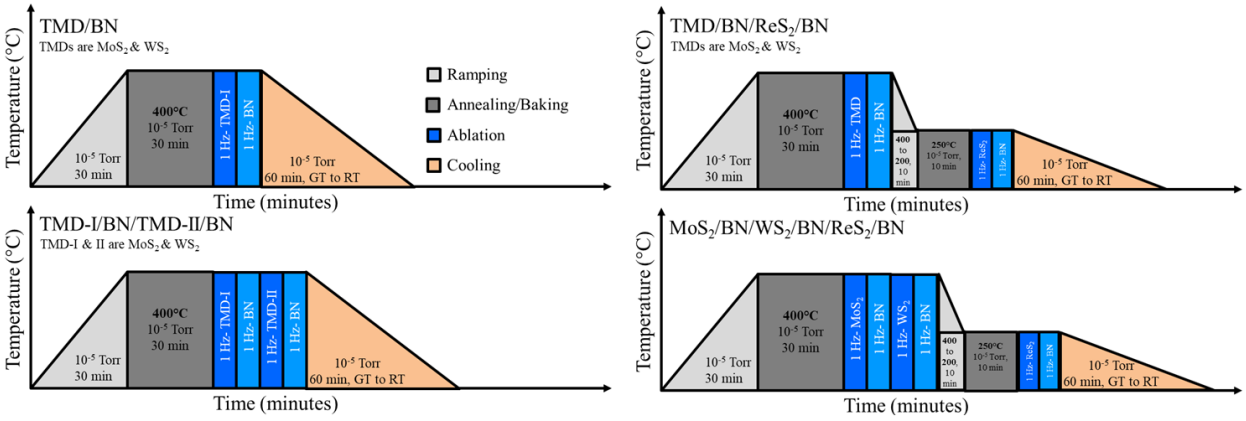

Figure 3.03. *The final growth scheme for of with different type of Single-stack, homo-stack, and Hetero-stack of vdW heterostructure on sapphire substrate by PLD.*

3.3.1 vdW Heterostructure Single-stack

3.3.1.1 MoS_2/BN

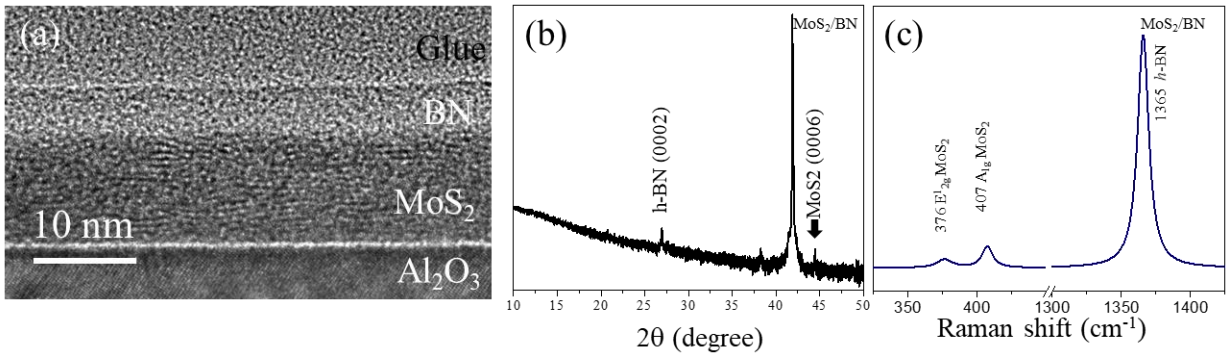

Figure 3.04*.(a) HRTEM image of Single-stack heterostructure MoS_2/BN with (b) XRD and (c) Raman spectra.*

HRTEM image confirms the uniform flat growth of Single-stack MoS_2/BN heterostructure shown in Figure 3.04.(a), and XRD confirms the same [Figure 3.04.(b)]. Flat growth confirms the possibility of growth of heterostructure in the top of the BN. Which is a great opportunity to fabrication for device application by PLD. Raman spectra of BN layers deposited on top of MoS_2 and WS_2 are displayed in Figure 3.04.(c) and Figure 3.05.(c) . It is found that the crystal structures of BN grown on top of MoS_2 and WS_2 are different depending on the type of the TMD compound; *h*-BN on MoS_2, mixture of *c*-BN and *w*-BN on WS_2 and ReS_2.

The Raman spectra of powder *h*-BN, *c*-BN, and *w*-BN from ref. 45 is used for better understanding [45]. The peak around 1370 cm^{-1} corresponds to the *h*-BN structure. For *c*-BN there are two distinct peaks around 1057 and 1309 $cm^{-1}$and many broad peaks appear in case of *w*-BN structure [45,46]. The Raman spectra of *w*-BN are scarce, and identification of all the peaks requires further investigation. In the present heterostructure samples, the BN films grown on MoS_2 shows peak around 1365 cm^{-1} confirming the hexagonal structure [Figure 3.04.(c)].

3.3.1.2 WS_2/BN

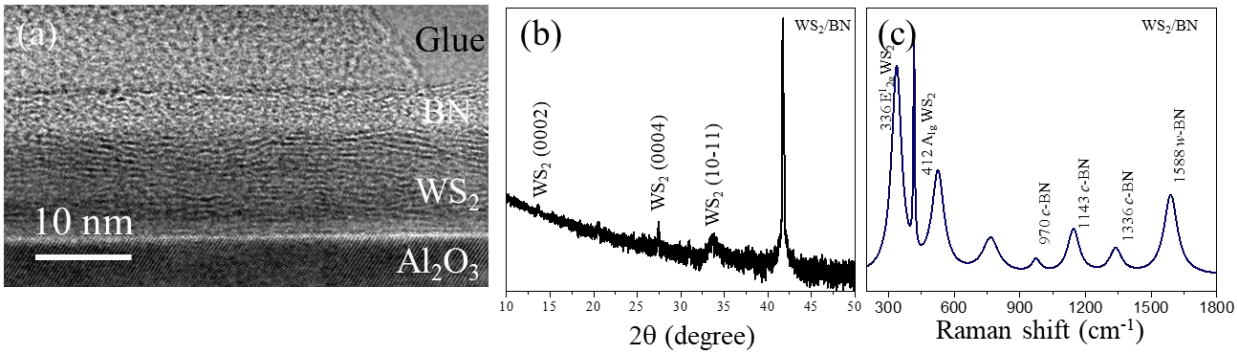

Figure 3.05*. (a) HRTEM image of Single-stack heterostructure WS_2/BN with (b) XRD and (c) Raman spectra.*

Similar to MoS_2/BN, Single-stack heterostructure WS_2/BN show the uniform flat growth by HRTEM [Figure 3.05.(a)]. XRD confirm the same [Figure 3.04.(b)]. Flat growth confirm the possibly of growth of heterostructure in top of the BN. Which is great opportunity to fabrication for device application by PLD. The Raman peaks of BN grown on WS_2 and ReS_2 matches closely with the *c*-BN and *w*-BN structures [Figure 3.05.(c)].

3.3.2 vdW Heterostructure Homo-stack

3.3.2.1 MoS_2/BN/MoS_2/BN

Homo-stack of vdW-heterostructure MoS_2/BN/MoS_2/BN grown by PLD with varying number single and multilayer of BN and TMD [Figure 3.06.]. The multilayer of BN layers in between TMDs and on top of the TMD layer is grown to form the heterostructure. The low magnification TEM image of the multilayer confirms the large area growth of heterostructure [Figure 3.06.(a)]. HRTEM confirm flat formation MoS_2 and BN [Figure 3.06.(b)]. Formation of single layer thick HRTEM of vdW heterostructure confirm our control of PLD system, and good for thinnest practical device application [Figure 3.06.(b)]. It is extremely difficult to prepare cross section TEM specimens with few layers of layered materials on the substrate as they are found to be delaminated unless extreme care is taken [41]. As already mentioned, the number of layers of different materials can be controlled with the laser ablation frequency under slow kinetic growth

condition and for example HRTEM images of scaled-up version of such heterostructure are given in the supporting information. The photoluminescence (PL) spectra at room temperature for MoS_2/BN/MoS_2/BN show five distinct peaks labeled as A, B, C, D, and E around 435 (2.85), 532 (2.33), 595 (2.08), 720 (1.72) and 845 (1.47) nm (eV), respectively [Figure 3.06.(d)]. For other two systems of homo-stack CQW, almost similar peak positions are observed shown in Figure 3.07.(d) and Figure 3.08.(c) for WS_2/BN/WS_2/BN and ReS_2/BN/ReS_2/BN, respectively . Theoretical understanding of origin of PL emission will be discuss in latter in section **3.3.3.4.**

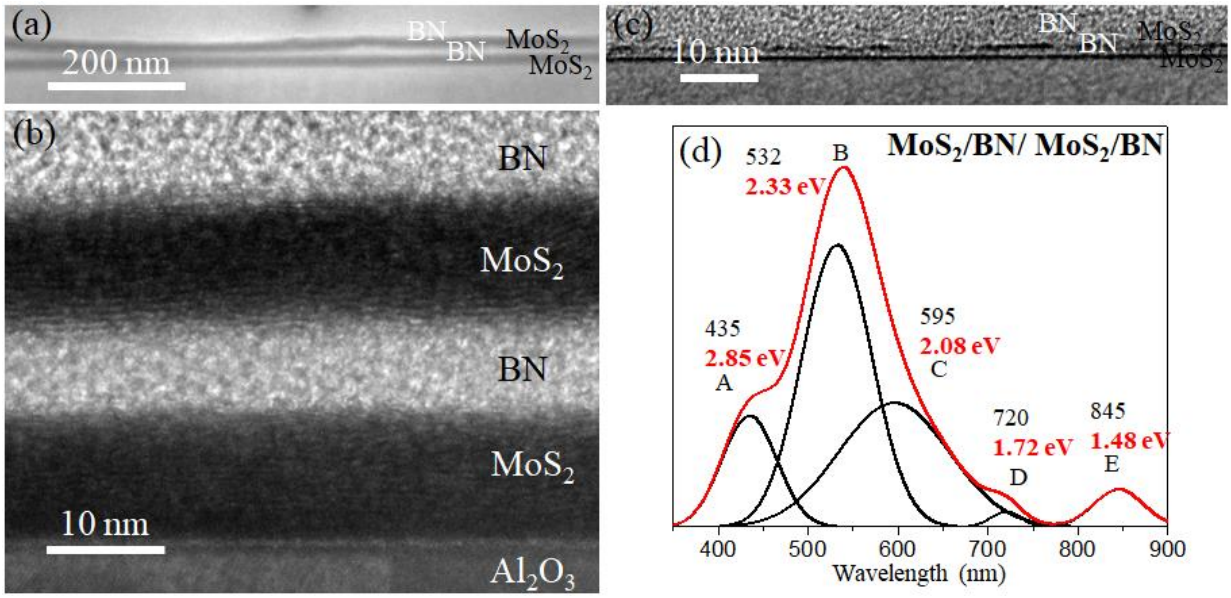

Figure 3.06*. (a) Low magnification TEM image and (b) HRTEM of homo-stack multi-layer thick vdW heterostructureMoS_2/BN/MoS_2/BN on sapphire substrate. (c) single layer thick HRTEM of vdW heterostructure . (d) Photoluminescence (PL) spectra at room temperature for MoS_2/BN/MoS_2/BN. Copyright 2018 by WILEY-VCH Verlag GmbH & Co. KGaA, Weinheim [43].*

3.3.2.2 WS_2/BN/WS_2/BN

Homo-stack of vdW heterostructures WS_2/BN/WS_2/BN grown by PLD with single and multilayer of BN and TMD shown in Figure 3.07. Low magnification TEM image of the multilayer confirm the large area growth of heterostructure [Figure 3.07.(a)]. HRTEM confirm flat formation

WS_2 and BN [Figure 3.06.(b)]. Formation of single layer thick HRTEM of WS_2/BN/WS_2/BN confirm our control of PLD [Figure 3.07.(c)]. The photoluminescence (PL) spectra at room temperature for WS_2/BN/WS_2/BN show in Figure 3.06.(d). Theoretical understanding of origin of PL emission will be discuss in latter in section **3.3.4.**

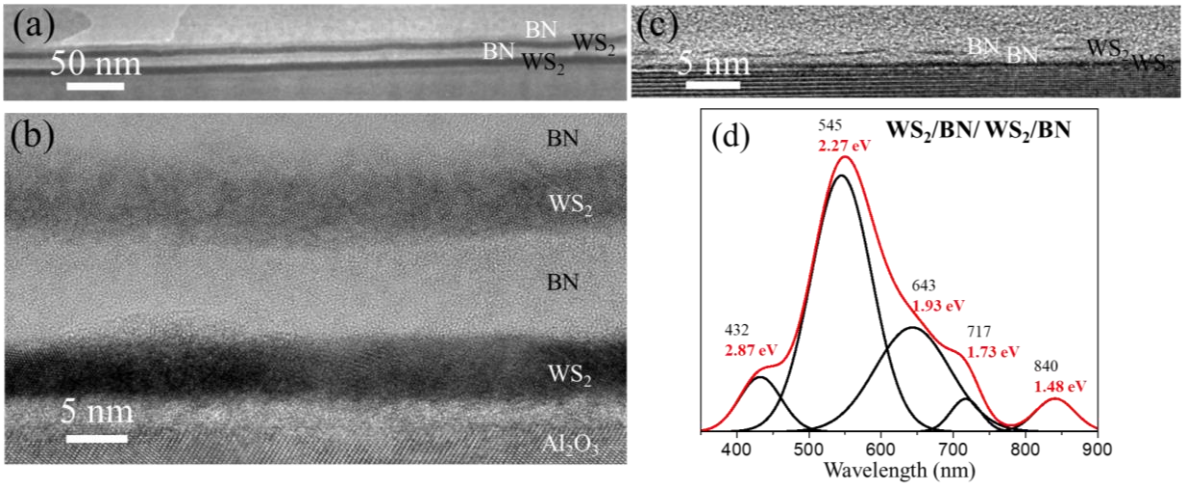

Figure 3.07*.(a) Low magnification TEM image and (b) HRTEM of homo-stack multi-layer thick vdW heterostructure WS_2/BN/WS_2/BN on sapphire substrate .(c) single layer thick HRTEM of vdW heterostructure .(d) Photoluminescence (PL) spectra at room temperature for WS_2/BN/WS_2/BN. Copyright 2018 by WILEY-VCH Verlag GmbH & Co. KGaA, Weinheim [43].*

3.3.2.3 ReS_2/BN/ReS_2/BN

Multilayer vdW-heterostructure ReS_2/BN/ReS_2/BN shown in Figure 3.08. Low magnification TEM image of the multilayer confirm the large area growth of heterostructure [Figure 3.08.(a)]. HRTEM confirm flat formation ReS_2 and BN [Figure 3.08.(b)]. The photoluminescence (PL) spectra at room temperature for WS_2/BN/WS_2/BN show in Figure 3.08.(c). Theoretical understanding of origin of PL emission will be discuss in latter in section **3.3.4.**

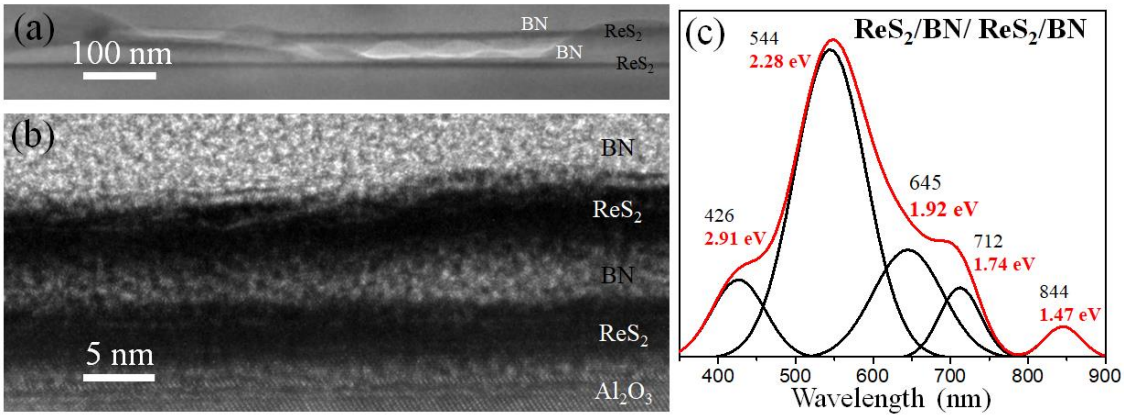

Figure 3.08*.(a) Low magnification TEM image of homo-stack vdW heterostructure ReS_2/BN/ReS_2/BN on sapphire substrate.(b) Schematic diagram of vdW heterostructure on sapphire substrate. (c) Photoluminescence (PL) spectra at room temperature for WS_2/BN/WS_2/BN. Copyright 2018 by WILEY-VCH Verlag GmbH & Co. KGaA, Weinheim [43].*

3.3.3 vdW Heterostructure Hetero-stack

3.3.3.1 MoS_2/BN/WS_2/BN

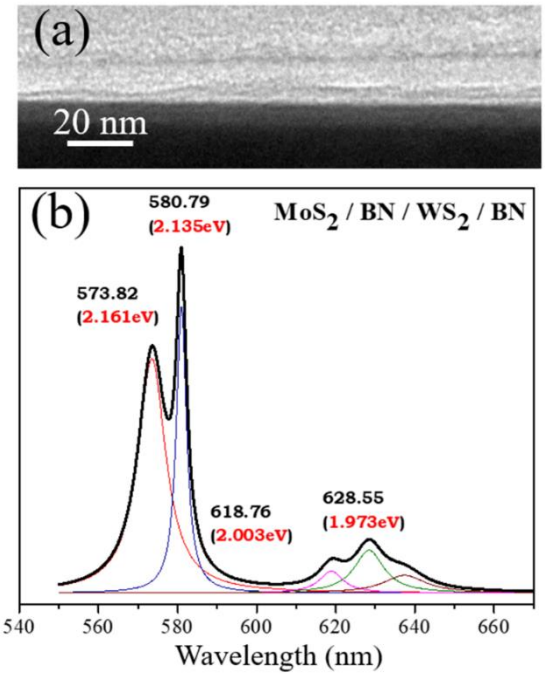

Figure 3.09*. (a) TEM image of Hetero-stack vdW heterostructure MoS_2/BN/WS_2/BN on sapphire substrate. (b) Photoluminescence (PL) spectra at room temperature for MoS_2/BN/WS_2/BN.*

TEM image of Hetero-stack vdW heterostructure MoS_2/BN/WS_2/BN on sapphire substrate shown in Figure 3.09.(a). The photoluminescence (PL) spectra at room temperature for WS_2/BN/WS_2/BN show in Figure 3.09.(b). Theoretical understanding of origin of PL emission will be discuss in latter in section **3.3.4.** Observes major PL emission peak around 580.79 (2.13) and 573 nm (2.16 eV) confirms the both stack layers of TMMs are active and good for optoelectronic application.

3.3.3.2 MoS_2/BN/ReS_2/BN

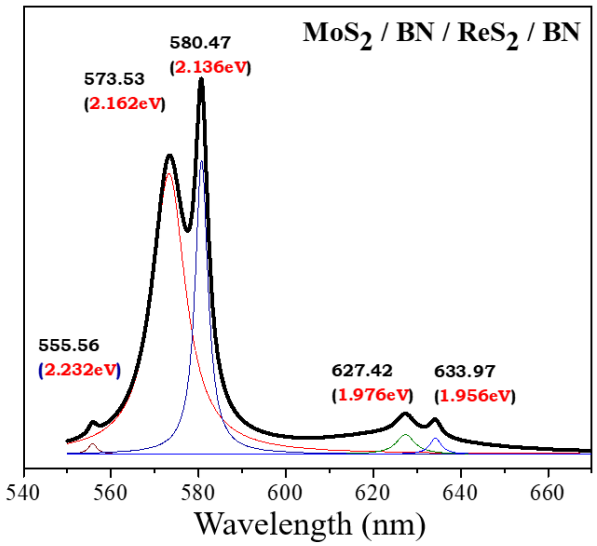

Figure 3.10. *Photoluminescence (PL) spectra at room temperature for MoS_2/BN/ReS_2/BN.*

The photoluminescence (PL) spectra at room temperature for WS_2/BN/ReS_2/BN show in Figure 3.10. Theoretical understanding of origin of PL emission will be discuss in latter in section **3.3.4.** Observes major PL emission peak around 580.47 (2.14) and 573 nm (2.16 eV) confirms the both stack layers of TMDs are active and good for optoelectronic.

3.3.3.3 MoS_2/BN/WS_2/BN/ReS_2/BN

TEM image of three stack of vdW heterostructure MoS_2/BN/WS_2/BN/ReS_2/BN on sapphire substrate shown in Figure 3.11.(a) .The photoluminescence (PL) spectra at room temperature for WS_2/BN/ReS_2/BN show in Figure 3.11.(b). Theoretical understanding of origin of

PL emission will be discuss in latter in section **3.3.4.** Observes major PL emission peak around 555.7 (2.14), 575.4 (2.15) and 592 nm (2.09 eV) confirms the all three stack of MoS_2, WS_2, ReS_2 layers are active and good for optoelectronic.

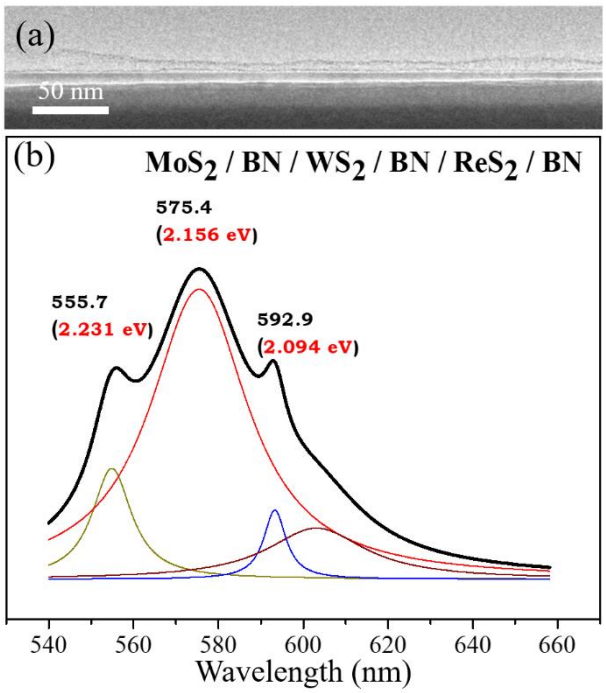

Figure 3.11*.(a) TEM image of three stack vdW heterostructure MoS_2/BN/WS_2/BN/ReS_2/BN on sapphire substrate.(b) Photoluminescence (PL) spectra at room temperature for MoS_2/BN/WS_2/BN/ReS_2/BN.*

PL spectra are obtained for three different TMD Homo-stack heterostructure systems, irrespective of the structure of BN. During this study, it is also found that BN grows with wurtzite structure directly on the sapphire and details of the findings can be found in Ref. 46 and Chapter 4 of the thesis. The results show that the various crystal forms of BN can be controlled with the choice of different TMD materials as a template. The results are interesting as it is known that the synthesis of *c*-BN and *w*-BN requires extreme temperature and pressure conditions like diamond [47,48].

3.3.4 Theoretical Origin of PL emission

The theoretical origin of the PL emission is described by allowed emission across the bandstructure of the particular heterostructure system. In the case of homo or hetero-stack two type of emission is possible, first emission occur between TMD and BN (MoS_2/BN), or inter-stack exciton emission (BEC excitons) occur between two TMDs, or both [20,21]. Rigorous and careful theoretical study is request to understand the exact nature of emission. BEC excitons emission are ultrafast and can be detected by the life time and absorption experiment. Here is our effort in case of emission originated from TMD and BN.

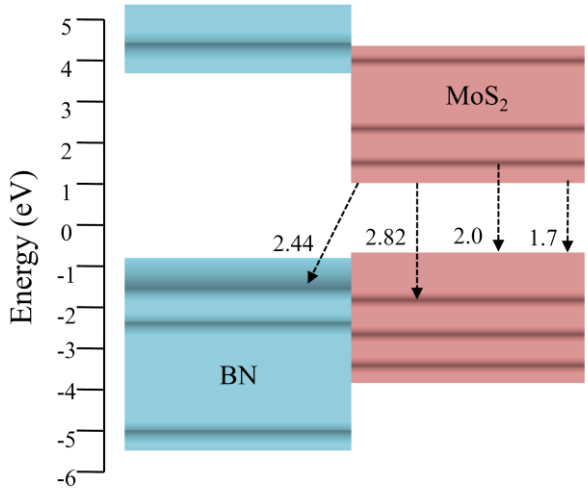

***Figure 3.12**. Schematic transitions between BN and MoS_2 valence and conduction levels [34, 35]. (The corresponding DOS and band structures are given in **Figure 3.13.**). Copyright 2018 by WILEY-VCH Verlag GmbH & Co. KGaA, Weinheim [43].*

The photoluminescence spectra at room temperature for three different homo-stack heterostructure with varying number of BN layers show five distinct peaks labeled as A, B, C, D, and E around 435 (2.85), 532 (2.33), 595 (2.08), 720 (1.72) and 845 (1.47) nm (eV), respectively for MoS_2/BN/MoS_2/BN heterostructure system. For other two homo-stack systems, almost similar peak positions are observed [Figure 3.06.(d), Figure 3.07.(d), Figure 3.08.(c)]. The various peak positions and full width at half maxima (FWHM) for different Homo-stack heterostructure systems

are given in Table 2. Moreover, the PL spectral patterns are almost similar irrespective of the number and crystal structure of BN layers deposited in between the TMDs.

Table 2. Experimental peak positions and FWHM of various peaks of different Homo-stack heterostructure systems. *Copyright 2018 by WILEY-VCH Verlag GmbH & Co. KGaA, Weinheim [43].*

TMDs	A		B		C		D		E	
	Peak (nm)	FWHM (nm)	Peak (nm)	FWHM (nm)	Peak (nm)	FWHM (nm)	Peak (nm)	FWHM (nm)	Peak (nm)	FWHM (nm)
MoS_2	435	61.25	532	77.69	595	123.22	720	35.14	845	56.18
WS_2	432	58.2	545	84.09	643	103.60	717	41.44	840	54.52
ReS_2	426	57.78	544	98.93	645	91.23	712	52.36	844	50.42

The band gap differences of MoS_2, WS_2 are approximately 0.04 eV [49]. This translates into ~ 13 nm shift in the PL peak positions. In case of MoS_2/ReS_2 system the difference is 0.46 eV [44]. Though, relative peak intensities are found to be slightly different with different number of BN layers, no clear trend was observed. The heterostructure band alignments might have little difference between various TMDs/BN systems and responsible for almost similar pattern in the PL spectra.

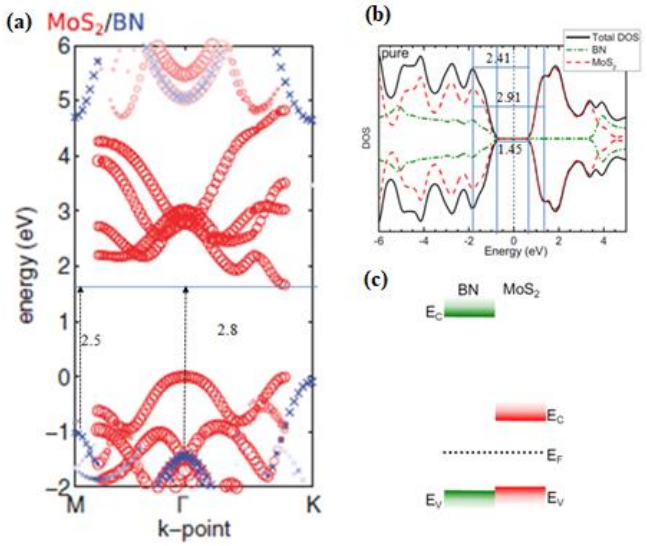

Figure 3.13. *Calculated (a) band structure and (b) DOS, and (c) schematic energy band levels of MoS_2/BN heterostructure system taken from Ref. 34 & 35. All the possible transitions between BN and MoS_2 are marked in the diagram. Calculation predicts a type-I heterostructure formation in*

this system. Copyright 2014 by American Physical Society [34]. Copyright 2013 by American Physical Society [35].

Among five different peaks, peak B is the most intense, followed by peak C, A, E and D [Figure 3.06.(d), Figure 3.07.(d), Figure 3.08.(c)]. This is consistent between various heterostructure systems. To understand the origin of different peaks, electronic structure calculations based on the MoS_2/BN heterostructure is considered [34, 35]. The calculated band structure and density of states (DOS) of MoS_2/BN heterostructure are shown in Figure 3.13. The dominant transitions are marked between various valence bands to conduction band states and the schematic transitions levels derived from this is shown in Figure 3.12. The calculation predicted type-I heterojunction between MoS_2 and *h*-BN system and similar heterojunction can be expected in case of WS_2 and ReS_2 based systems as well. The valence band maxima of MoS_2 in the partial density of states (PDOS) is higher than that of *h*-BN by about 0.05 eV, which is significantly smaller compared to the difference in conduction band minima levels by about 3.1/3.55eVpredicted by PBE+D2/HSE12 functional. In the schematic energy band diagram [Figure 3.12.] the band gap of *h*-BN and MoS_2 are 4.82/6.05 and 1.75/2.5 eV, respectively, which are estimated by PBE+D2/HSE functional [35].

Monolayer MoS_2 has a direct band gap of 1.98 eV at K point and indirect band gap of 1.78 eV at $\Gamma \longrightarrow K$ point [44,50-51]. Whereas, theoretical calculation of *h*-BN shows direct and indirect transitions at 5.97 eV and 5.95 eV points [52-53]. For the MoS_2/*h*-BN heterostructure, three possible transitions have been identified from the calculated band structure, these are: 2.85 eV at $\Gamma \longrightarrow K$, 2.54 eV at $M \longrightarrow K$, and 1.57 eV at $K \longrightarrow K$ points [Figure 3.13.] [34]. the first two transitions at 2.5 and 2.8 eV are also marked in the DOS of the compound MoS_2/*h*-BN system. Now from the various transitions as marked in the combined DOS of the MoS_2/*h*-BN heterostructure system, transitions at 2.8 and 2.3 eVs can be assigned to the peak A and B of the PL spectra, respectively. Peak C and D at 2.1 and 1.72 eV can be assigned to the MoS_2 *B* and *A* excitons, which in general observed at 1.95 and 1.8 eV respectively [44].

The difference in peak values between reported and present values (peak C and D) may be because of relative rotation between the layers in the heterostructure system, unknown effects like impurities, oxide layers and presence of charges [54-55]. The low energy peak around 1.47 eV could be because of defects or edge state levels for the combined system. For MoS_2 and WS_2 defect related spectral feature 0.1 eV below the excitonic peak and enhanced photoluminescence from defects have been reported and for ReS_2 no changes in photoluminescence due to defect is reported [56-58]. In the present heterostructure systems planar faults due to discontinuous Mo atoms are commonly observed and could also be responsible for the emission peak around 1.47 eV. The proposal is viable as BN can be doped both *p* and *n* type and $MoS_2/WS_2/ReS_2$ can be doped *n* type, therefore, charge extraction is possible. Subsidiary peaks around 2.8, 1.9, 1.7 and 1.5 eV are also observed with reduced intensity.

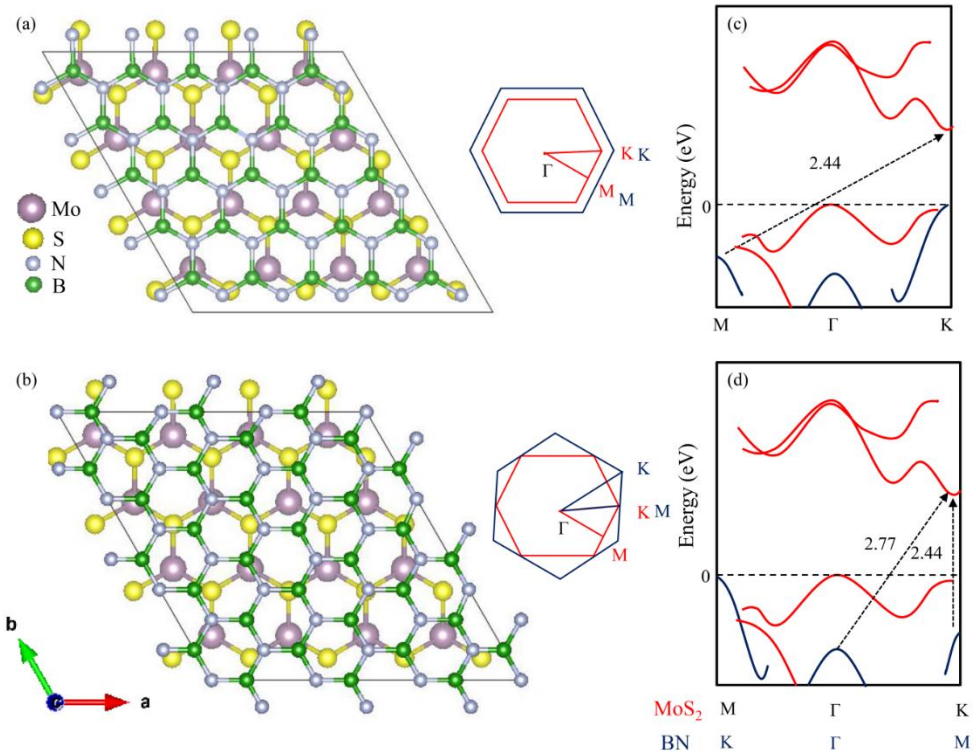

Figure 3.14. *Two different h-BN stacking on MoS_2 (a) $\Gamma \rightarrow K\ (BN) \parallel \Gamma \rightarrow K(MoS_2)$ and (b) $\Gamma \rightarrow K\ (BN) \parallel \Gamma \rightarrow M(MoS_2)$. Corresponding schematic band structures are shown in (c) and (d), respectively. Kindly note the relative VBM and CBM positions between the two layers with respect to relative rotation between them. Copyright 2018 by WILEY-VCH Verlag GmbH & Co. KGaA, Weinheim [43].*

The room temperature broadening of PL peaks of any semiconductor is important as this directly affects the performance of LEDs, LDs and other devices. The FWHM of all the peaks is broader compared to the typical broadening observed for the emission from monolayer MoS_2, WS_2 and ReS_2 [Table 2]. The room temperature broadening of PL peaks of the quantum wells semiconductors may be due to following possibilities; strong exciton-phonon interaction at room temperature, increase in thermal population at higher electron and hole energy levels, scattering by longitudinal-optical (LO) phonons, average well width fluctuations and associated quantum coupling effect, scattering due to impurities, dopants and longitudinal acoustic (LA) phonons [59]. The variation in thickness of BN barrier layers and MoS_2 layers can be expected in the PLD grown TMD/BN heterostructure system [Figure 3.07.(a)]. Two vastly different atoms and crystal lattices of TMDs and BN may contribute to the broadening of the PL peaks. Moreover, encapsulation of MoS2 by *h*-BN was predicted to increase the dissociation rate of excitons which may also contribute to the broadening of the emission peaks [60]. Therefore, the fluctuation of well and barrier width, longitudinal phonon scattering at room temperature and momentum vector mismatch may have contributed to the observed PL peak broadening.

Now the most intense peak at 2.31 eV in case of MoS_2/*h*-BN system and similar peaks for other two systems can be understood as follows; as already mentioned, the difference between the valence band edges of TMDs and BN is very small i.e. 0.05 eV. Therefore, the valence band edge of the compound TMD/BN systems has contributions from both TMDs and BN. However, with increasing number of BN layers in-between and above the TMDs layer, the valence band is expected to be dominated by the BN DOS. Though, previous results [34] suggest that the transition at 2.3 at $M \longrightarrow K$ is an indirect transition and should not be most intense for the compound system where at $K \longrightarrow K$ (1.57 eV) direct transition exists. However, the calculation was carried out with a specific stacking of *h*-BN on MoS_2 where the respective Brillouin zones have same orientation. In fact, the energy difference is negligible between various stacking arrangement between *h*-BN and MoS_2 because of the weak quantum mechanical interaction between the two systems, which is mostly van der Waals in nature. Quantum coupling (QC) may lead to unique properties due to electronic coupling, and in the present case it is the distinct PL emission. Here, due to misorientation of BN and TMD layers (with preferable rotation angle 30º), M-point of BN coincides with the K-point of MoS_2 during the formation of the heterostructure. The transition

from M ⟶ K , which is direct, results in the intense peak. The corresponding Brillouin zones for the system are shown in Figure 3.14.(a) and (b) with the resulting band structure in Figure 3.14.(c) and (d). As we could not verify the relative orientations between the h-BN and TMDs in our experimental heterostructure systems, therefore we anticipate based on the PL intensity peak and theory calculation that the orientation between the two crystal layers is according to Figure 3.14.(d). This explains strong emission peak around 2.3 eV in the PL spectra. The transition at 2.8 eV is between the VBM at Γ point of *h*-BN to the CBM at K point of MoS_2. In addition to this, the effect of electric dipole due to defects can tilt the balance from indirect to direct transitions [34,61].

In summary, every PL emission can be explained by bandstructure of vdW heterostructure and to calculate bandstructure of vdW heterostructure, it is very important to know that exact nature of TMDs, no. of layers, type of stacking between BN and TMD, orientation/angle between layers of BN and TMD is very important. For future study, experiment plan view TEM sample preparation by very carefully by lifting off the layers on a grid to study the relative alignment by electron diffraction can provide above information.

3.4 Conclusion

In conclusion, large area growth of heterostructures of three different TMD and BN layers by PLD is demonstrated. The layer numbers of in both homo-stack and hetero-stack can be controlled by PLD, which is good for fine tuning during fabrication of devices. Raman spectra shows BN can form with different crystal structure depending on the type of TMD as template layer. For heterostructure PL spectra show strong emission around 2.3 eV, whereas Hetero-stack give PL response near 2.13 eV from each stack of TMD. The origin of the PL emission can be explained by the bandstructure of the heterostructure. The PL response suggest all vdW heterostructure are optically active material and maybe a good candidate for solar photovoltaic application.

3.5 Bibliography

[1] A. Geim and I. V. Grigorieva, Nature **499**, 419-425 (2013).

[2] A. K. Geim, K. S Novoselov, Nat. Mater. **6**, 183−191 (2007).

[3] G. Eda and S. A. Maier, ACS Nano **7**, 5660 (2013).

[4] M. Pumera, Z. Sofer, A. Ambrosi, J. Mat. Chem.A.**2**, 8981 (2014).

[5] M.R.Gao, Y.F. Xu, J. Jiang, and S.H. Yu, Chem. Soc. Rev. **42**, 2986(2013).

[7] G. E. Moore, Proc. IEEE **86**, 82 (1998).

[8] Q. H. Wang, K.K. Zadeh, A. Kis, J. N. Coleman and M. S. Strano, Nat. Nanotechnol.**7**, 699 (2012).

[9] H. S. S. R. Matte, B. Plowman, R. Datta and C. N. R. Rao, Dalton Trans. **40**,10322 (2011).

[10] G. Gao, W. Gao, E. Cannuccia, J. T. Tijerina, L.Balicas, A.Mathkar, T. N. Narayanan, Z. Liu, B. K. Gupta, J. Peng, Y. Yin, A. Rubio and P. M. Ajayan, Nano lett. **12**, 3518 (2012).

[11] C. Gong, H. Zhang, W. Wang, L. Colombo, R. M. Wallace and K. Cho, Appl. Phys. Lett.**103**, 053513 (2013).

[12] Y. Gong, J. Lin, X. Wang, G. Shi, S. Lei, Z. Lin, X. Zou, G. Ye, R. Vajtai, B. I. Yakobson, H.Terrones, M. Terrones, B. K. Tay, J. Lou, S. T. Pantelides, Z. Liu, W. Zhou and P. M. Ajayan,Nat. Mat.**13**, 1135 (2014).

[13] K. Chen, X. Wan, W. Xie , J. Wen , Z. Kang , X. Zeng,H. Chen and J. Xu, Adv. Materials **27**, 6431 (2015).

[14] F. Withers, O. Del Pozo-Zamudio, A. Mishchenko, A. P. Rooney, A. Gholinia, K. Watanabe, T. Taniguchi, S. J. Haigh, A. K. Geim, A. I. Tartakovskii & K. S. Novoselov, *Nat. Mater.* **14**, 301 (2015).

[15] C. R. Dean, A. F. Young, I. Meric, C. Lee, L. Wang, S. Sorgenfrei, K. Watanabe, T.

Taniguchi, P. Kim, K. L. Shepard and J. Hone, Nat. Nanotechnol. **5**, 722 (2010).

[16] S.M. Kim, A. Hsu, M.H. Park, S.H. Chae, S.J. Yun, J.S. Lee, D.H. Cho, W. Fang, C. Lee, T. Palacios and M. Dresselhaus, Nat. Ccommun. **6**, 8662 (2015).

[17] A. Ramasubramaniam, D. Naveh and E. Towe, Nano Lett., **11**, 1070 (2011).

[18] B. Hunt, J.D. Sanchez-Yamagishi, A.F.Young, M. Yankowitz, B.J. LeRoy, K. Watanabe, T. Taniguchi, P. Moon, M. Koshino, P. Jarillo-Herrero and R.C. Ashoori, Science, **340**, 1427 (2013).

[19] G. L. Yu, R. V. Gorbachev, J. S. Tu, A. V. Kretinin, Y. Cao, R. Jalil, F.Withers, L. A. Ponomarenko, B. A. Piot, M. Potemski, D. C. Elias, X. Chen, K.Watanabe, T. Taniguchi, I. V. Grigorieva, K. S. Novoselov, V. I. Fal'ko, A. K. Geim and A. Mishchenko, Nat. Phys. **10**, 525 (2014).

[20] L. Britnell, R. V. Gorbachev, R. Jalil, B. D. Belle, F. Schedin, A. Mishchenko, T. Georgiou, M.I. Katsnelson, L. Eaves, S. V. Morozov, N. M. R. Peres, J. Leist, A. K. Geim, K. S. Novoselov and L. A. Ponomarenko, Science **335**, 947(2012).

[21] T. Georgiou, R. Jalil, B. D. Belle, L. Britnell, R. V. Gorbachev, S. V. Morozov, Y. J. Kim, A. Gholinia, S. J. Haigh, O. Makarovsky, L. Eaves, L. A. Ponomarenko, A. K. Geim, K. S. Novoselov and Artem Mishchenko, Nat. Nanotechnol. **8**, 100 (2013).

[22] P. M. Campbell,A. Tarasov, C. A. Joiner, W. J. Ready and E. M. Vogel, J. Appl. Phys. **119**, 024503 (2016).

[23] E. V. Calman,C. J. Dorow, M. M. Fogler, L. V. Butov, S. Hu, A. Mishchenko and A. K. Geim, Appl. Phys. Lett. **108**, 101901 (2016).

[24] C. H. Lee, G. H. Lee, A. M. van der Zande, W. Chen, Y. Li, M. Han, X. Cui, G.Arefe, C.

Nuckolls, T. F. Heinz, J. Guo, J. Hone and P. Kim, Nat. Nanotechnol. **9**, 676 (2014).

[25] J. Chu, F. Wang, L. Yin, L. Lei, C. Yan, F. Wang, Y. Wen, Z. Wang, C. Jiang, L. Feng, J. Xiong, Y. Li and J. He, Adv. Functional Materials, **27**, 1701342 (2017).

[26] Y. Wen,L. Yin,P. He,Z. Wang,X. Zhang,Q. Wang, T. A. Shifa,K. Xu,F.Wang, X. Zhan,F. Wang,C. Jiang and J. He,Nano Lett. **16**, 6437 (2016).

[27] F. Wang , L. Yin , Z. X. Wang , K. Xu , F. M. Wang , T. K. A. Shifa,Y. Huang , C. Jiang and J. He, Adv.Functional Materials. **26**, 5499 (2016).

[28] F. Wang, Z. Wang, T. A. Shifa, Y. Wen, F. Wang,X. Zhan, Q. Wang, K. Xu, Y. Huang, L. Yin, C. Jiang and J. He, Adv. Functional Materials. **27**, 1603254 (2017).

[29] H. Fang, C. Battaglia, C. Carraro, S. Nemsak, B. Ozdol, J.S. Kang, H.A. Bechtel, S.B. Desai, F. Kronast, A. A. Unal and G. Conti, Proc. Natl. Acad. Sci. **111**, 6198 (2014).

[30] H.M. Hill, A.F. Rigosi, K.T. Rim, G.W. Flynn and T.F. Heinz, Nano Lett. **16**, 4831 (2016).

[31] D. Kozawa, A.Carvalho, I. Verzhbitskiy, F. Giustiniano, Y. Miyauchi, S. Mouri, A.H. Castro Neto, K. Matsuda and G. Eda, Nano Lett. **16**, 4087 (2016).

[32] M.Z. Bellus, M. Li, S.D. Lane, F. Ceballos, Q. Cui, X.C. Zeng and H. Zhao, Nanoscale Horizons, **2**, 31 (2017).

[33] Z. Huang, C. He, X. Qi, H. Yang, W. Liu, X. Wei, X. Peng and J. Zhong, J. Phys. D: Appl. Phys. **47**, 075301 (2014).

[34] H.P. Komsa and A.V. Krasheninnikov, Phys. Rev. B **88**, 085318 (2013).

[35] R. Gillen, J. Robertson and J. Maultzsch, Phys. Rev. B **90**, 075437 (2014).

[36] X. Cui, G.H. Lee, Y.D. Kim, G. Arefe, P.Y. Huang, C.H. Lee, D.A. Chenet, X. Zhang, L. Wang, F. Ye and F. Pizzocchero, Nat. Nanotechnol. **10**, 534 (2015).

[37] S. Wang, X. Wang and J.H. Warner, ACS Nano **9**, 5246 (2015).

[38] Z. Zhang, X. Ji, J. Shi, X. Zhou, S. Zhang, Y. Hou, Y. Qi, Q. Fang, Q. Ji, Y. Zhang and M. Hong, ACS Nano **11**, 4328 (2017).

[39] X. Ling, Y.H. Lee, Y. Lin, W. Fang, L. Yu, M.S. Dresselhaus and J. Kong, Nano Lett.**14**, 464 (2014).

[40] B. Loukya, P. Sowjanya, K. Dileep, R. Shipra, S. Kanuri, L.S. Panchakarla and R. Datta, J. Crys. Growth **329**, 20 (2011).

[41] R. Sahu, D. Radhakrishnan, B. Vishal, D. S. Negi, A. Sil, C. Narayana and R. Datta, J. Crys. Growth **470**, 51 (2017).

[42] X. Hong, J. Kim, S. F. Shi, Y. Zhang, C. Jin, Y. S. S. Tongay, J.Wu, Y. Zhang and F. Wang, Nat. Nanotechnol. **9**, 682 (2014).

[43] U. Bhat, R. Singh, B Vishal, A. Sharma, S. Horta,R. Sahu and R. Datta., physica status solidi (b) **255** (7), 1700691 (2018).

[44] K. Dileep, R. Sahu, S. Sarkar, S.C. Peter and R. Datta, J. Appl. Phys. **119**, 114309 (2016).

[45] N. Dubrovinskaia, V. L. Solozhenko, N. Miyajima, V. Dmitriev, O. O. Kurakevych and L. Dubrovinsky, Appl. Phys. Lett. **90**, 101912 (2007).

[46] B. Vishal, R. Singh, A. Chaturvedi, A. Sharma,M.B. Sreedhara, R. Sahu, U. Bhat, U. Ramamurty and R. Datta, Superlattices and Microstructures **115**, 197 (2018).

[47] A. Bartl, S. Bohr, R. Haubner and B. Lux, Int. J. Refractory Metals and Hard Materials**14**, 145 (1996).

[48] E. Knittle, R. B. Kaner, R. Jeanloz and M. L. Cohen, Phys. Rev. B **51**, 12149 (1995).

[49] H. Terrones, F. L. Urias and M. Terrones, Scientific Report **3,** 1549 (2013).

[50] Y. Ding, Y. Wang, J. Ni, L. Shi, S. Shi and W. Tang, Physica B, **406**, 2254 (2011).

[51] Z. Y. Zhu, Y. C. Cheng and U. Schwingenschlogl, Phys. Rev. B **84**, 153402 (2011).

[52] K. Watanabe, T. Taniguchiand H. Kanda, Nat. materials **3**, 404 (2004).

[53] G. Cassabois, P. Valvin and B. Gil, Nat. Photonics **10**, 262 (2016).

[54] H. Heo, J. H. Sung, S. Cha, B. G. Jang, J. Y. Kim, G. Jin, D. Lee, J. H. Ahn, M. J. Lee, J. H. Shim, H. Choi and M. H. Jo, Nat. Comm. **6**, 7372 (2015).

[55] G. Plechinger, F. X. Schrettenbrunner, J. Eroms, D. Weiss, C. Schüller, and T. Korn, Phys. Status Solidi RRL **6**, 126 (2012).

[56] P. K. Chow, R. B. J. Gedrim, J. Gao, T. M. Lu, B. Yu, H. Terrones and N. Koratkar, ACS Nano 9, 1520 (2015).

[57] H. Nan, Z. Wang, W. Wang, Z. Liang, Y. Lu, Q. Chen, D. He, P. Tan, F. Miao, X. Wang, J. Wang and Z. Ni, ACS Nano **8**, 5738 (2014).

[58] S. Horzum,D. C¸ akır,J. Suh,S. Tongay,Y.S. Huang,C.H. Ho,J. Wu, H. Sahinand F. M. Peeters, Phys. Rev. B **89**, 155433 (2014).

[59] J.V. D. Vehadis, J. B. Khurgin, Y.J. Ding, A. G. Cui and D. S. Katzer, Phys. Rev. B **50**, 4463 (1994).

[60] S. Haastrup, S. Latini, K. Bolotin and K. S. Thygesen, arXiv:1602.04044v1 (2016).

[61] M. Kang, B. Kim, S. H. Ryu, S. W. Jung, J. Kim, L. Moreschini, C. Jozwiak, E. Rotenberg, A. Bostwick and K. S. Kim, Nano Lett. **17**, 1610 (2017).

Chapter 4

Chemically stabilized epitaxial *wurtzite*-BN thin film

This chapter emphasizes the growth of the chemically stabilized epitaxial w-BN thin film on c-plane sapphire by pulsed laser deposition under slow kinetic condition. Traces of no other allotropes such as cubic (c) or hexagonal (h) BN phases are present. Sapphire substrate plays a significant role in stabilizing the metastable w-BN from h-BN target under unusual PLD growth condition involving low temperature and pressure and is explained based on density functional theory calculation. The hardness and the elastic modulus of the w-BN film are 37 & 339 GPa, respectively measured by indentation along <0001> direction. The results are extremely promising in advancing the microelectronic and mechanical tooling industry.

This work has been published in the following journal:

***B. Vishal,** R. Singh, A. Chaturvedi, A. Sharma, M.B. Sreedharaa, R. Sahu, U. Bhat, U. Ramamurty, and R. Datta, Superlattices and Microstructures, **115**, 197-203 (2018).*

4.1 Introduction

Boron Nitride (BN) exhibits numerous allotropes e.g., hexagonal (*h*-BN, $P6_3/mmc$), rhombohedral (*r*-BN, R3m), cubic (*c*-BN, Fd3m) and *wurtzite* (*w*-BN, $P6_3mc$) which are analogous to Carbon (C) allotropes. Among these, *h*-BN is the most stable form found at room temperature and pressure. *c*-BN and metastable *w*-BN can be stabilized, but require extreme temperature (1730-3230 °C) and pressure (5-18 GPa) condition [1]. The equilibrium phase diagram of BN depicts that the stabilization of *w*-BN requires either *c*-BN or *h*-BN as the starting phase and may be difficult to synthesize in the pure form [2]. Observation of synthetic *w*-BN, converted from *h*-BN at a pressure of 11.5 GPa and temperature of 2000K, was first reported in 1963 by Bundy and Wentorf Jr.[3]. Subsequently, various methods e.g., static high-pressure, shock-wave compression method, direct conversion from *h*-BN have been reported [4-8]. P- T phase and reaction diagram for BN, where *w*-BN is metastable phase and found at extreme P-T condition shown in Figure 4.01.(a) [8].

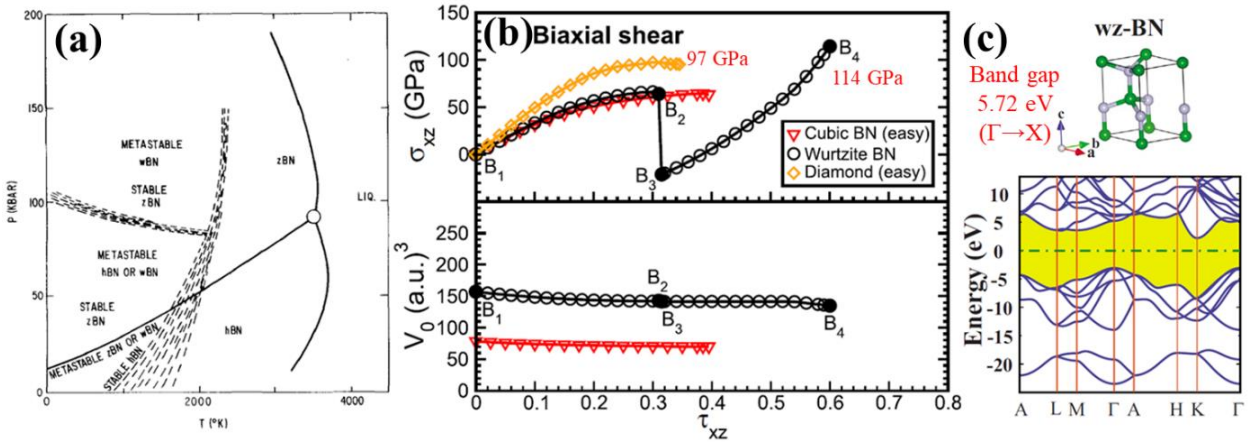

Figure 4.01. *(a) P- T phase and reaction diagram for BN.where w-BN is metastable phase and found at extreme P-T condition (T = 1730-3230°C and P = 5-18 GPa). Copyright (1975) by American Institute of Physics [8]. (b) Theoretical calculation by Z. Pan et. al. shows the w-BN is second hardest material. Copyright (2009) by The American Physical Society [21]. (c) w-BN is ultra-high band gap semiconductor with indirect band gap of 5.72 eV (Γ→X), which is good for deep UV range optoelectronic application. Copyright (2009) by The American Physical Society [26].*

Experimental investigation into the properties of *w*-BN is scarce because of the difficulty in synthesizing sufficiently large and pure crystals of it. Recently, synthesis of 2 mm diameter and 350 µm thick *w*-BN crystals with 98% purity (*h*-BN is the residue phase) under direct conversion method involving high temperature (1500 °C) and pressure (4 GPa) was reported [7]. There are reports on the formation of *w*-BN and *c*-BN by thin film growth procedure [9-13]. Polycrystalline (2-20 µm grain size) *w*-BN film is deposited on amorphous C film by pulsed laser deposition [11]. Only *c*-BN thin film is deposited on Si (100) substrate by ion-assisted pulsed laser deposition at 400 °C and 10^{-5} Torr [12] Mixture of *c*-BN and *w*-BN has also been reported by PLD on WS_2 and ReS_2 template [14].

Two-dimensional (2D) layered *h*-BN (also called white graphene) has recently attracted considerable attention to improving the performance of graphene, other 2D materials such as MoS_2 and also being explored as an active material for the optoelectronic and energy applications [15-18]. On the other hand, *c*-BN and *w*-BN are attractive due to high hardness and the potential in electronic applications remains unexplored [14,19]. In *w*-BN structure, each atom is tetrahedrally coordinated with a B-N bond length of 157 pm and a bond angle of 109.5° with '*..aa'bb'aa'..*' stacking of the basal plane along *c* direction and the structure is denser and harder compared to *h*-BN [20]. Theoretical predictions indicate that both *c*-BN and *w*-BN are super hard, with *w*-BN being the second most hard material (114 GPa) after Lonsdaleite (hexagonal C, hardness - 152 GPa), due to an intermediate bond flipping structural phase transition shown in Figure 4.01.(b). [21]. Recently, another new form of C called Q-carbon has been predicted to show higher hardness than diamond [22]. However, the unavailability of a sufficiently large crystal of *w*-BN and Lonsdaleite prevented experimental verification of these predictions [21,23,24]. Therefore, diamond retained the top position in the list. Both *w*-BN and *c*-BN have the advantage over the diamond in terms of excellent chemical and thermal stability (oxidation temperature is 1300 °C compared to 700 °C of diamond) suitable for high-speed manufacturing. Experimentally, the nanocrystalline (~14 nm) composite of *c*-BN and *h*-BN exhibited hardness of 85 GPa which is close to that of diamond [25]. The millimeter size bulk *w*-BN crystal (98% purity) showed Hardness and Young's modulus values of ~ 54 and 860 GPa, respectively [7]. *w*-BN is ultra-high band gap semiconductor with indirect band gap of 5.72 eV ($\Gamma \rightarrow X$), which is good for deep UV range optoelectronic application [Figure 4.01.(c)] [26].

Here, we report on the formation of large area single phase epitaxial thin film of *w*-BN at much lower temperature and pressure compared to the extreme condition usually require for stabilizing this metastable phase [2]. The film is grown by pulsed laser deposition (PLD) under slow kinetic condition. The formation of *w*-BN phase is confirmed by high-resolution transmission electron microscopy (HRTEM), X-ray diffraction (XRD) and Raman spectroscopy. The stabilization of metastable *w*-BN at low temperature (400 °C) and pressure (10^{-5} Torr) combination is rationalized based on chemical interaction between the O-planes of *c*-plane sapphire and the B atoms of the first *h*-BN layer, which is supported by first principle calculation. This chemical interaction initiates staggering in the first *h*-BN layer which subsequently transforms into *w*-BN [27]. Nanoindentation on the thin films shows that *H* and *E* of this phase are 37 and 339 GPa, respectively.

4.2 Experimental Methods

Thin films of w-BN are grown by pulsed laser deposition on 8×8 mm^2 size 'c' plane sapphire substrate. The target pellet is prepared from *h*-BN powder obtained from Sigma Aldrich (99.9%) by first cold pressing and then sintering at 800 °C for 5 h in a vacuum chamber (~10^{-5} Torr). The growth scheme epitaxial wurtzite-BN thin film shown in Figure 4.02. The ablation frequency used is 1 Hz during the film growth. The slow laser ablation rate allows sufficient time for kinetic relaxation of the nucleation layer to establish an epitaxial relationship with the underlying substrate. This also helps in eliminating misaligned crystallites for highly lattice mismatched epitaxy [28-30]. The pressure is kept constant at ~10^{-5} Torr throughout the growth schedule while the temperature of the growth was 400 and 800 °C for the nucleation and final growth, respectively. The formation of epitaxial *w*-BN thin film is confirmed by XRD, HRTEM, and electron diffraction techniques. TEM cross-sectional samples are prepared by first mechanical polishing and then Ar ion milling to perforation around which large electron transparent thin area is generated. Raman spectra are recorded using a custom-built Raman spectrometer using a 532 nm laser excitation and a grating of 1800 lines/mm at room temperature. The laser power at the sample is approximately 1 mW.

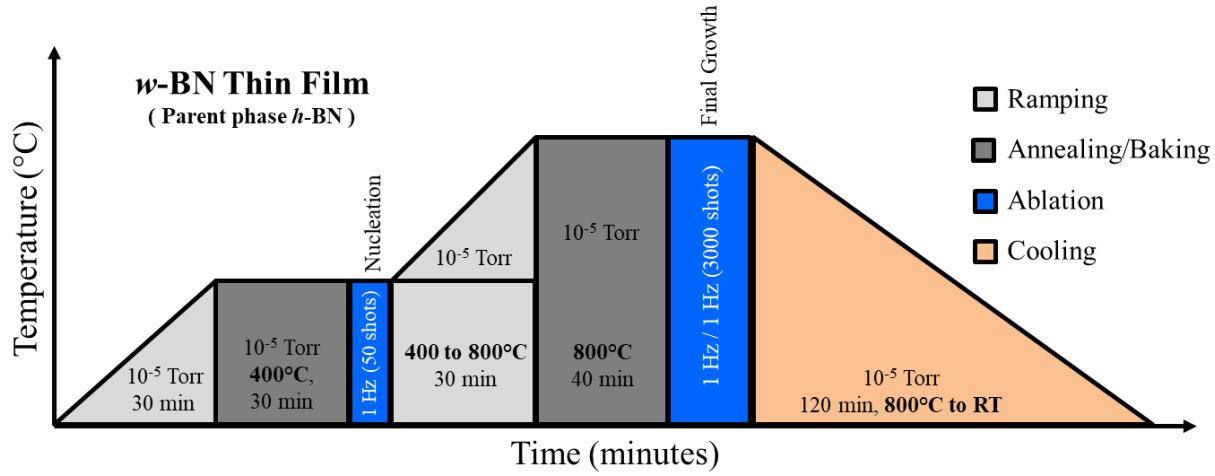

Figure 4.02. *The growth scheme of epitaxial wurtzite-BN thin film on* size '*c*' plane sapphire substrate *with slow kinetics of laser ablation (1Hz).*

To measure the mechanical properties of the thin film, nanoindentation is performed on 100 nm thick BN film on sapphire substrate using Hysitron Triboindenter, Minneapolis, MN, USA, equipped with a three-sided pyramidal Berkovich diamond indenter with a tip radius of ~100 nm. The equipment records the load, P, and depth of penetration, h, of the indenter with resolutions of 1 nN and 0.2 nm, respectively. The tests are performed both under displacement and load controlled modes to examine the reproducibility of the results since the maximum depths of penetrations, h_{max}, are small. Around 20 indentations are performed on each sample. The recorded P-h responses are analyzed using the standard Oliver-Pharr method to extract the reduced elastic modulus, E_r, and hardness, H, of the sample [31].

4.3 Computational Techniques

To understand the substrate effect on the phase transition from *h*-BN to *w*-BN theoretical calculations are performed based on density functional theory (DFT) using self-consistent plane wave pseudopotential as implemented in Quantum Espresso (QE) code [32]. The ionic core-valence electron interactions are modeled using ultra-soft pseudo-potentials [33]. Electronic exchange-correlation energy is approximated using Perdew-Burke-Ernzerhof (PBE) functional within generalized gradient approximation (GGA) [34]. The following cases were simulated, (*i*) monolayer *h*-BN (*ii*) Modulated monolayer BN, (*iii*) bilayer *h*-BN and (*iv*) modulated bilayer BN

on top of O-end Al_2O_3 with epitaxial relation *w*-BN $< 11\bar{2}0 >$ ∥ Al_2O_3 $< 01\bar{1}0 >$ that were observed experimentally. The schematic of the simulated structure is later shown in Figure 4.09. and [Figure 4.10]. Kinetic energy and augmented charge density cutoffs used are 50 and 400 Ry, respectively. Atomic positions and cell parameters are fully relaxed below energy convergence of 10^{-5} eV. Optimized structures of BN and Al_2O_3 are stacked according to epitaxial relation and then VC (variable cell)-relaxation is carried out with 8×8×8 k-mesh according to the scheme proposed by Monkhorst and Pack [35]. Relaxed supercell parameters of the *h*-BN on Al_2O_3 substrate is $a = b = 4.840$ Å and $\alpha = \beta = 90°$, $\gamma = 120°$ and additional 20 Å of vacuum is created along *c*-direction on top of BN.

4.4 Results and Discussion

4.4.1 Epitaxial relation of *w*-BN and Al_2O_3

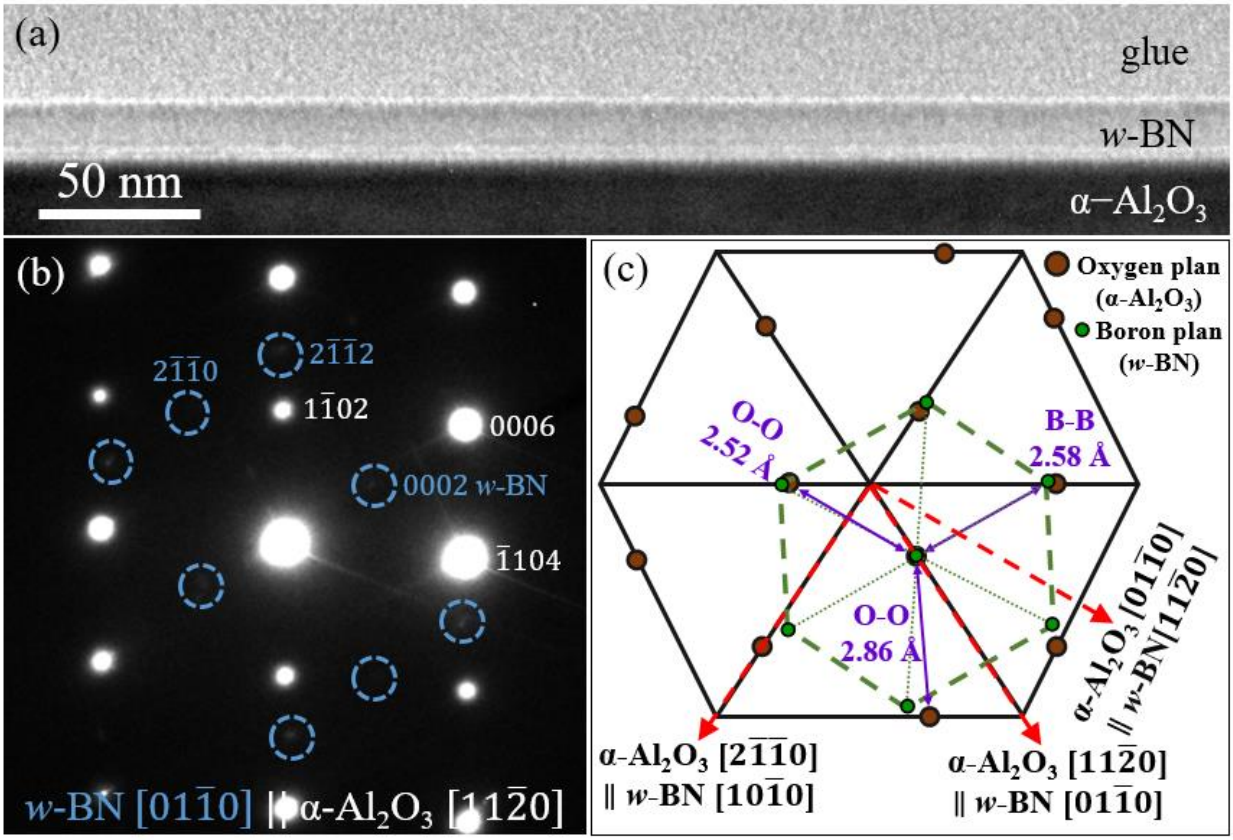

Figure 4.03. *(a) TEM bright field image of w-BN thin film on c-plane sapphire substrate along* $< 01\bar{1}0 >$ *Z.A. of w-BN. (b) Electron diffraction pattern showing epitaxial relationship between*

sapphire and w-BN is α-Al_2O_3 $< 11\bar{2}0 >\|$ w-BN $< 01\bar{1}0 >$. (c) Schematic showing in-plane epitaxial relationship between w-BN and sapphire substrate. Copyright (2018) by Elsevier [27].

We begin with the description of structural characterization confirming the formation of epitaxial *w*-BN thin film on (0001) plane of sapphire. From the low magnification TEM image uniform and smooth film of *w*-BN with thickness ~ 20 nm can be observed [Figure 4.03(a)]. The film can be grown as thick as required following the slow kinetic condition. Indentation experiment was carried out on a film of 100 nm thickness. Figure 4.03.(b) & (c) are the electron diffraction (ED) pattern and schematic of in-plane orientation relationship between *w*-BN and sapphire, respectively. The epitaxial relationship is found to be *w*-BN $[01\bar{1}0] \parallel$ *α*-Al_2O_3 $[11\bar{2}0]$ and the relative rotation of *c* axis between film and substrate is 30°, which is similar to the growth of GaN or ZnO on *c*-plane sapphire. The chemical interaction between B and O atoms is responsible for such an arrangement and is explained later with the aid of DFT.

4.4.2 Raman, XRD, XPS of *wurtzite*-BN epitaxial thin film

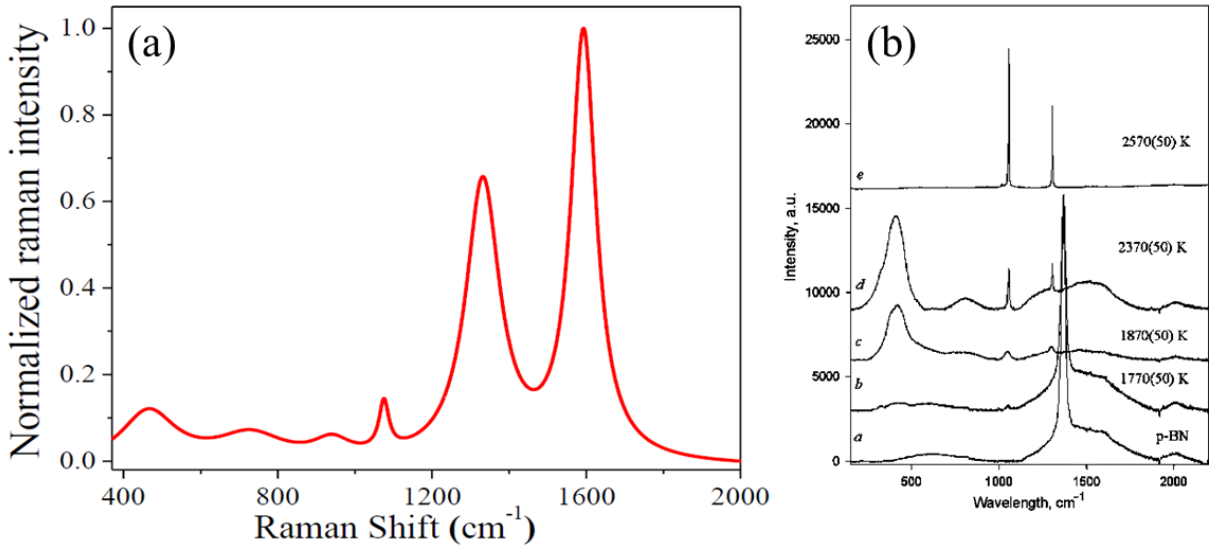

Figure 4.04. (a). *Raman spectra from w-BN epitaxial thin film. Copyright (2018) by Elsevier [27]. (b) Experimental reference Raman spectra for different crystal form of BN [25]. Copyright (2018) by Elsevier [25].*

The Raman spectra of the *w*-BN thin film is given in Figure 4.04.(a) The Raman spectra of reference powder *h*-BN, *c*-BN and *w*-BN are provided in Figure 4.05.(b) [25]. The peak, observed around 1370 cm^{-1} corresponds to the *h*-BN structure. For *c*-BN, two distinct sharp peaks 1057 and 1309 cm^{-1} were noted, whereas many broad peaks are present in case of *w*-BN. The FWHM of the Raman peaks corresponding to *w*-BN is relatively narrower in the present study, as compared to those reported earlier, which is due to large crystalline area in the former. During the study, it is also found that BN grows with different polytypic phases on TMDs depending on the TMD template (MoS_2, WS_2, and ReS_2) [14]. XRD and XPS spectra supporting the formation of *w*-BN can be found in Figure 4.05.

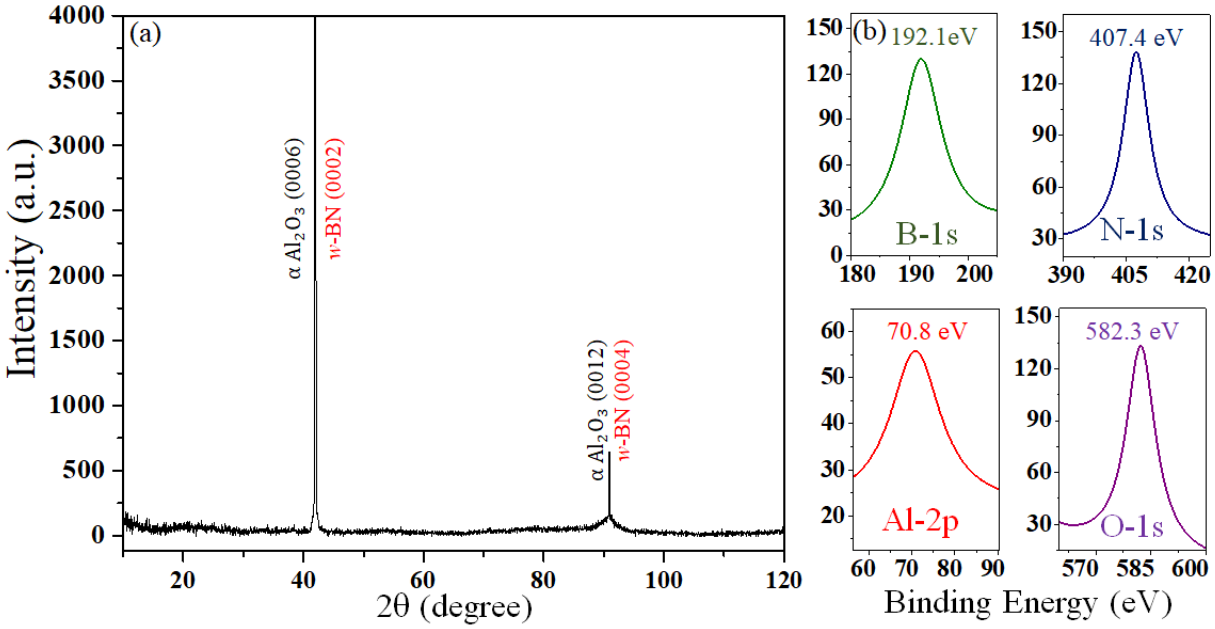

Figure 4.05. *(a) X-ray diffraction pattern of epitaxial w-BN on c-plane sapphire. Kindly note that the (0002) peak of w-BN (2θ = 41.94°) superimposes with (0006) of sapphire (2θ = 41.83°). No other peaks corresponding to h-BN, c-BN, and polycrystalline grains are observed. (b) XPS spectra of B 1s, N 1s, Al 2p and O 1s identifying the elements present both in the film and substrate. Copyright (2018) by Elsevier [27].*

4.4.3 Detailed Microstructural by TEM

HRTEM images of *w*-BN thin film on *c*-plane sapphire (Al_2O_3) along two different zone axes (Z.A.) orientations are given in Figure 4.06 and Figure 4.07. The film is relaxed and the lattice parameters of *w*-BN are approximately a = 2.58 Å and c = 4.29 Å. The atomic registry of the film with the terminating O-plane of *c*-plane sapphire substrate and specific stacking of atomic planes '…*ababa*..' can clearly be observed and schematics are provided for guidance.

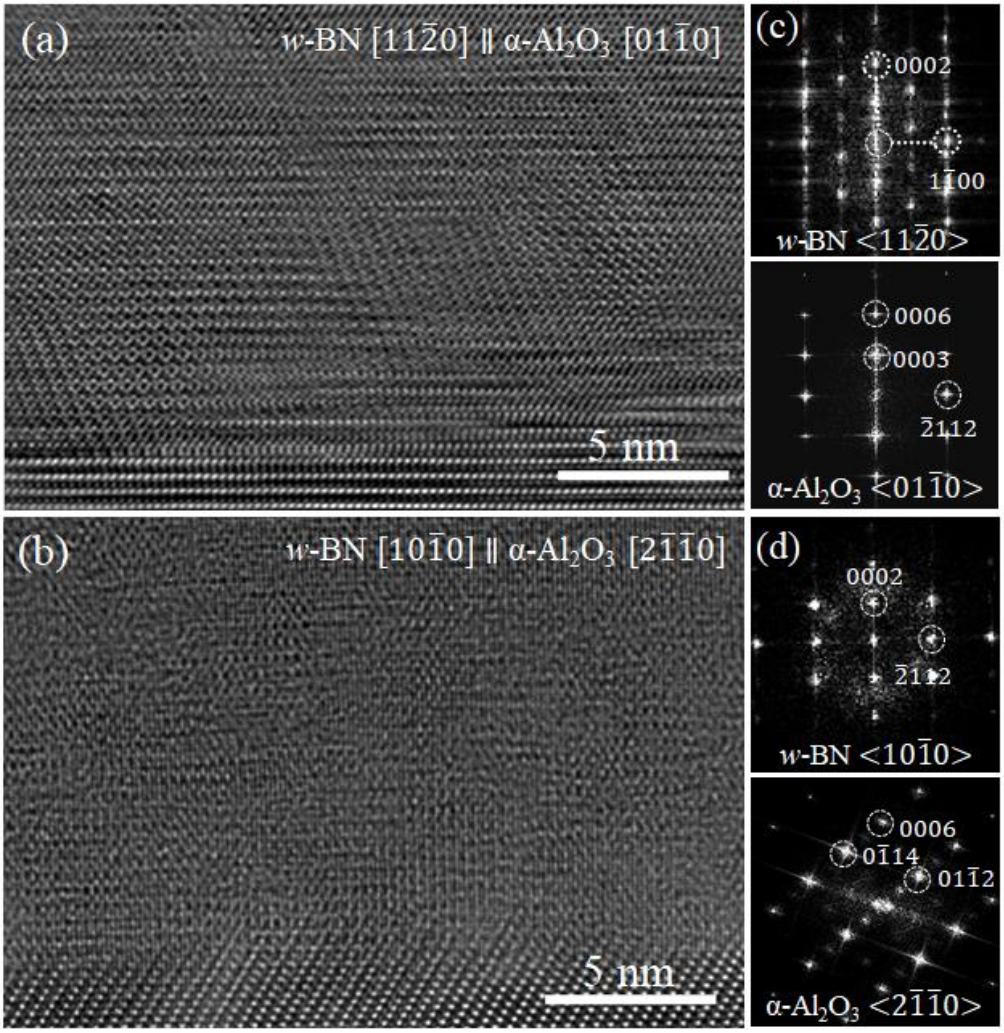

Figure 4.06. *HRTEM image of w-BN on c-plane sapphire along (a) <01$\bar{1}$0>, (b) <2$\bar{1}\bar{1}$0> of sapphire. Corresponding FFT pattern both from the film and substrate areas are given in the (c) and (d), respectively. Copyright (2018) by Elsevier [27].*

In addition to the ED pattern, the specific stacking of atomic planes along the growth direction in the film also confirming the formation of *w*-BN phase.

Presence of *h*-BN or any other allotropes is not detected and *w*-BN is the only phase formed right from the film-substrate interface with some planar faults present in the film. This suggests that the phase transformation from *h*-BN to *w*-BN must have occurred at the O-terminated (0001) plane of sapphire via chemical interaction which is further supported by DFT based calculation. The difference in electronegativity between B and O is high compared to N and O atoms. Therefore, the chemical bonding between BN to sapphire is due to bonding between B and O atoms which is energetically more favorable compared to N and O bonding by 173 meV/atom. This is indicated with the color round circles in Figure 4.07.

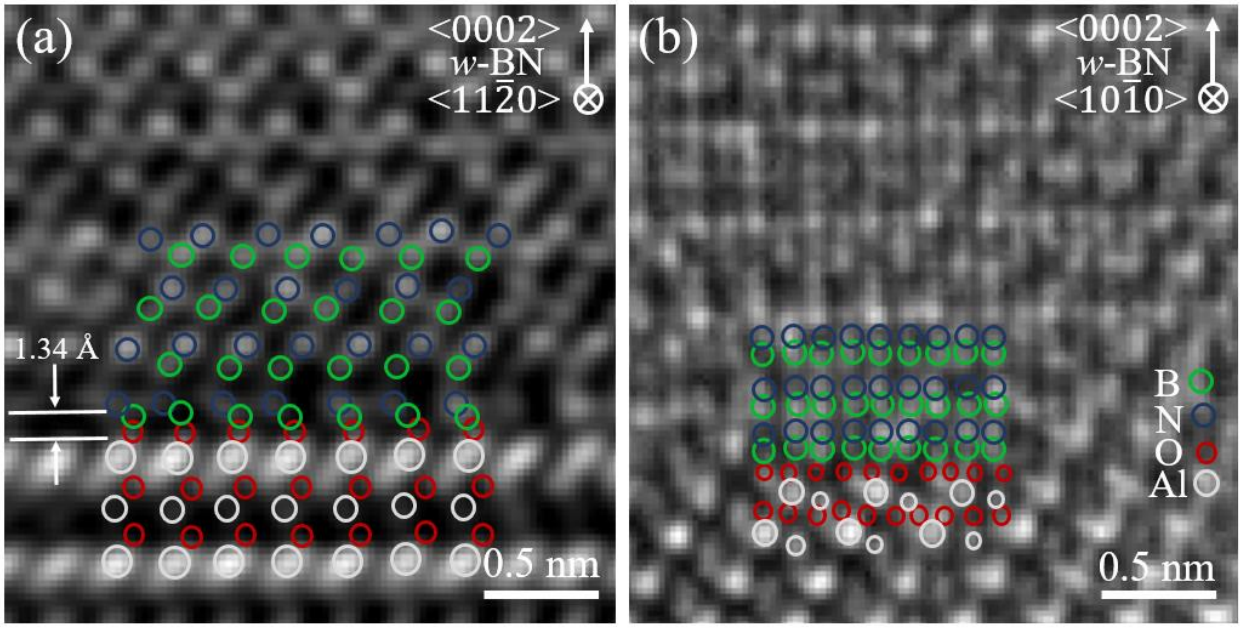

Figure 4.07. *(a) & (b) HRTEM image of w-BN on c-plane sapphire along two different zone axes of sapphire showing atomic arrangement and registry of atoms at the film substrate interface. The inter-atomic distances are mentioned in the Figure. Copyright (2018) by Elsevier [27].*

From the HRTEM image, the interatomic distance between B and O atoms along the projected *c* direction is ~1.34 Å. The shortest inter-atomic distances along *c* direction for *w*-BN and *h*-BN are ~1.4 and 2.6 Å, respectively. This suggests that the bonding between the first BN

layer to O-plane of sapphire is due to covalent chemical bonding and not weak van der Waals interaction. Moreover, the structure of *h*-BN can be converted to *w*-BN by staggering the layer by selective bonding between B and O atoms [as shown in Figure 4.10 (a)]. HRTEM image also shows that the first layer is like staggered *h*-BN [Figure 4.07]. As already mentioned, *h*-BN is used as starting compound during the film growth. Theoretically similar structural transformation through staggering the *h*-BN to *w*-BN was considered under pure shear stress and not by chemical interaction [23].

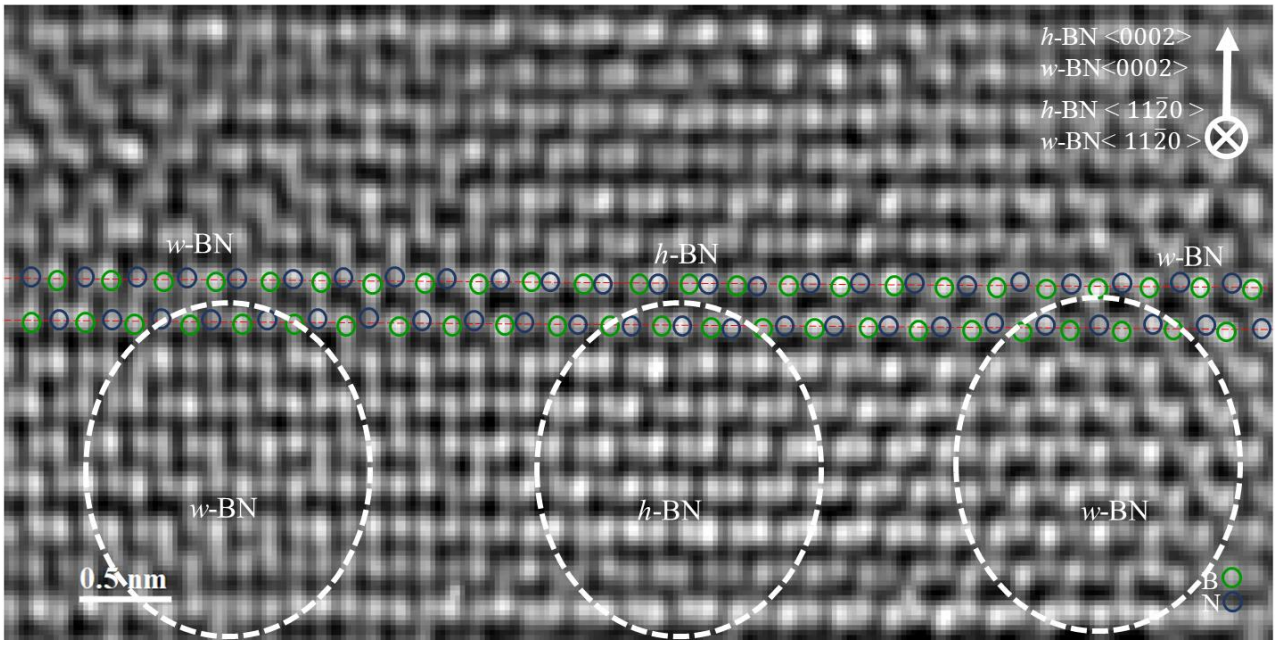

Figure 4.08. *HRTEM image show the phase transformation from h-BN and w-BN. It is experimental proof of the in-plane staggering (along red line) of boron and nitrogen in parent h-BN will transform into w-BN. Phase relationship is h-BN* <0002> ‖ *w-BN*<0002> *and h-BN* < 11$\bar{2}$0 > ‖ *w-BN*< 11$\bar{2}$0 >.

4.4.4 Origin of chemical stability by DFT

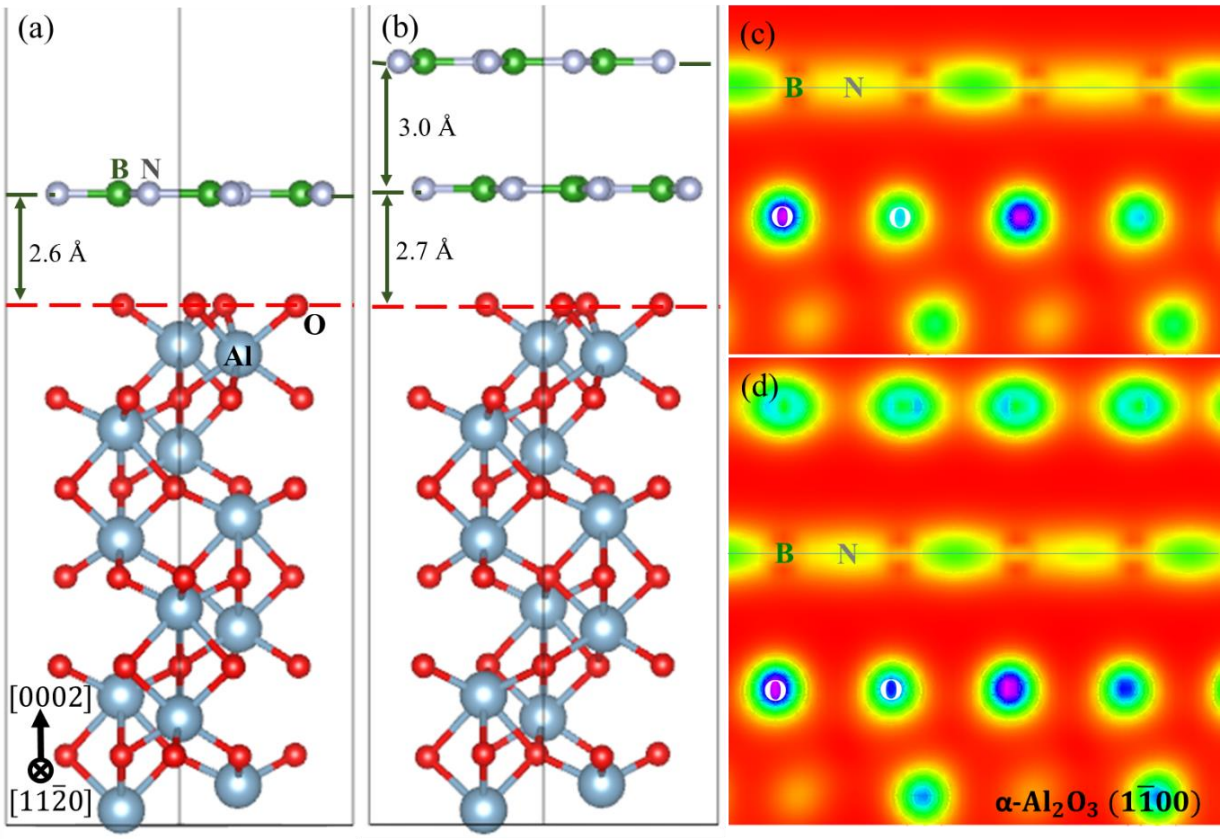

Figure 4.09. *Schematic structure of (a) monolayer and (b) bi-layer h-BN on c-plane sapphire. Charge density plot showing no additional interaction between B and O atoms at the interface between flat h-BN and O-terminating sapphire substrate. Copyright (2018) by Elsevier [27].*

DFT calculation was performed for both monolayer, bi-layer *h*-BN and staggered *h*-BN on O-terminated sapphire to get insights into the stability and chemical interaction through charge transfer between B and O atoms leading to structural phase transition from *h*-BN to *w*-BN. The structure of sapphire (α-Al_2O_3, space group $R\bar{3}c$) consists of 12 Al and 18 O atoms per unit cell with lattice parameter a = 4.758 Å, c = 12.992 Å. In O-ending (0001) plane of Al_2O_3, there are two distinct O-O-O equilateral triangles with O-O interatomic distances 2.52 and 2.86 Å where B-B-B triangle of staggered *h*-BN or the first layer of (0001) *w*-BN stack with a B-B interatomic distance 2.58 Å. This gives +2.3% and -9.7 % strain in the BN lattice corresponding to two

different O-O-O tringles and an overall -6.1 % lattice mismatch along *w*-BN $< 01\bar{1}0 >$ ‖ Al_2O_3 $< 2\bar{1}\bar{1}0 >$ resulting in non-uniform bond length [Figure 4.03.(c)].

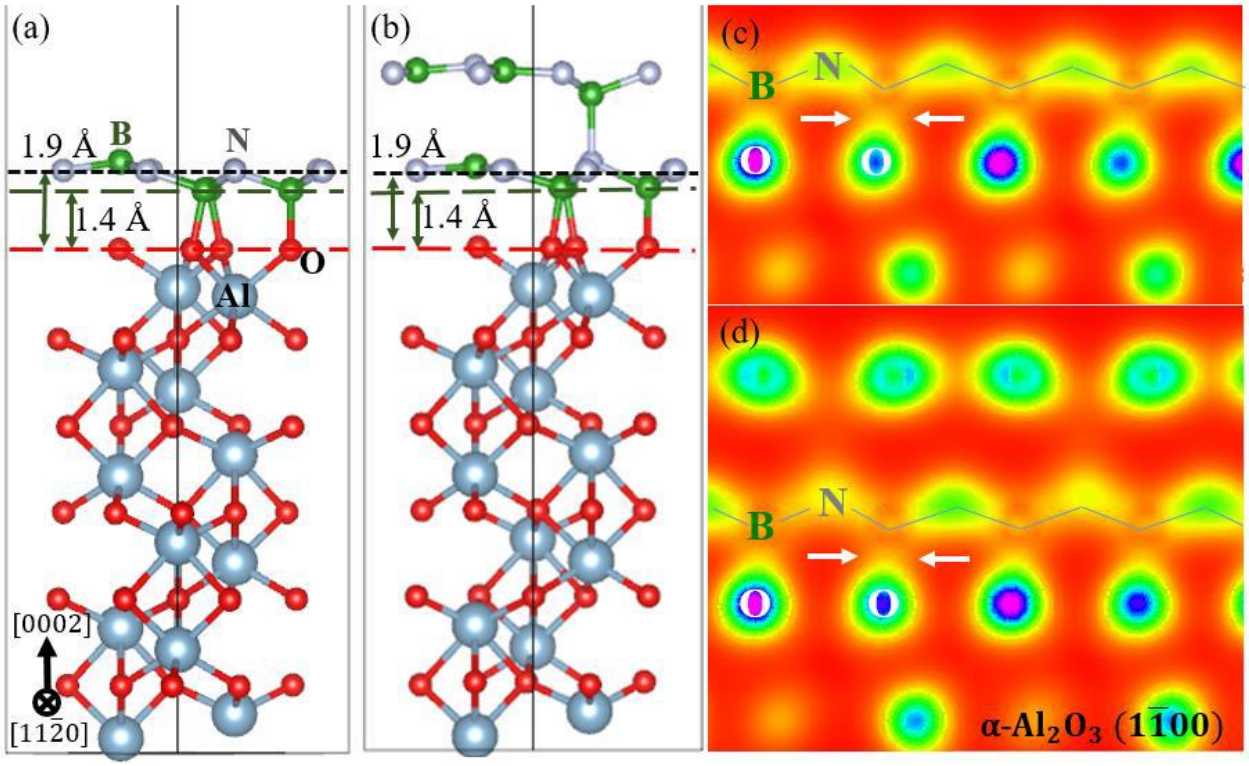

Figure 4.10. *Schematic structure of monolayer (a) staggered h-BN on c-plane sapphire. The stability of staggered h-BN configuration is 210 meV/atom more compared to flat h-BN. (b) staggered bi-layer h-BN showing nucleation and growth of w-BN phase along c direction. Charge density plot showing additional interaction between B and O atoms at the interface in both (c) mono and (d) bi-layer leading to staggering configuration of flat h-BN. Copyright (2018) by Elsevier [27].*

The calculation revealed that *w*-BN on sapphire with B-O bonding is more stable (7.76 eV/atom) than *h*-BN (7.55 eV/atom) for the monolayer coverage. Further calculation shows that the staggering propagates to the bi-layer as a stable system (7.92 eV/atom) compared to bi-layer flat *h*-BN (7.83 eV/atom) and eventually form the wurtzite structure [Figure 4.10.(b) and Figure 4.09 (b)]. The valence charge density plot reveals charge transfer between O and B atoms for staggered *h*-BN [Figure 4.10.(c) & (d)] but not for the flat *h*-BN [Figure 4.11.(c) & (d)]. The observation by HRTEM imaging at the interface and combination of first principle calculation

suggests that the selective and stronger chemical interaction between the O atoms and B atoms in *h*-BN for the first deposited layer initiated the structural phase transition from *h*-BN to *w*-BN and subsequently propagated along the (0001) direction.

4.4.5 *w*-BN hardness Measurement

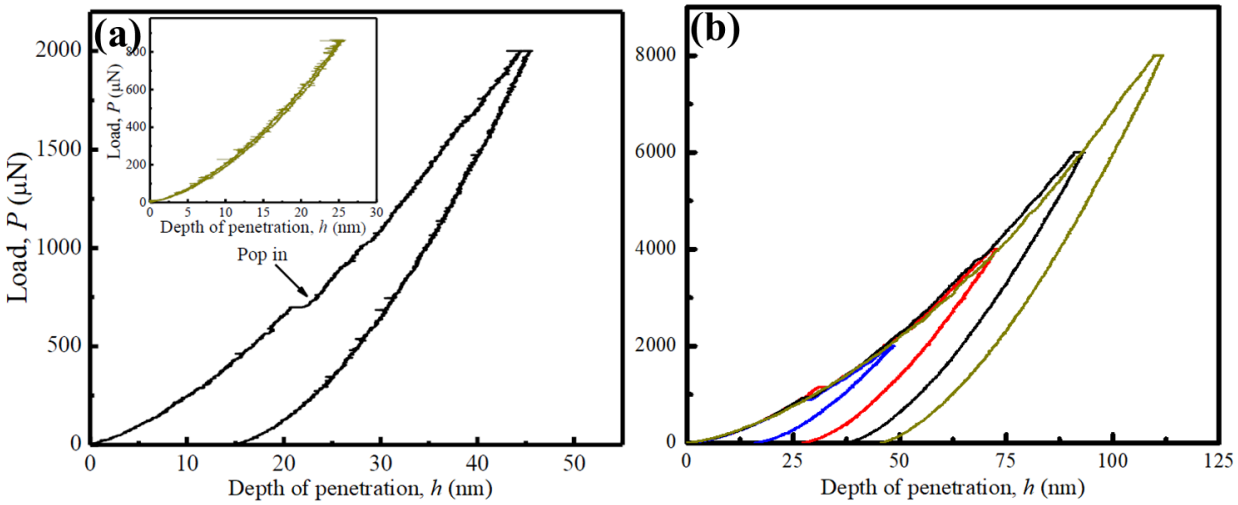

Figure 4.11. (a). *Load-displacement curves exhibiting pop in due to cracking or delamination phenomenon. (Inset graph shows shallow depth indent without pop-in).* ***(b).*** *Representative indents for α-Al_2O_3 for various penetration depths. Copyright (2018) by Elsevier [27].*

A representative *P-h* (load vs. penetration depth) response obtained through nano-indentation on the *w*-BN thin film is displayed in Figure 4.11.(a). A prominent discrete displacement jumps or 'pop-in' at $P \approx 600$ μN, which corresponds an *h* of ~20 nm can be seen. Such pop-ins can be either due to cracking or delamination of the film, both of which make the film compliant. Therefore, we confined subsequent experiments to extremely shallow depths (h_{max} = 15 nm). Representative *P-h* response obtained in those experiments is displayed as the inset of Figure 4. 11.(a). No pop-ins can be seen. The E and H values obtained from such experiments are 339 and 37 GPa, respectively. In addition to calibration before each set of nanoindentations, which are performed by fused quartz specimens, nano-indentation on bare α-Al_2O_3 was also performed. Results of these experiments [Figure 4.11.(b)] are in good agreement with those reported in literature [E = 444.4±20.1 GPa and H = 28.9±2.3 GPa along (0001)] [36]. Importantly, the E values obtained via shallow depth nano-indentations (h_{max} = 40 nm), are similar to those obtained with

much higher h_{max}. This observation confirmed the validity of extracting E and H values from shallow depth indentations.

The experimental values of hardness (37 GPa) and elastic modulus (339 GPa) of the present *w*-BN thin film is in the lower side among various experimental measurement of this phase either in bulk or nano-composite form reported earlier [Table 1]. The present measurement of epitaxial *w*-BN thin film involves indentation along <0001> direction due to the orientation of film and such measurement is highly anisotropic compared to the earlier reports. Note that the <0001> direction is not the closed packed direction of *w*-BN structure and hence unlikely to exhibit the highest stiffness or hardness [21]. Theoretically, the tensile strength of *w*-BN is 68/90 GPa along <0001> and $< 11\bar{2}0 >$ directions, respectively [21,24].

Table I. List of reported hardness (H) and modulus (E) values of known hard materials obtain from experiment (Exp.) or calculations (Calc.). Experimental measurement methods i.e. Vickers (V), Knoop (K) is indicated. *Copyright (2018) by Elsevier [27]*.

Phase	Phase	H (GPa)	E (GPa)	Exp. Or calc.
w-BN	Thin Film	37 (V)	339	Exp.(present work)
w-BN	Bulk	54 (V) [7]	860[7]	Exp.
Diamond-C	Bulk	96(V) [22,40]	535 [40]	Exp.
Natural Diamond	Bulk	57-104 (K) [39]	1140 [39]	Exp.
Diamond	Nanocrystallite	105 (K) [39], 120-145 (K) [42]	1070 [39]	Exp.
Lonsdelite		152 [21]		Calc.
c-BN	Bulk	64 (V) [37]		Calc.
c- BN	Nanotwins in bulk	108-196 (V) [41]		Exp.

The bi-axial shear strength with intermediate structural transition can reach 114 GPa. If we extrapolate the experimental data based on the theory calculation then the film would show the strength of ~ 65 GPa along ($< 11\bar{2}0 >$) direction, which is still lower than predicted. Possible reasons for the experimental values being less than the theoretical predictions are that (a) the structure may not have undergone bond flipping intermediate structural transitions proposed earlier, and (b) the presence of planar defects in the as-grown film whereas theoretical predictions are made on perfect crystals and hence are ideal values.

4.5 Conclusion

In conclusion, *w*-BN thin film is grown under relatively low pressure and temperature condition in PLD compared to the extreme higher temperature and pressure condition usually required to stabilize this metastable phase. The phase transition occurred due to chemical interaction between B and O atoms leading to staggering in flat *h*-BN layer transforming to *w*-BN structure. The hardness of the film is 37 GPa lower than theoretical prediction due to indention along soft direction, thin film geometry and defects present in the film. Nonetheless, the growth of such epitaxial thin film may find application in tooling and microelectronic industry.

4.6 Bibliography

[1] R. H. Wentorf Jr, J. Chem. Phys. **34**, 809-812 (1961).

[2] V. L. Solozhenko, D. Häusermann, M. Mezouar, M. Kunz, Appl. Phys. Lett. **72**, 1691-1693 (1998).

[3] F. P. Bundy, R. H. Wentorf Jr, J. Chem. Phys. **38**, 1144-1149 (1963).

[4] E. Tani, T. Sōma, A. Sawaoka, S. Saito, Jpn. J. Appl. Phys. **14**, 1605 (1975).

[5] T. Sōma, A. Sawaoka, S. Saito, Mat. Res. Bull. **9**, 755-762 (1974).

[6] T. Akashi, H. R. Pak, A. B. Sawaoka, J. Mater. Sci. **21**, 4060-4066 (1986).

[7] M. Deura, K. Kutsukake, Y. Ohno, I. Yonenaga,T. Taniguchi, Jpn. J. Appl. Phys. **56**, 030301 (2017).

[8] F. R. Corrigan, F. P. Bundy, J. Chem. Phys. **63**, 3812-3820 (1975).

[9] M. Sokołowski, J. Cryst. Growth 46, 136-138 (1979).

[10] J. Szmidt, A. Jakubowski, A. Michalski,A. Rusek, Thin Solid Films **110**, 7-20 (1983).

[11] G. Kessler, H-D Bauer, W. Pompe, H-J Scheibe, Thin Solid Films **147**, L45-L50 (1987).

[12] D. L. Medlin, T. A. Friedmann, P. B. Mirkarimi, P. Rez, M. J. Mills, K. F. McCarty, J. Appl. Phys. **76** , 295 -303 (1994).

[13] T. K. Paul, P. Bhattacharya, D. N. Bose, Appl. Phys. Lett. **56,** 2648-2650 (1990).

[14] U. Bhat, R. Singh, B Vishal, A. Sharma, S. Horta,R. Sahu and R. Datta., status solidi (b) **255** (7), 1700691 (2018).

[15] G. Giovannetti, P. A. Khomyakov, G. Brocks, P. J. Kelly, Van Den Brink, Phys. Rev. B **76,** 073103 (2007).

[16] G. Cassabois, P. Valvin, B. Gil, Nat. Photonics **10,** 262–266 (2016).

[17] T. Q. P. Vuong, S. Liu, A. Van der Lee, R. Cuscó, L. Artús, T. Michel, P. Valvin, J. H. Edgar, G. Cassabois, B. Gil, Nat. Mater. **17,** 152–158 (2018).

[18] M. R. Gao, Y. F. Xu, J. Jiang, S. H. Yu, Chem. Soc. Rev. **42,** 2986-3017 (2013).

[19] N. Izyumskaya, D. O. Demchenko, S. Das, Ü. Özgür, V. Avrutin, H. Morkoç, Adv. Electron. Mater. **3,** 1600485 (2017).

[20] R. R. Wills, Int. J. High Technology Ceramics **1,** 139-153 (1985).

[21] Z. Pan, H. Sun, Y. Zhang, C. Chen, Phys. Rev. Lett. **102,** 055503(2009).

[22] J. Narayan, A. Bhaumik, J. Appl. Phys. **118,** 215303(2015).

[23] W. J. Yu, W. M. Lau, Phys. Rev. B **67,** 014108(2003).

[24] R. F. Zhang, S. Veprek, A. S. Argon, Phys. Rev. B **77,** 172103(2008).

[25] N. Dubrovinskaia, V. L. Solozhenko, N. Miyajima, V. Dmitriev, O. O. Kurakevych, L. Dubrovinsky, Appl. Phys. Lett. **90,** 101912 (2007).

[26] M. Topsakal, E. Aktürk, S. Ciraci, Phys. Rev. B **79**, 115442 (2009).

[27] B. Vishal, R. Singh, A. Chaturvedi, A. Sharma, M.B. Sreedharaa, R. Sahu, U. Bhat, U. Ramamurty, and R. Datta, Superlattices and Microstructures, **115**, 197-203 (2018).

[28] B. Loukya, P. Sowjanya, K. Dileep, R. Shipra, S. Kanuri, L. S. Panchakarla, R. Datta, J. Cryst. Growth **329,** 20-26 (2011).

[29] R. Sahu, D. Radhakrishnan, B. Vishal, D. S. Negi, A. Sil, C. Narayana, R. Datta, J. Cryst. Growth **470,** 51-57 (2017).

[30] R. Sahu, H. Gholap, G. Mounika, K. Dileep, B. Vishal, S. Ghara, R. Datta, Phys. Stat. Sol. (b) **253,** 504-508 (2016).

[31] W. C. Oliver, G. M. Pharr, J. Mater. Res. **7,** 1564-1583 (1992).

[32] P. Giannozzi, S. Baroni, N. Bonini, M. Calandra, R. Car, C. Cavazzoni, D. Ceresoli, G. L. Chiarotti, M. Cococcioni, I. Dabo, J. Phys.: Condens. Matter **21,** 395502(2009).

[33] D. Vanderbilt, Phys. Rev. B **41,** 7892 (1990).

[34] J. P. Perdew, K. Burke, M. Ernzerhof, Phys. Rev. Lett. **77,** 3865(1996).

[35] H. J. Monkhorst, J. D. Pack, Phys. Rev. B **13,** 5188 (1976).

[36] S. Ruppi, A. Larsson, A. Flink, Thin Solid Films **516,** 5959-5966 (2008).

[37] F. Gao, J. He, E. Wu, S. Liu, D. Yu, D. Li, S. Zhang, Y. Tian, Phys. Rev. Lett. **91,** 015502 (2003).

[38] A. Šimůnek, J. Vackář, Phys. Rev. Lett. **96,** 085501 (2006).

[39] N. Dubrovinskaia, S. Dub, L. Dubrovinsky, Nano Lett. **6,** 824-826 (2006).

[40] R. A. Andrievski, Int. J. Refrat. Met. Hard Matt. **19,** 447-452 (2001).

[41] Y. Tian, B. Xu, D. Yu, Y. Ma, Y. Wang, Y. Jiang, W. H. C. Tang, Y. Gao, K. Luo, Z. Zhao, L.-M. Wang, B. Wen, J. He, Z. Liu, Nature **493,** 385-388 (2013).

[42] H. Sumiyaa, T. Irifuneb, Diam. Relat. Mater. **13,** 1771-1776 (2004).

Chapter 5

Investigation of microstructural details in low thermal conducting thermoelectric $Sn_{1-x}Sb_xTe$

This chapter discusses the detailed microstructural features in low thermal conducting $Sn_{1-x}Sb_xTe$ (x = 0.04, 0.08, 0.15) alloy investigated by transmission electron microscopy and density functional theory calculation. Thermal conductivity is obtained for $Sn_{0.85}Sb_{0.15}Te$ alloy composition containing distinct microstructures at their minimum energy configuration. The crisscross lines along {111} planes forming nano-scale structures have been identified as areas with Sb replacing both regular Sn sites and Te anti-sites. This leads to the modulation in {111} inter-planar spacing (d_{111}) and results in superstructure spots in the electron diffraction pattern. The formation of such structures is supported by theoretical calculation. Two different phases are observed in the system, one with Sb replacing the regular Sn sites and the areas with crisscross lines where Sb is replacing both the Sn and Te sites. Calculation further reveals that the areas with Sb at the regular site gives large thermo-power, whereas the regions with Sb substituting regular and anti-sites combination forming superstructure are contributing towards low lattice thermal conductivity and the combined effect increases the zT to ~1.

This work has been published in the following journal:

***B. Vishal**, R. Sahu, U. Bhat and R. Datta, Journal of Applied Physics, **122 (5)**, 055102 (2017).*

5.1 Introduction

Harvesting electrical energy from the waste heat will immensely contribute towards environmental preservation [1]. More than two-thirds of the industrial energy is wasted as heat. Thermoelectric materials can directly convert waste heat into electrical power and have attracted significant attention for electricity generation through waste heat recovery [1-4]. Among various materials as potential thermoelectric, PbTe based systems e.g., PbTe-SnSe/PbS/SrTe/TI/PbS/SbSe are reported in the literature with high *zT* (up to 2.2) in the mid-temperature range (600-900K) [Figure 5.01.(a)] [1-6]. The low thermal conductivity, large thermopower, and maximum electrical conductivity make *p*-type PbTe superior compared to other systems [1-9]. But environmental concern limit its large-scale application due to toxicity associated with Pb, which motivated for exploring alternative materials. Among various options, tin telluride (SnTe) based system which is a lead-free homologue of PbTe and identical electronic structures, has recently attracted enormous attention for the thermoelectric power generation [10,11]. But immense intrinsic hole carrier concentration (>10^{21} cm^{-3}) associated with the lattice Sn vacancies (V_{Sn}), high electrical thermal conductivity, and sizeable energy gap (ΔE ~ 0.3-0.4 eV) between the light hole (*L* point) and heavy hole (Σ point) valence bands compared to PbTe (ΔE ~ 0.17 eV) are observed. Hence the Seebeck coefficient or Thermopower (S) becomes small resulting in a low thermoelectric figure of merit (*zT*) and an inferior thermoelectric [10, 12].

The ability of a material to produce thermoelectric power from the thermal energy efficiency is measured by a dimensionless parameter called a thermoelectric figure of merit $zT = \left(\frac{S^2\sigma}{\kappa}\right)T$, where *T* is the temperature, $S^2\sigma$ is power factor (PF) and a key controlling parameter to achieve high performance, $\kappa = \kappa_{el} + \kappa_{lat}$ is thermal conductivity and is the sum of lattice thermal conductivity(κ_{lat}) through lattice vibrations and charge carriers (κ_{el}). These parameters are determined by the details of the electronic structure and scattering of charge carriers and are not independently controllable. To achieve high *zT*, one needs to either maximize the PF or minimise the thermal conductivity. The challenge is to engineer thermoelectric materials having simultaneously high electrical conductivity (σ), large thermopower (*S*) and low thermal conductivity (κ) in the same material. It is well understood with standard charge-transport theory that S and σgoes in the opposite directions, so with doping, a balance needs to be achieved to

obtain high PF, and this is performed in a semiconductor with optimum carrier concentration [13]. PF can be improved by either development of new semiconductor materials or optimizing the existing material by alloying. Low lattice thermal conductivity can be obtained through nano-structuring [2]. There are many reports where the performance of SnTe system has been enhanced by various means. Sb alloying in SnTe increased the *zT* to ~1 by reducing the lattice thermal conductivity (κ_{lat}) to the theoretical minimum value ($\kappa_{lat(min)}$~ 0.5$Wm^{-1}K^{-1}$) of SnTe with the concomitant improvement in electronic conductivity (σ) by optimization of *p*-type carrier concentrations [14]. On the other hand Sn self-compensational one shows an effective way of lowering the large hole carrier concentration of SnTe [14, 15]. *S* is improved by formation of resonant level in valence band (VB) by In doping, VB convergence by alloying with Cd, Hg, Ag, Mg and Mn [9,11,14,16-25]. Presence of resonant level induced by In doping and band convergence enabled by the Ag doping together in SnTe increases the *zT* up to 1 at 856 K [17].

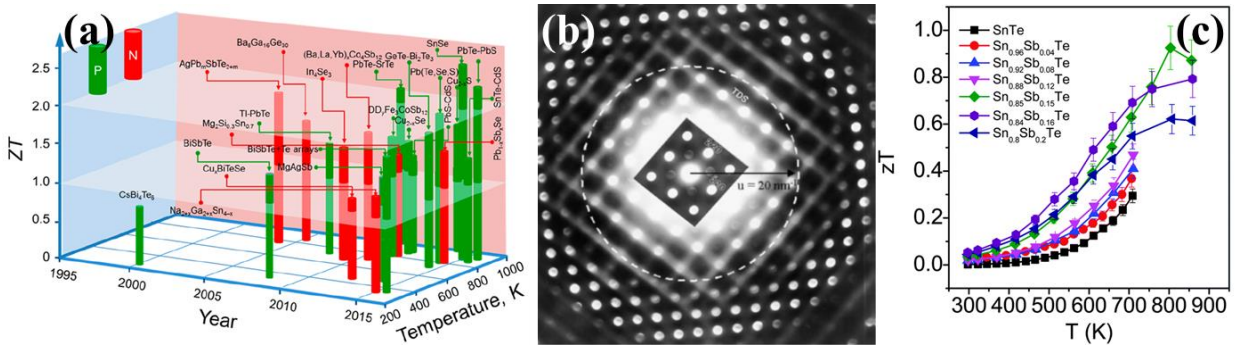

Figure 5.01.*(a) Current state-of-the-art bulk thermoelectric materials: the thermoelectric figure of merit (zT) as a function of temperature and year illustrating important milestones. Copyright (2017) by American Institute of Physics [2].(b) Electron diffraction pattern showing the presence of diffuse scattering streaks between the Bragg reflections due tothermal vibration (phonon) of the atoms in the crystals. Copyright (2003) by Elsevier [46].(c) Thermoelectric figure of merit (zT) of $Sn_{1-x}Sb_xTe$,with* a *zT* ~ 1 for $Sb_{0.15}$ at T = 800 K. *Copyright (2016) by The Royal Society of Chemistry 2016 [35].*

Lattice thermal conductivity(κ_{lat}) is related to thermal phonon vibration and phonon scattering in the host matrix. Generally, reduction in κ_{lat} has been reported through the formation of point-defects and grain boundaries, all-scale hierarchical nano-meso-structures, endotaxial nanostructures in the bulk matrix, lattice of complex crystal structure, soft phonon modes, rattling

modes, resonant bonding levels, and anisotropic layered structures [11,26-32]. In case of SnTe system, the experimental κ_{lat} is reported to be ~2.88 $Wm^{-1}K^{-1}$ at 300 K but as already mentioned, the theoretical limit for minimum lattice thermal conductivity (κ_{min}) is ~0.5 $Wm^{-1}K^{-1}$ [14]. Although there are reports to reduced k_{lat} (1 $Wm^{-1}K^{-1}$ at RT) in this system by introduction of secondary phase nano-precipitates e.g., CdS and HgTe and alloy formation, but there are few reports which could successfully reduce the κ_{lat} of SnTe near to its theoretical minimum value i.e. $\kappa_{min} = 0.5$ $Wm^{-1}K^{-1}$; κ_{lat}~0.6 $Wm^{-1}K^{-1}$ at 900 K with zT~1.3 in $Sn_{0.94}Mn_{0.17}Te$, κ_{lat}~ 0.78 $Wm^{-1}K^{-1}$ at 856 K with zT~1.2 in p-type $Sn_{0.94}Mg_{0.09}Te$ and κ_{lat}~ 0.67 $Wm^{-1}K^{-1}$ at 800 K [14,17,19,22-24].

The improvement in thermal conductivity in Sb-doped SnTe is attributed to the formation of the nanostructure. Moreover, Sb incorporation in SnTe affects the band structure and carrier concentrations. In PbTe, Sb plays an important role to reduce κ_{lat} [8, 33]. Substitution of Sb in PbTe shows a significant increase in the thermoelectric performance at higher temperatures due to the formation of Sb donor states below the conduction band of PbTe [8, 33, 34]. Sb in PbTe forms nanostructures via matrix encapsulation and show k_{lat} of ~0.8 $Wm^{-1}K^{-1}$ at 300K [33]. Addition of Sb in $Pb_{9.6}Sb_yTe_{10-x}Se_x$ (y<0.2) is reported to form the spontaneous nano-inclusions of Sb rich phases, which resulted in low κ_{lat} [5].

Sb doping (x = 0.15) in SnTe leads to the formation of distinct nanostructures which is responsible for achieving low thermal conductivity in the system with a zT ~ 1 at T = 800 K shown in [Figure 5.01.(c)] [35]. The exact form of the nanostructure is very interesting and the origin of which is found to be Sb occupying both regular Sn site and Te anti-site positions on the {111} planes in the host SnTe lattice. This modifies the {111} interplanar spacing (d_{111}) of the host lattice and results in superstructures as observed in the electron diffraction pattern. This nanostructural feature is different than nano-sized precipitates which is generally observed. In the present case, there is no precipitate formation. The location of Sb at both the lattice sites is further supported by the first principle based calculation. In addition to this, it also suggests that while the areas with Sb at the regular site gives large thermopower, the areas with anti-sites forming superstructure are contributing towards low lattice thermal conductivity and both together increases zT to ~1 in this system [36].

5.2 Experimental Methods

$Sn_{1-x}Sb_xTe$ (x = 0.04, 0.08, 0.15) are synthesized by the melting reaction of Sn(Alfa Aesar 99.99+ %), Sb (Alfa Aesar 99.999+ %)and Te (Alfa Aesar 99.999+ %) in a vacuum sealed quartz tube (10^{-5} Torr), which is heated to 900 ^{o}C over 12 hrs, then stay for 10 hrs, and cool to Room Temperature in 18 hrs. All the transmission electron microscopy imaging was performed in aberration-corrected FEI TITAN 80-300 kV TEM as well as 200 kV Tecnai microscopes. Electron transparent TEM samples are prepared by conventional mechanical thinning followed by Ar ion milling to generate large electron transparent thin areas. The sample pieces are cut from the solid ingot, synthesized by melting and annealing procedures.

5.3 Computational methods

The electronic structures of SnTe with different Sb atom substitutions are calculated using DFT based Wien2k code [37]. Two different cases of interest are considered, (*i*) StructureI Sb of 18.75% (Sb_{Sn}) and (*ii*) Structure II (18.75% Sb_{Sn+Te}, 12.5% Sb_{Sn} + 6.5% Sb_{Te}).Generalized gradient approximation (GGA) is employed with Perdew- Burke-Ernzenhof(PBE) functional for optimization of lattice parameters and minimization of forces. SnTe is known to be rock salt structure. The optimized SnTe lattice parameter is a= 6.41 Å. 14×14×14 k-mesh is used for SnTe unit cell and reduced proportionally to the number of unit cell in each direction for the supercell calculations. For Sb-doped case, a 2×2×1 supercell is created. Structural models are shown in Figure 5.08.(a) & (b) where Sn and Te are replaced with Sb in {111} planes. The criteria of convergence for force, energy and electronic charge are set to below 1 mRy/a.u., 0.0001 Ry and 0.001 e, respectively. The Muffin Tin radii are chosen such that they do not overlap. The K_{max} value for plane wave basis is 8.00/R_{MT} (min) (R_{MT} (min) is the Muffin tin radius of the smallest atom). For the calculation of band gaps, the modified Becke-Johnson potential (mBJ) is used [38]. Spin-orbit coupling is considered to plot band structure. semi-classic Boltzmann transport theory in the constant time approximation is used to calculate Thermopower of these Structures using BoltzTraP code [39,40].

5.4 Results and Discussion

5.4.1 Structural Characterization of $Sn_{1-x}Sb_xTe$ alloy

We begin with the microstructural features observed under TEM bright field and HRTEM images for three different Sb concentrations in $Sn_{1-x}Sb_xTe$ (x = 0.04, 0.08 and 0.15). Figure 5.02 is the TEM bright field images showing diffraction contrast features in three different samples. Samples with x = 0.04 and 0.08 Sb do not show any features and confirm the formation of a single-phase solid solution between Sb and SnTe [Figure 5.02.(a) & (b)].

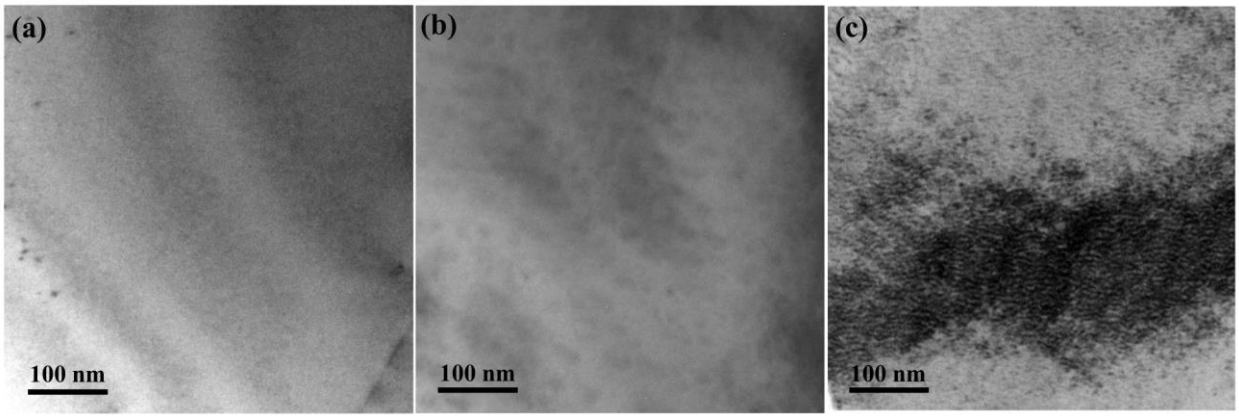

Figure 5.02. *TEM bright field images of $Sn_{1-x}Sb_xTe$ alloy at, (a) x = 0.04, (b) x=0.08, and (c) x=0.15. Ripple-like dark-bright contrast is visible for Sb0.15 alloy but no such contrast is observed from low magnification images. Copyright (2017) by American Institute of Physics [36].*

Ripple-like strain contrast areas are visible for x = 0.15 sample, but there is no contrast due to secondary phases, also precipitates with any boundary between these features and the host material is not observed [Figure 5.02.(c)].The electron diffraction (ED) patterns from three different samples are given in Figure 5.03. All the ED patterns have been acquired along <112> zone axis (Z.A.). The spots are indexed and are indicated in the respective figures. No additional spots due to secondary precipitates are observed in $Sb_{0.04}$ and $Sb_{0.08}$ samples but super-lattice spots along with streaks due to thermally diffused scattering are observed for sample $Sb_{0.15}$ [Figure 5.03.(c), Figure 5.06, Figure 5.07].

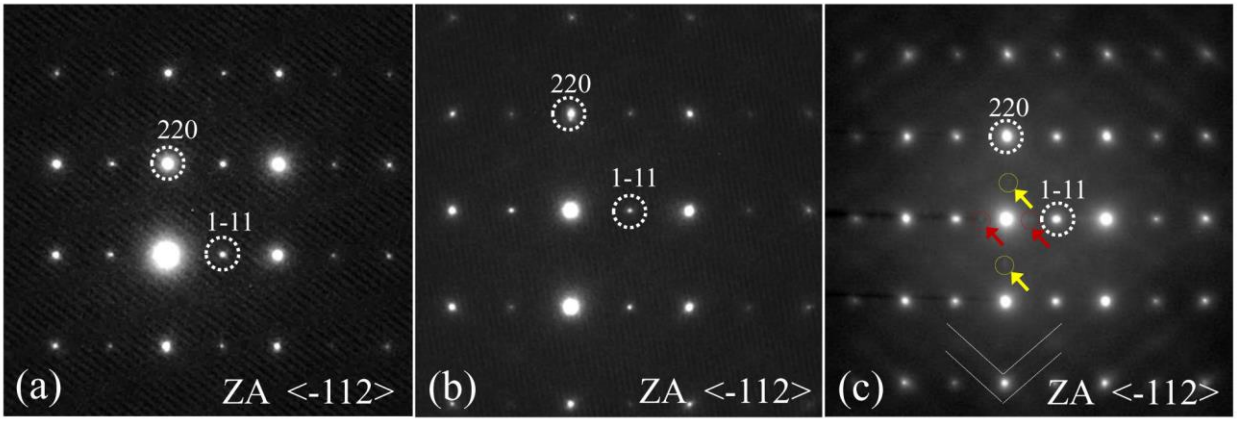

Figure 5.03. *Electron diffraction pattern along <112> Z.A. of (a) x = 0.04, (b) x = 0.08, and (c) x = 0.15. One can notice the super-lattice spots at ½{111} and thermal diffused scattering between the primary Bragg spots. No such super-lattice spots or thermal diffused scattering are observed for alloy* $Sb_{0.04}$ *and* $Sb_{0.08}$*. Copyright (2017) by American Institute of Physics [36].*

Figure 5.04. Shows the HRTEM images and corresponding fast Fourier transformed (FFT) diffractograms of three different samples. One interesting feature is the structural modulation in SnTe host lattice with Sb incorporation which results in super-lattice spots both in the ED and FFT pattern for $Sb_{0.15}$ alloy. This structural modulation can be observed both in terms of the criss-cross line running along {111} planes with 60° angles between them and are marked in the images and corresponding super-lattice spots in FFT [Figure 5.04.(c)]. The frequency of such crisscross lines is less and appearance are faint in samples $Sb_{0.04}$ and $Sb_{0.08}$ Due to the periodicity of these lines, ED does not show any super-lattice spots [see Figure 5.04.(b) for $Sb_{0.08}$].

However, this feature is not uniformly present throughout the volume and two different microstructures are present, with and without modulated regions [Figure 5.05]. This indicates that the structural modulation observed might be due to the difference in Sb substituting the SnTe host crystal. Theory calculation suggests (see discussion later) that Sb can replace both the regular Sn site and Te anti-site which is not only stable energetically but also modifies the local d_{111}inter planar spacing through an additional chemical interaction between Sb at two different lattice sites.

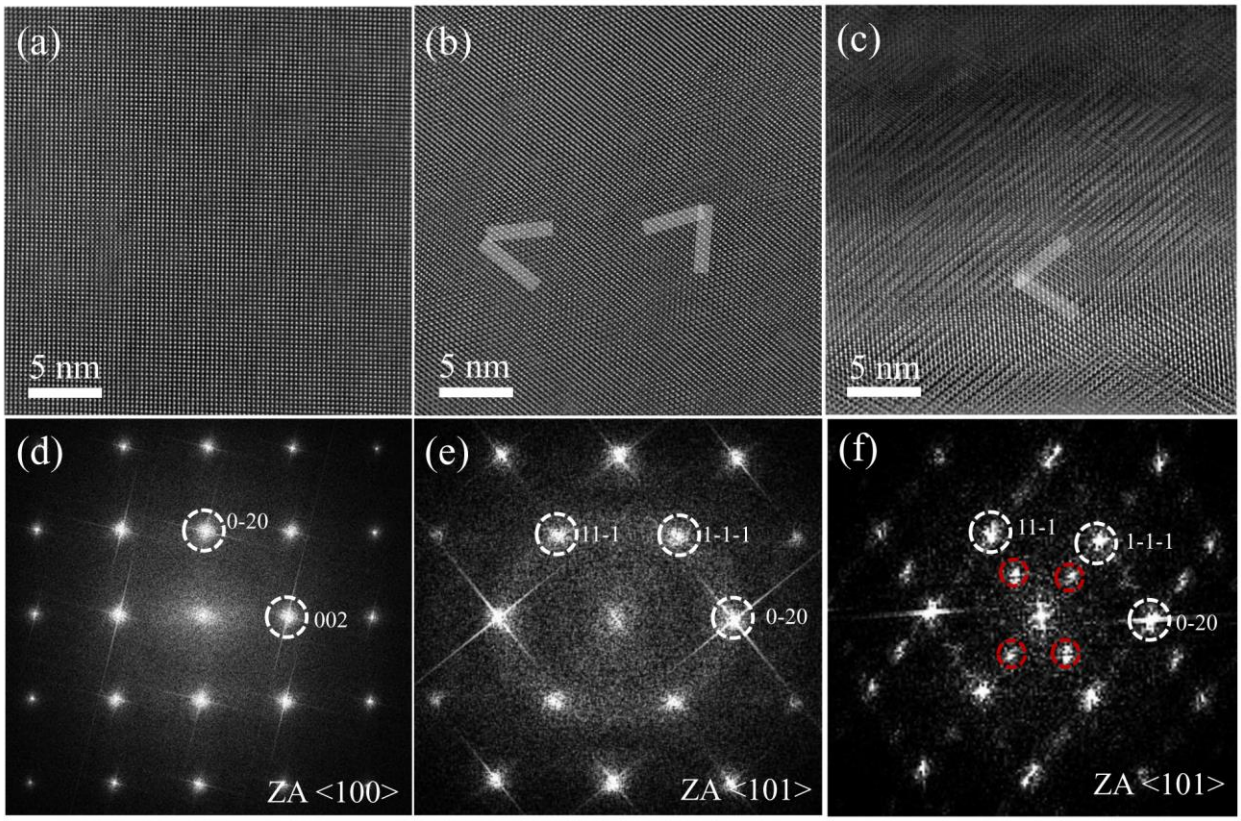

Figure 5.04. *(a)-(c) HRTEM images and (d)-(f) corresponding FFT pattern of $Sn_{1-x}Sb_xTe$ alloy at, x = 0.04, x = 0.08, and x = 0.15, respectively. Superlattice spots at ½{111} are marked for $Sb_{0.15}$ alloy. Note that no diffused streak is observed from FFT pattern because their origin is dynamic thermal disorder but not static disorder. Super-lattice spots have origin in criss-cross line like feature in $Sb_{0.15}$ alloy and such criss-cross lines can be seen in fewer numbers in $Sb_{0.08}$ alloy and rarely in $Sb_{0.04}$ alloy sample. Copyright (2017) by American Institute of Physics [36].*

Systematic tilting experiment is carried out for the rock salt structures shown in Figure 5.06. to confirm the origin of superlattice spots. No secondary set of the diffraction pattern is observed along different zone axis of the host rock salt SnTe crystal. This confirms that the origin of such microstructure is not due to Sb-rich subsequent hexagonal phase forming intergrowth structure, rather local Sb_{Sn}-Sb_{Te} interaction between two different lattice sites leading to structural modulation in the same single crystal rock salt phase.

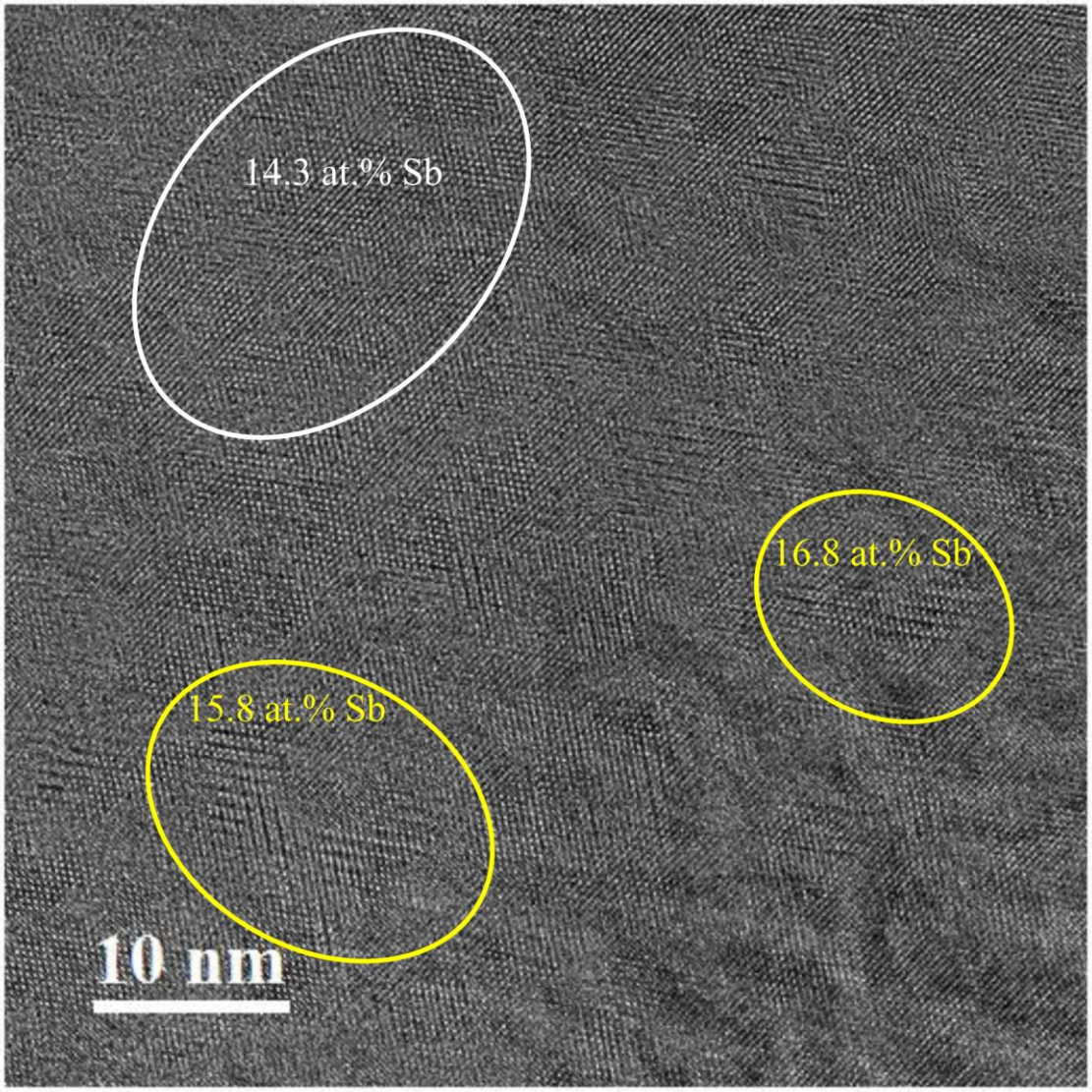

Figure 5.05. *HRTEM images for $Sb_{0.15}$ alloy showing two different phase areas, one with criss-cross line where Sn is replacing both Sn and Te sites and areas without criss-cross line like features where Sb is replacing only Sn site. Local EDS measurement shows similar concentrations of Sb in two different regions. The boundary between these two-phase regions is coherent. Copyright (2017) by American Institute of Physics [36].*

To derive more insight on the origin of such structural feature associated with crisscross network of lines at 60° angle between them and associated super-lattice spots in the electron diffraction pattern, two different alloy compositions i.e.structure-I with Sb replacing Sn site and structure-II, where Sb replacing both Sn and Te sites, are considered for the theoretical calculation.

Figure 5.08.(a) & (b) shows a schematic structural model for the two-different alloy structures. Sb is placed close to each other on the Sn and Te (111) planes to check for any resulting mutual interaction between Sb atoms. The stability of Sb at Sb_{Sn}+Sb_{Te} is found to be energetically more stable (cohesive energy 2.92 eV/atom) compared to Sb_{Sn} site (2.74 eV/atom) alone. The interatomic/planar spacing $d_{111}$is found to be different i.e. 5.35 to 5.58 and 5.55 Å for Sb at Sb_{Sn}+Sb_{Te} and Sb_{Sn}sites, respectively [Figure 5.08.(a) & (b)] and gives rise to super-lattice spots in the calculated diffraction pattern [Figure 5.08.(c) & (d)]. This modulation can be understood by considering the charge density plot. Figure 5.08.(e) & (f) are the charge density plots for two different structures along 001 direction. Interatomic distances are indicated and most of the lattice distances are shorter in structure-II compared to structure-I. The distance between Sb-Sb in two different lattice sites is 2.92 Å, which is significantly shorter compared to other interatomic distance. One can notice that Sb_{Sn}-Sb_{Te} and Sb_{Sn}-Te interaction through hybridization and this is dominated by the *p* orbitals. This is responsible for locally changing the d_{111} interplanar spacing. Thus, this supports that Sb may not form separate crystallographic phase from the SnTe host rather locally modulate d_{111} spacing of the host lattice through additional interaction between Sb at two different lattice sites. This is responsible for the observed crisscross like microstructure and superlattice spots in the ED pattern. The role of such microstructure on phonon scattering resulting in low κ_{lat} is further discussed.

Structural features influence theκ_{lat}, band structure, *S* and σ. We have observed two different regions or phases in the $Sb_{0.15}$ sample, one with super lattice spots and criss-cross lines in the ED pattern and another without such feature. Local energy dispersive X-ray measurement (EDS) confirms almost same concentrations of Sb in two different regions [Figure 5.05]. The first area corresponds to Sb in Sb_{Sn}+Sb_{Te} sites and the second area to Sb_{Sn} site with coherent boundary

between these two regions.Later, result is presented based on theoretical calculation on the respective contributions of two different phases on various parameters in the *zT* equation.

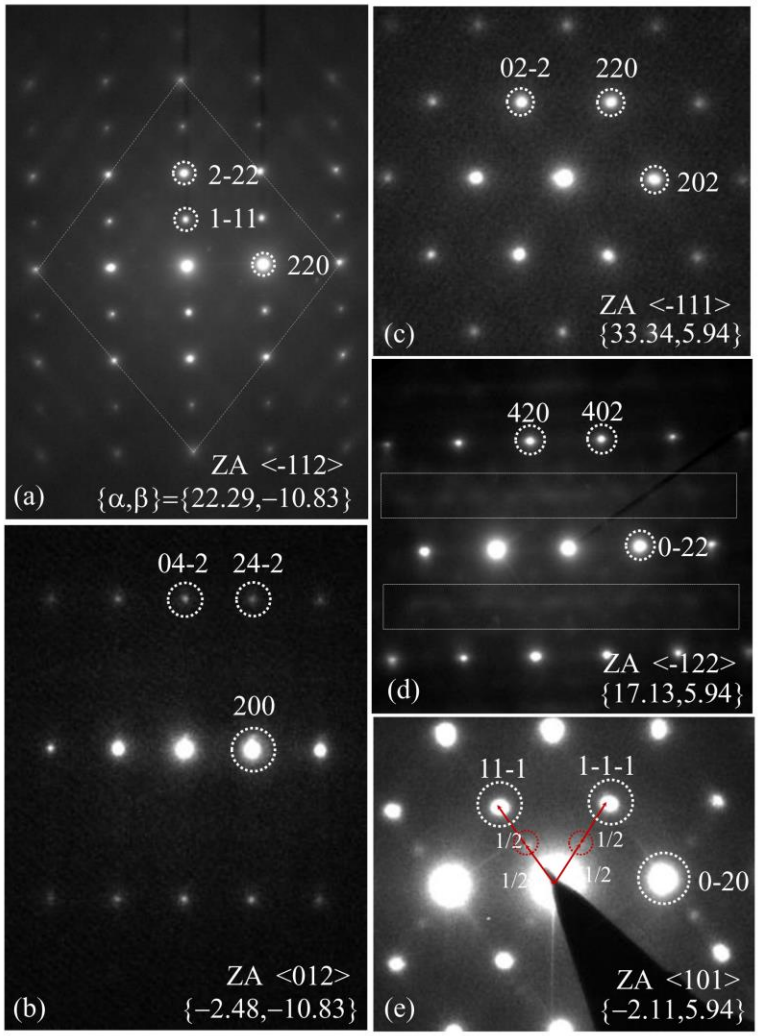

Figure 5.06. *Tilt series of electron diffraction pattern of host SnTe rock salt structure showing presence of no secondary spots due to different crystallographic phases or intergrowth structure for $Sb_{0.15}$ alloy. Diffused streaks in between Bragg spots are marked with dotted rectangular box in (d). Notice this diffused streak line has diffused spots along the line and the origin of such feature is due to a disordering in deformation vector related to two substitutional or vacant sites. Copyright (2017) by American Institute of Physics [36].*

5.4.2 Role of phonon scattering in electron diffraction pattern

The presence of nanostructures has a significant influence on reducing κ_{lat} compared to the solid solution alloying [1,7,14,17,19,22,25,26,31,35,41-43]. In the present system, there are four different contributors to decrease the κ_{lat}; intrinsic V_{Sn}, Sb substitution in Sn site (Sb_{Sn}) and Sb at Sb_{Sn}+Sb_{Te} sites forming distinct feature giving rise to super-lattice spots in the ED pattern. Among these, the last one has the significant influence on decreasing κ_{lat} as explained before. However, this feature is different compared to the earlier nano-structural precipitates or intergrowth structure. In other words, the present features are part of the host lattice and only introducing the modulation in d_{111} lattice planes forming superstructure. Super-lattice structures affect the lattice thermal conductivity, also modification of the phonon spectrum, phonon localization, and diffuse or specular scattering of phonons at interfaces due to acoustic mismatch [44].

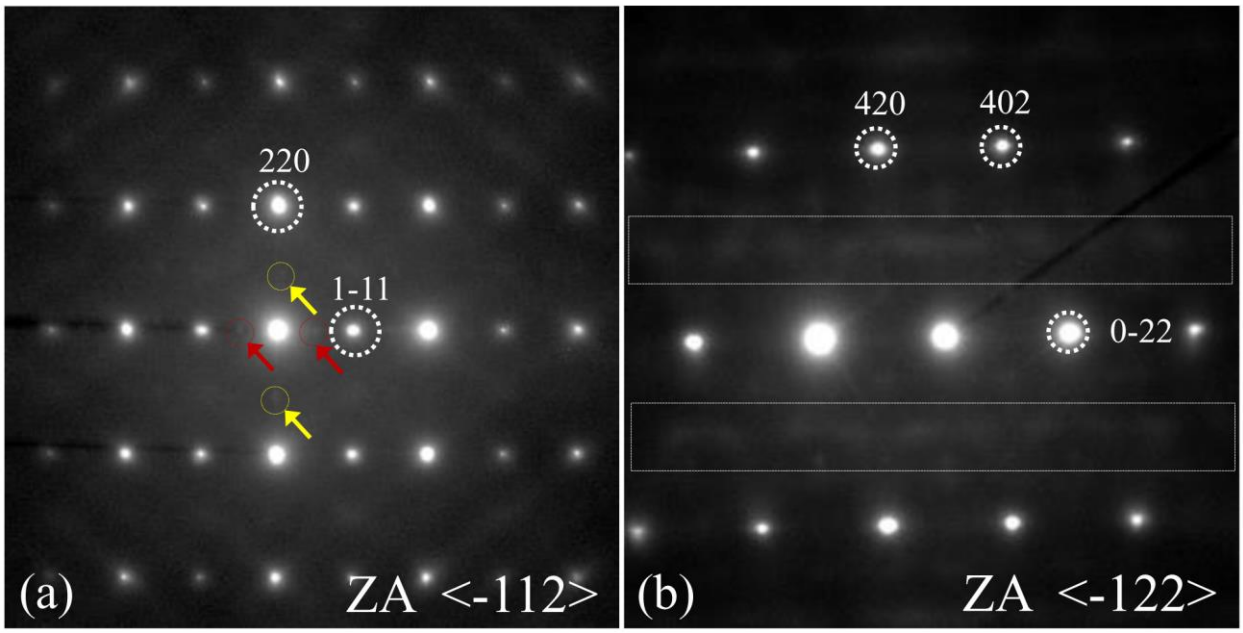

Figure 5.07. *Electron diffraction patterns of $Sb_{0.15}$ alloy along (a) <112>, and (b) <122> zone axis. Diffused streaks between Bragg spots and streaks in between Bragg spots are visible in (a) and (b), respectively. Copyright (2017) by American Institute of Physics [36].*

In fact, electron diffraction pattern shows diffused streaks due to additional phonon scattering in $Sb_{0.15}$ alloy case. Signature of phonon scattering in electron diffraction pattern appears

as diffused streak. This has the thermal but not the static origin. Due to structural modification such streak is not observed in the FFT pattern [45-46]. Three different features are observed in the DP in $Sb_{0.15}$; broadening of spots, diffused streak between Bragg spots, and 2D diffused sheet in between Bragg spots due to phonon scattering [Figure 5.07].

Broadening of the spots is observed in the system with large concentrations of point defects (in the present case it is due to native V_{Sn}). The origin of diffused streak between Bragg spots is attributed to transverse long low frequency waves with wave fronts perpendicular to closely packed strings of atoms. Phonon vibration during electron scattering perturbs the crystal potential and if this is not periodic, it results in diffuse scattering distribution between Bragg's spots in DP [Figure 5.01.(b)] [46]. The 2D sheet in between Bragg spots has diffused broad spots along the line as well as around the primary Bragg spots [Figure 5.07(b)]. Such 2D sheet may have originated due to a disordering in deformation vector related to two substitutional or vacant sites and in the present system such sites may be formed by any of the following combinations; (Sb_{Sn}+Sb_{Sn} or Sb_{Sn}+Sb_{Te}) or two vacancy V_{Sn} or between (Sb_{Sn} or Sb_{Te}) and V_{Sn}. All these features can contribute to the overall phonon scattering and reduce the thermal conductivity of the system close to the theoretical value of SnTe.

5.4.3 Role of dopant at different occupancy/site by DFT

As the observation of Sb in the Te anti-site is not intuitive and being primary focus of the present paper, we, therefore provide further information on the changes in the electronic structure due to such substitution of Sb in the SnTe host lattice. The band gap of pristine SnTe is found to be 0.052 eV from the present calculation [Figure 5.09.(b)]. However, the experimental band gap values of SnTe has been reported to be 0.18 eV at room temperature [12]. The higher reported experimental band gap values of SnTe may be either due to the intrinsic large hole carrier concentration which shifts the Fermi level into the valence band or intrinsic underestimation of predicted band gap values by the theoretical calculation. We have compared the density of states of two different Sb-doped SnTe structures (I & II) with the pristine SnTe [Figure 5.09.(b)-(d)]. The calculated band structure and density of state (DOS) of Structure I&II are shown in Figure 5.09 (b) & (c). In general, Sb has three valence electrons and can show ambipolar behaviour [47].

Therefore, Sb in Sn site is expected to give *n*-type conductivity and in Te site *p*-type conductivity. Pristine SnTe exhibits *p*-type conductivity due to intrinsic V_{Sn}. The calculation shows a similar trend i.e. Sb_{Sn} is *n*-type and Sb_{Te} is *p*-type. The regions where lattice containing Sb_{Sn} will reduce the intrinsic *p*-conductivity and areas with Sb_{Sn+Te} will have little or no effect depending on the relative proportions of Sb_{Sn} to Sb_{Te}.

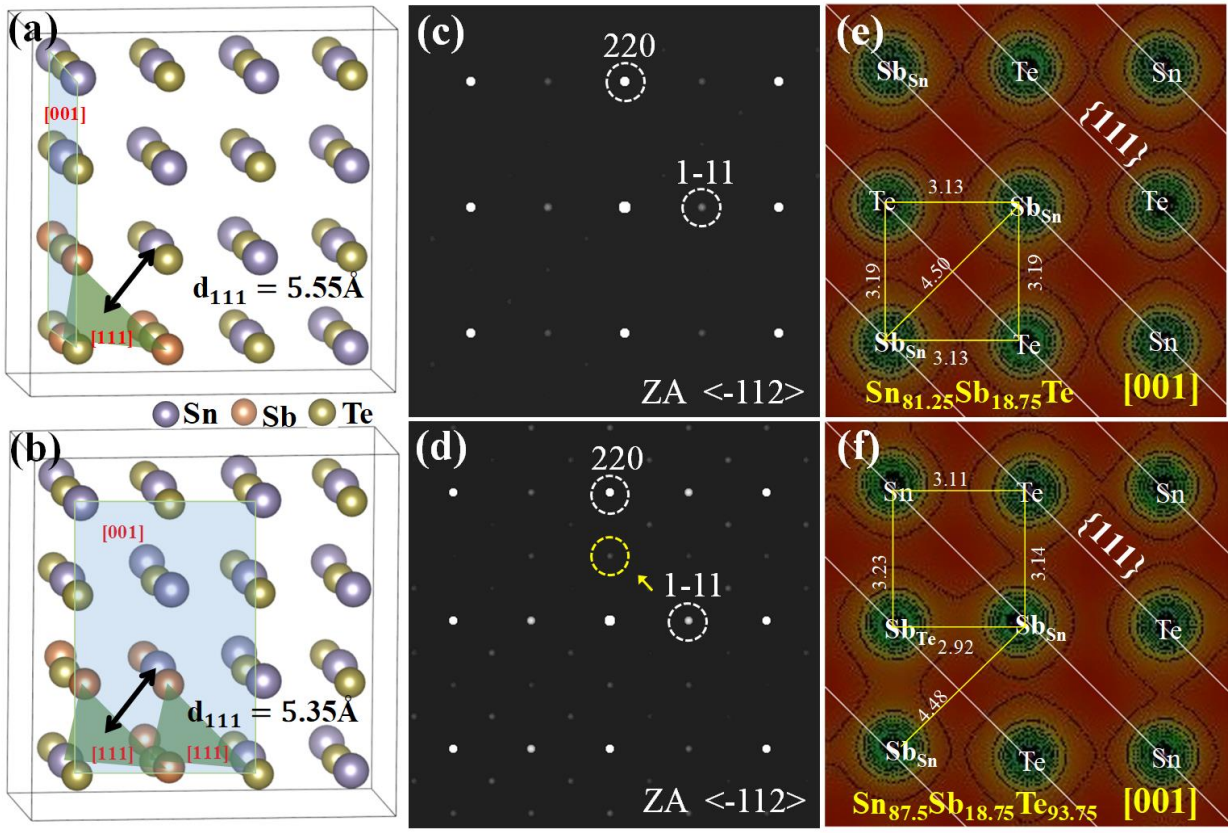

Figure 5.08. *Schematic of structure (a) I (Sb_{Sn}), and (b) II (Sb_{Sn+Te}). Calculated diffraction pattern for two different structures are given in (c) & (d). Superlattice spots can be observed in structure II. Charge density plots for two different structures are given in (e) & (f). One can notice that in structure II, Sb_{Sn}-Sb_{Te} and Sb_{Sn}-Te interaction through hybridization and this is dominated by the p orbitals. This is responsible for locally changing the d_{111} interplanar spacing. Copyright (2017) by American Institute of Physics [36].*

Experimentally, it is observed that *p*-carrier concentrations decrease slightly from 3×10^{20} to 2.2×10^{20} cm^{-3} even after alloying with Sb up to 15 at.%. This suggests that Sb has the high probability to occupy anti site positions in the lattice and this is further supported by the theoretical calculation of energy. Though experimentally the carrier concentration is not changed significantly, no variation in the *zT* are expected. Further improvement in power factor is possible by decreasing *p*-carrier concentration either by activating Sb in the Sn site or by reducing its occupancy at the anti-sites.However, the number of states increases at the Fermi level and this is higher in the case of Sb_{Sn} compared Sb_{Sn+Te}. SnTe shows *s*-*p* hybridization, where Sn *p* and Te *s* states together form conduction band and Sn *s* and Te *p* form valence band edges. The density of states (DOS) is dominated by *p* states [Figure 5.09.(b)-(d)]. Upon Sb substitution in Sn site (structure-I), the number of states increases significantly near Femi level (E_F) compared to structure-II contributed mostly by Sb *p* states. This will have an effect on increasing the conductivity $\sigma(\epsilon)$. It is known that the *S* is proportional to the logarithmic derivate of the conductivity [48]. Therefore, increase in states near E_F results in the increase in thermopower *S* in case of structure-I. Structure-II does not show such effect.

We further calculated the transport properties of Structure-I and Structure-II using the Boltzmann transport theory in the constant scattering time approximation [40]. Thermopower for a system of independent electrons interacting with static scatterers is given by the Mott's formula as;

$$S = \frac{\pi}{3}\left(\frac{k_B^2 T}{e}\right)\left(\frac{d\, ln\sigma(\epsilon)}{d\epsilon}\right)_{\epsilon=0} \qquad \ldots. (1)$$

and

$$\sigma = \int_{-\infty}^{\infty}\left(-\frac{\partial n_F}{\partial \epsilon}\right)\sigma(\epsilon)\, d\epsilon \qquad \ldots. (2)$$

Where, $\sigma(\epsilon), \epsilon, n_F, k_B, e$ are electrical conductivity, energy, density of states at Fermi level, Boltzmann constant, charge of electron respectively [48].

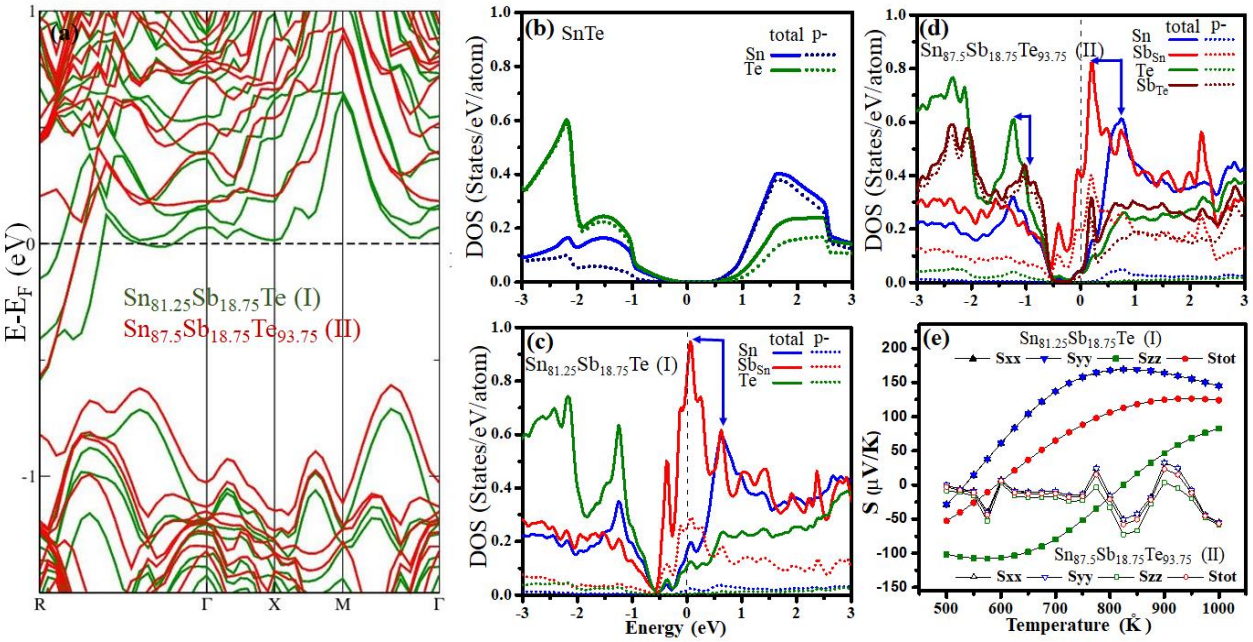

Figure 5.09. *(a) Band structure of structure I & II. Density of states of (b) pristine SnTe, (c) structure-I, and (d) structure-II. (e) Calculated thermopower S against T for two different Sb substituted structures. Copyright (2017) by American Institute of Physics [36].*

However, electrical thermal conductivity $\kappa_{el}$is influenced by carrier concentration or σ through the Wiedemann-Franz relation $\kappa_{el} = L\sigma T = Lne\mu T$where L is the Lorenz number, ne is the total number of carriers,μ is the mobility,σ is the conductivity and T is the temperature. Therefore, any decrease in ne or σ and will decrease k_{el} and decreases the zT. It is a challenge to increase S without suppressing electrical conductivity, and not clear whether it needs a different system or known material [13]. We found that S is improved in Structure-I and κ_{lat} is improved in Structure-II belong to the same experimental ingot $Sb_{0.15}$having highest zT among series.

5.5 Conclusion

In conclusion, the nature of structural features in Sb alloyed with SnTe is elucidated. It is found that Sb incorporation in SnTe lattice can take place both at the substitutional Sn sites and Te anti-sites. Sb at Sb_{Sn}+Sb_{Te} is energetically more stable than Sb_{Sn}. Sb_{Sn}+Sb_{Te} leads to local modulation of d_{111} interplanar spacing in SnTe host lattice and results in criss-cross lines like structure and super-lattice spots in image and ED pattern, respectively. This is not intergrowth structure, rather superstructure responsible for the near theoretical thermal conductivity of SnTe in the system. Phonons are scattered strongly from such structure, which is evident from the strong diffused streak and 2D disordering in the ED pattern of $Sb_{0.15}$ composition. While Sb_{Sn}+Sb_{Te} responcible for low thermal conductivity, the Sb_{Sn} regions contribute to higher conductivity and S, thus leading to zT~1 in the $Sb_{0.15}$ system.

5.6 Bibliography

[1] K. Biswas, J. He, I.D. Blum, C.I. Wu, T.P. Hogan, D.N. Seidman, V.P. Dravid, M.G. Kanatzidis, Nature 489, 414 (2012).

[2] G. Tan, L.-D. Zhao, and M. G. Kanatzidis, Chem. Rev. **116,** 12123 (2016).

[3] R.W.Boydston, Phys. Rev. **30(6),** 911 (1927).

[4] D.M. Rowe, ed. *CRC handbook of thermoelectrics*. CRC press, (1995).

[5] P. F. Poudeu, J. D'Angelo, H. Kong, A. Downey, J. L. Short, R. Pcionek, T. P. Hogan, C. Uher, and M. G. Kanatzidis, J. Am. Chem. Soc. **128,** 14347 (2006).

[6] S. N. Girard, J. He, X. Zhou, D. Shoemaker, C. M. Jaworski, C. Uher, V. P. Dravid, J. P. Heremans, and M. G. Kanatzidis, J. Am. Chem. Soc. **133,** 16588 (2011).

[7] K. Biswas, J. He, Q. Zhang, G. Wang, C. Uher, V. P. Dravid, and M. G. Kanatzidis, Nat. Chem. **3,** 160 (2011).

[8] K. F. Hsu, S. Loo, F. Guo, W. Chen, J. S. Dyck, C. Uher, T. Hogan, E. Polychroniadis, and M. G. Kanatzidis, Science **303,** 818 (2004).

[9] Y. Pei, X. Shi, A. LaLonde, H. Wang, L. Chen, and G. J. Snyder, Nature **473,** 66 (2011).

[10] R. Brebrick and A. Strauss, Phys. Rev. **131,** 104 (1963).

[11] Q. Zhang, B. Liao, Y. Lan, K. Lukas, W. Liu, K. Esfarjani, C. Opeil, D. Broido, G. Chen, and Z. Ren, Proceedings of the National Academy of Sciences **110,** 13261 (2013).

[12] L. Rogers, Journal of Physics D: Appl. Phys. **1,** 845 (1968).

[13] J. R. Sootsman, D. Y. Chung, and M. G. Kanatzidis, Angew. Chem Int. Edi. **48,** 8616 (2009).

[14] G. Tan, F. Shi, H. Sun, L.-D. Zhao, C. Uher, V. P. Dravid, and M. G. Kanatzidis, J. Mater. Chem. A **2,** 20849 (2014).

[15] S. Acharya, J. Pandey, and A. Soni, Appl. Phys. Lett. **109,** 133904 (2016).

[16] A. Banik, U. S. Shenoy, S. Anand, U. V. Waghmare, and K. Biswas, Chem. Mater. **27,** 581 (2015).

[17] A. Banik, U. S. Shenoy, S. Saha, U. V. Waghmare, and K. Biswas, J. Am. Chem. Soc. **138,** 13068 (2016).

[18] K. Ahn, K. Biswas, J. He, I. Chung, V. Dravid, and M. G. Kanatzidis, Energy Environ. Sci. **6,** 1529 (2013).

[19] G. Tan, F. Shi, J. W. Doak, H. Sun, L.-D. Zhao, P. Wang, C. Uher, C. Wolverton, V. P. Dravid, and M. G. Kanatzidis, Energy Environ. Sci. **8,** 267 (2015).

[20] M. Zhou, G. J. Snyder, L. Li, and L.-D. Zhao, Inorg. Chem Frontiers **3,** 1449 (2016).

[21] G. Tan, L.-D. Zhao, F. Shi, J. W. Doak, S.-H. Lo, H. Sun, C. Wolverton, V. P. Dravid, C. Uher, and M. G. Kanatzidis, J. Am. Chem. Soc. **136,** 7006 (2014).

[22] G. Tan, F. Shi, S. Hao, H. Chi, L.-D. Zhao, C. Uher, C. Wolverton, V. P. Dravid, and M. G. Kanatzidis, J. Am. Chem. Soc. **137,** 5100 (2015).

[23] X. Tan, H. Shao, J. He, G. Liu, J. Xu, J. Jiang, and H. Jiang, Phys. Chem. Chem. Phys. **18,** 7141 (2016).

[24] J. He, X. Tan, J. Xu, G.-Q. Liu, H. Shao, Y. Fu, X. Wang, Z. Liu, J. Xu, and H. Jiang, J. Mater. Chem. A **3,** 19974 (2015).

[25] H. Wu, C. Chang, D. Feng, Y. Xiao, X. Zhang, Y. Pei, L. Zheng, D. Wu, S. Gong, and Y. Chen, Energy Environ. Sci. **8,** 3298 (2015).

[26] L.-D. Zhao, X. Zhang, H. Wu, G. Tan, Y. Pei, Y. Xiao, C. Chang, D. Wu, H. Chi, and L. Zheng, J. Am. Chem. Soc. **138,** 2366 (2016).

[27] G. J. Snyder and E. S. Toberer, Nat. mater. **7,** 105 (2008).

[28] L. Bjerg, B. B. Iversen, and G. K. Madsen, Phys. Rev. B **89,** 024304 (2014).

[29] M. K. Jana, K. Pal, U. V. Waghmare, and K. Biswas, Angew. Chem. Int. Edit. (2016).

[30] H. Euchner, S. Pailhès, L. Nguyen, W. Assmus, F. Ritter, A. Haghighirad, Y. Grin, S. Paschen, and M. de Boissieu, Phys. Rev. B **86,** 224303 (2012).

[31] L.-D. Zhao, S.-H. Lo, Y. Zhang, H. Sun, G. Tan, C. Uher, C. Wolverton, V. P. Dravid, and M. G. Kanatzidis, Nature **508,** 373 (2014).

[32] L.-D. Zhao, G. Tan, S. Hao, J. He, Y. Pei, H. Chi, H. Wang, S. Gong, H. Xu, and V. P. Dravid, Science **351,** 141 (2016).

[33] J. R. Scotsman, R. J. Pcionek, H. Kong, C. Uher, and M. G. Kanatzidis, Chem. Mater. **18,** 4993 (2006).

[34] J. R. Sootsman, H. Kong, C. Uher, J. J. D'Angelo, C. I. Wu, T. P. Hogan, T. Caillat, and M. G. Kanatzidis, Angew. Chem. **120,** 8746 (2008).

[35] A. Banik, B. Vishal, S. Perumal, R. Datta, and K. Biswas, Energy Environ. Sci. **9,** 2011 (2016).

[36] B. Vishal, R. Sahu, U. Bhat and R. Datta, J. Appl. Phys , **122(5)**, 055102 (2013).

[37] P. Blaha, K. Schwarz, G. K. H. Madsen, D. Kvasnicka, and J. Luitz, *WIEN2k: An Augmented Plane Wave + Local Orbitals Program for Calculating Crystal Properties* (KarlheinzSchwarz, Techn. Universität Wien, Austria, 2001).

[38] F. Tran and P. Blaha, Phys. Rev. Lett. **102,** 226401 (2009).

[39] P. Allen, *Boltzmann theory and resistivity of metals*. (Kluwer International Series In Engineering and Computer Science, Netherlands,1996).219-250.

[40] G. K. Madsen and D. J. Singh, Comput. Phys. Commun. **175,** 67 (2006).

[41] J. He, J. R. Sootsman, S. N. Girard, J.-C. Zheng, J. Wen, Y. Zhu, M. G. Kanatzidis, and V. P. Dravid, J. Am. Chem. Soc. **132,** 8669 (2010).

[42] B. Poudel, Q. Hao, Y. Ma, Y. Lan, A. Minnich, B. Yu, X. Yan, D. Wang, A. Muto, and D. Vashaee, Science **320,** 634 (2008).

[43] Y. Pei, L. Zheng, W. Li, S. Lin, Z. Chen, Y. Wang, X. Xu, H. Yu, Y. Chen, and B. Ge, Adv. Electron. Mater. **2** (2016).

[44] P. Hyldgaard and G. Mahan, Phys. Rev. B **56,** 10754 (1997).

[45] G. Van Tendeloo and S. Amelinckx, Phase Transitions **67,** 101 (1998).

[46] Z. L. Wang, Micron **34,** 141 (2003).

[47] V. Kumar, Phys. Rev. B **48,** 8470 (1993).

[48] M. Jonson and G. Mahan, Phys. Rev. B **21,** 4223 (1980).

[49] J. Pulikkotil and S. Auluck, J. Alloys Compd. **626,** 208 (2015).

Chapter 6

Microstructural and magnetic study of $Ni_{50}Mn_{37/35}Sn_{13/15}$ Heusler alloy thin film

This chapter emphasizes the important $Ni_{50}Mn_{37/35}Sn_{13/15}$ alloy thin films grown by pulsed laser deposition. The Curie temperatures of the films are 316 and 334 K, respectively. The microstructure of the films consists of untransformed austenite ($L2_1$) and three different martensite with $L1_0$, $4O$ and $5M$ structures. The relative proportions of four predominant phases are ~ 50, 40, 5 and 5 %, respectively. The $L2_1$ grows under tensile strain on sapphire (0001) substrate and favours the formation of predominantly $L1_0$ over other martensite phases below the transition temperature. The interface between various phases are found to be coherent. The overall magnetization of the thin films is close to the ideal values and local EELS measurement of Mn and Ni $L_{3,2}$ absorption edges confirms the presence of non-magnetic phases in the structure.

This work has been published in the following journals:

***B. Vishal,** U. Bhat, H. Sharona, A. Mukherjee, S. Roy, S. C. Peter, and R. Datta,, Manuscript Under review, Journal of Crystal Growth (2020).*

6.1 Introduction

Magnetic refrigeration plays a vital role in cooling technologies, which is energy-efficient and environmentally benign without greenhouse gas emission [1]. Though various Heusler alloys (HA), e.g., La-Fe-Si, Mn-Fe-P-As, Gd-Si-Ge, Ni-Mn-X (X = Ga, Sn, Sb, In) exhibit giant magnetocaloric effect (MCE) [2-12], however, inverse magnetocaloric effect (iMCE) is important for the refrigeration application. Among many alloy systems, two composition of Ni-Mn-Sn, i.e. $Ni_{50}Mn_{37}Sn_{13}$ and $Ni_{50}Mn_{35}Sn_{15}$ have attracted considerable research attention due to their large iMCE at room temperatures. Entropy change (ΔS) of 18 and 15 $JKg^{-1}K^{-1}$ has been reported for the above two compositions at 299 and 187 K, respectively in bulk polycrystalline samples [5]. In these specimens, the field induced magnetization *M(H)* deviates from the linearity due to short range ferromagnetic interaction at the non-magnetic phase at temperature up to Curie temperature (T_C^A). Martensitic transformation begins at a martensitic start temperature (M_s), below which the magnetization drops. Between $M_f \leq T \leq M_s$, the bending of *M(H)* curve is attributed to non-magnetic component present in the mixture of ferromagnetic austenite and martensite phases probably due to short range anti-ferromagnetic correlation [5, 13]. Such short-range interaction is attributed to the observed giant iMCE which increases configurational entropy through various first order magnetic transformations [14-16]. In Ni-Mn-Sn system, AFM interaction is present between Mn-Mn_{Sn} sites in the martensite lattice [5, 17-21].

The transformation from Austenite to various martensite is correlated with the valence electron to atom ratio (*e/a*) in this system [22, 23]. Moreover, it depends also on the Sn concentration. There are several reports based on X-ray diffraction analysis, HRTEM imaging to identify various martensitic phases and associated transformation temperatures for these two-alloy compositions [24, 25]. From the TEM image, $L2_1$ and $4O$ phases are observed to be present in $Ni_{50}Mn_{37}Sn_{13}$ alloy [25]. With substitution of Mn at Sn site in $Ni_{50}Mn_{37+x}Sn_{13-x}$ (x = 0, 2, 4) raises the martensitic transition temperature (M_s) while it decreases with increasing Mn content for constant Sn level in $Ni_{50-y}Mn_{37+y}Sn_{13}$ (y = 0, 2, 4) [25]. The composition dependence of M_s has been generalized based on (*e*/*a*) ratio and volume of high temperature phase. It was mentioned that the martensitic phases evolve as $4O \rightarrow 10M \rightarrow 14M \rightarrow L1_0$ with increasing M_s. In another report, inter-martensitic phase transformations have been described and for the two alloy compositions under consideration i.e. Sn =13 (*e*/*a* =8.11) and 15 (*e*/*a* =8.04), the transition goes as austenite

$L2_1 \rightarrow 5M$ and subsequently $5M \rightarrow 5M + L1_0$ upon lowering the temperature around 500 K and 150 K, respectively [22]. For the ribbon shaped $Ni_{50}Mn_{37}Sn_{13}$ flake sample, only 7M martensitic phase is observed at 150 K with M_s at 218 K [24].

As already mentioned, that giant iMCE is associated with a large change in entropy. This is further associated with a sharp change in *M vs T* curve which requires the austenitic Curie temperature (T_C^A) to coincide with the martensitic start temperature (M_s) according to Ref. 21. Under this scenario, FM austenite quickly changes to AFM martensite results in sharp drop in temperature dependent magnetization response across the transition temperatures. $Ni_{50}Mn_{37}Sn_{13}$ (e/a = 8.11) is only known alloy composition with both T_C^A and M_s coinciding at room temperature (RT). The magnetic moment contribution in all the austenitic and martensitic phases for the present composition below Curie temperature (T_C^A) is mostly from Mn at the regular lattice site and Ni contributes marginally [Table 1, Ref. 21]. The small magnetic moment of Ni ($< \sim +0.20\ \mu_B$) and Sn ($< \sim -0.08\ \mu_B$) are ferromagnetically and antiferromagnetically coupled with the Mn ($\sim 3.5\ \mu_B$) in the $L2_1$ lattice, respectively [21]. For stoichiometric $Ni_{50}Mn_{25}Sn_{25}$, there is no substitution of Mn at Sn site and the magnetic moment of the alloy is large $4.05\ \mu_B$/f.u. ($L2_1$) [21]. When Mn goes to Sn site which is the case for the present alloy compositions, then Mn at two different sites in the same unit cell are antiferromagnetically coupled leading to reduction in net magnetization i.e. $2.89, 1.86, 0.81\ \mu_B$/f.u. for composition $Ni_2Mn_{1+x}Sn_{1-x}$ (x = 0.25, 0.50, 0.75), respectively [21]. This aspect has been studied both theoretically and experimentally for non-stoichiometric alloy composition [5,13,17-21].

For many practical device applications, thin film form of the alloy is required e.g., in magnetic cooling, actuators, sensors, micro-electromechanical system (MEMS) etc. [26-27]. Growing thin film with right stoichiometry is challenging and transformation kinetics of austenite to martensitic phases may be very different in thin film form compared to its bulk counterpart. In one report, thin film $Ni_{50}Mn_{37}Sn_{13}$ shows formation of $L1_0$, $14M$ and $10M$ martensite phases, whereas $Ni_{51.6}Mn_{34.9}Sn_{13.5}$ shows $4O$ and $10M$ martensitic phases grown by sputtering method [18]. Film thickness has strong influence on martensitic transformation kinetics, transformation temperatures (M_s, M_f), and range of transformation temperature. In this context it was shown that martensitic transformation is restricted near the film-substrate interface leading to residual

austenitic at lower temperature and increase the range of martensitic transformation temperature [28]. The large temperature range of martensitic transformation is useful for wide temperature range MCE application. In another report entropy change of 1.6 $JKg^{-1}K^{-1}$ and 1.5 $JKg^{-1}K^{-1}$ corresponding to cooling and heating, respectively was reported for $Ni_{51.6}Mn_{32.9}Sn_{15.5}$ alloy thin film grown on MgO substrate [29].

In this chapter, thin film of $Ni_{50}Mn_{37/35}Sn_{13/15}$ alloys were deposited on *c*-plane sapphire substrate by pulsed laser deposition (PLD). The Curie temperature (T_C^A) of the films are 316 and 334 K corresponding to Sn = 13 and 15, respectively. The microstructure of the films consists of untransformed austenite $L2_1$ and three different martensite of $L1_0$, $4O$ and $5M$ structures with ~ 50, 40, 5 and 5% volume fractions, respectively. The $L2_1$ grows under tensile strain on sapphire (0001) plane and favours the formation of predominantly $L1_0$ over other martensite phases at transition temperature. The overall magnetization is close to the ideal values and local EELS measurement of Mn and Ni $L_{3,2}$ edge confirms the presence of non-magnetic phases in the structure particularly in $4O$ and $5M$ form of martensite.

6.2 Experimental Methods

$Ni_{50}Mn_{37/35}Sn_{13/15}$ thin films are grown by PLD from the respective target composition. In order to prepare the PLD target, first the ingots corresponding to two different alloy compositions were prepared by arc melting of pure metal Ni (Alfa Aesar 99.99+ %), Mn (Alfa Aesar 99.999+ %) and Sn (Alfa Aesar 99.999+ %) in appropriate proportion in a water-cooled copper crucible and Ar atmosphere. PLD target was then prepared from these ingots after reshaping and polishing to the desired level. Excimer laser (KrF, ~ 248 nm) with 150 mJ energy (~1.5 Jcm^{-1}) energy density at the target was used for ablation. Due to the large lattice mismatch (~10%) we follow three step thin growth reported/developed in our previous work [30-32]. Three step growth schedule is shown in Figure 6.01. The ablation frequency used is 1 Hz/1 Hz during nucleation at T= 400 °C, 1 Hz/1 Hz and 5 Hz/5 Hz during buffer and final growth respectively at T= 600 °C. The slow laser ablation rate allows sufficient time for kinetic relaxation of the nucleation layer to establish epitaxial relationship with the underlying substrate. This also helps in eliminating misaligned crystallites for highly lattice mismatched epitaxy [30-32]. The pressure is kept constant at ~10^{-5} Torr

throughout the growth schedule while the temperature of the growth was 400 and 600 °C for the nucleation and final growth, respectively. For microstructure evaluation, TEM samples were prepared by first mechanical polishing down to 30 µm and then Ar ion milling to perforation to generate large electron transparent thin area. Stoichiometry of thin films were characterized by energy dispersive spectroscopy (EDS).

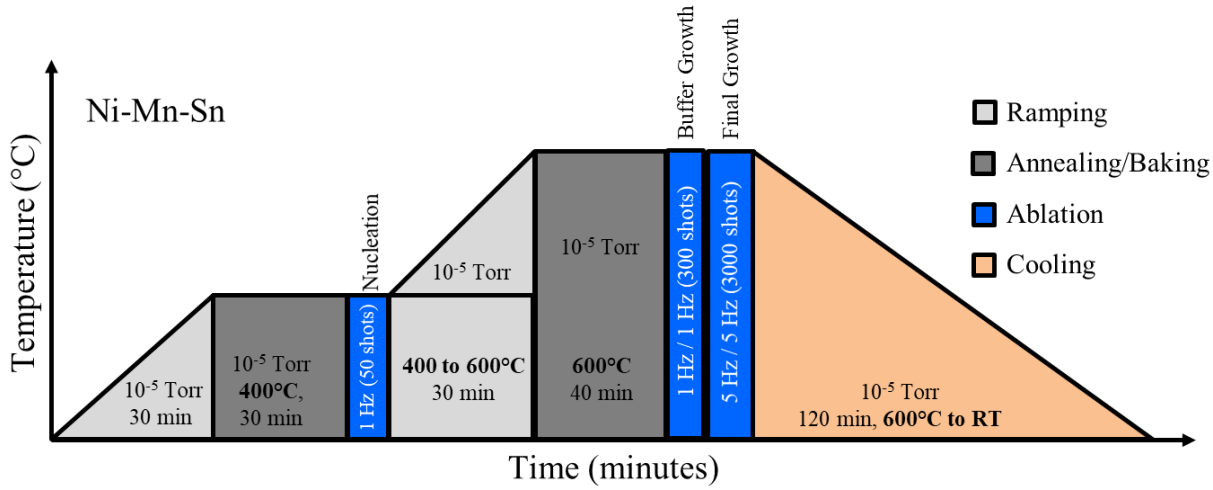

Figure 6.01. *The growth scheme for Ni-Mn-Sn Heusler alloys thin film by PLD.*

All the imaging and Electron energy loss spectroscopy (EELS) were performed in a FEI TITAN 80-300 kV aberration corrected transmission electron microscope equipped with a gun monochromator having energy resolution better than 180 meV. The fine features at Ni and Mn L_3 edge corresponding to onset of absorption at 855 and 640 eV, respectively were recorded for analysing presence of any non-magnetic phases in the microstructure. During EELS spectra acquisition a parallel illumination technique with nano scale resolution was used developed earlier [33-34]. Thin film of dimension 4×3 mm^2 was used for magnetic measurement in a superconducting quantum interference device (SQUID), VSM, Quantum Design, USA. Field Cooled (FC) and Zero Field Cooled (ZFC) measurements were carried out from 390 K to 2 K with cooling rate of 2 K/min.

6.3 Computational Techniques

The first principle calculation of the density of states (DOS) and EELS spectra of different phases corresponding to $Ni_{50}Mn_{37.5}Sn_{12.5}$ alloy composition was carried out using full potential augmented plane waves and local orbital basis set as implemented within WEIN2k code [35, 36]. The calculations were performed by generalized gradient approximation (GGA) under Perdew-Burke-Ernzerhof (PBE) exchange correlation functional with energy, charge and force convergence criteria below 0.0001 Ry, 0.001 e and 1m Ry/au, respectively [36]. The Muffin Tin radii (R_{MT}) was chosen such that to avoid overlap between atoms. The K_{max} value for plane wave basis was $8.00/R_{MT}$ (min) (R_{MT} (min) is the Muffin tin radius of the smallest atom). The crystal structures corresponding to $L2_1$, $L1_0$, $4O$ and $5M$ phases were constructed. The optimizes lattice parameters are (*i*) a = 5.78 Å for $L2_1$, (*ii*) $a = b$ = 3.74 , c = 6.86 Å for $L1_0$, (*iii*) a = 4.35, b = 5.29, c = 8.42 Å with $\delta = 0.062$ for $4O$, and (*iv*) a = 4.11 , b = 5.67 , c = 10.43 Å with $\delta = 0.050$ for $5M$. A 10×10×10 *k*-mesh was used per stoichiometric unit cell of $L2_1$ and is reduced proportionally for $L1_0$, $4O$ and $5M$ phases. For magnetic calculation, spin orbit coupling is considered and magnetization of the lattice is oriented along <001> direction with individual atomic spin orientations as Ni (up), Mn (up), Mn_{Sn} (dn), Sn (dn) [21, 37]. To explain the marginal discrepancy between the observed magnetic moment and theoretical values, non-magnetic calculation is also performed for all the different phases. Electron loss near edge spectra (ELNES) corresponding to Ni and Mn L_3 edge is simulated using TELNENS3 program as implemented within WEIN2k code [38, 39]. The magnetic structure of materials by EELS spectra has already been used extensively [33, 34].

6.4 Results and Discussion

6.4.1 Microstructural details of HA thin films

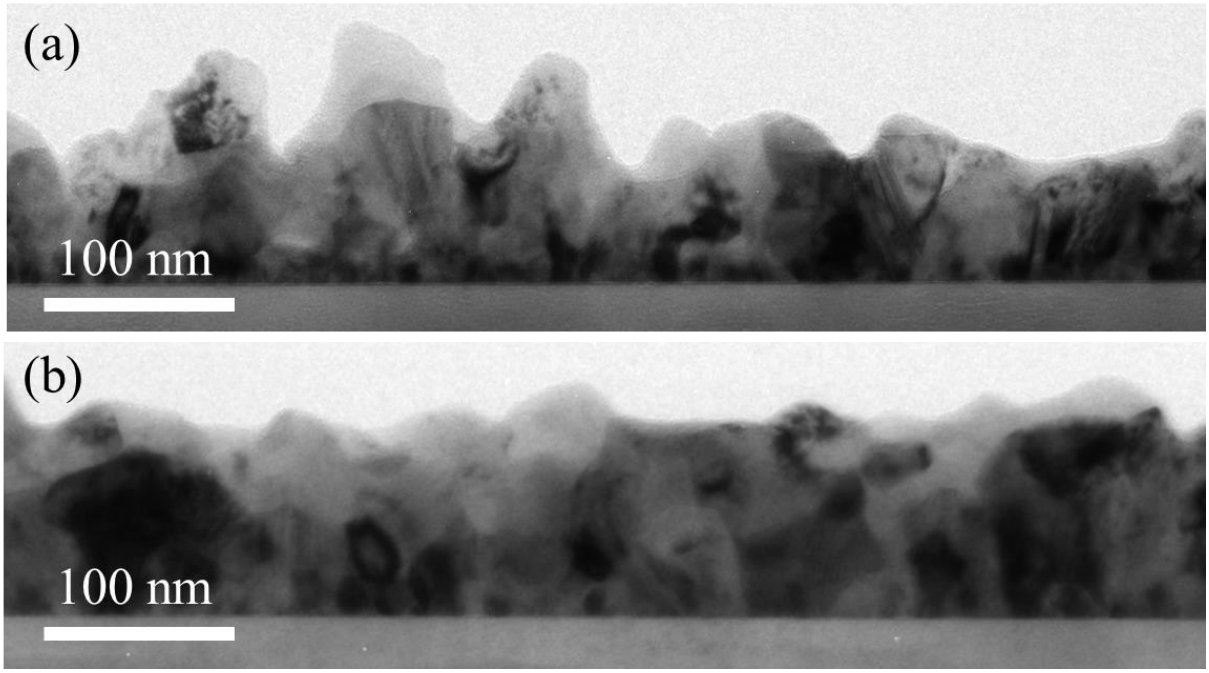

Figure 6.02. *(a) & (b) are the bright field TEM image of $Ni_{50}Mn_{37}Sn_{13}$ and $Ni_{50}Mn_{35}Sn_{15}$ Heusler alloy with two different Mn and Sn concentrations.*

Figure 6.02. (a) & (b) are the low magnification bright field TEM image of $Ni_{50}Mn_{37}Sn_{13}$ (film X) and $Ni_{50}Mn_{35}Sn_{15}$ (film Y) Heusler alloy thin films grown on *c*-plane sapphire substrate. The thickness of the films is ~ 100 nm and the surface is rough. The rough surface morphology is due to various structural phase transitions while cooling down from the deposition temperature (600 °C) to room temperature (RT). Figure 6.03. is the example HRTEM image showing various structural phases present in film X at RT. And Figure 6.04. for HRTEM images for film Y ($Ni_{50}Mn_{35}Sn_{15}$) which is similar to film X. The microstructure of films at RT shows untransformed austenite ($L2_1$) along with three different martensitic ($L1_0$, $4O$ and $5M$) phases which are indicated in the HRTEM images. From the image analysis the volume fractions of different phases are found to be ~50, 40, 5 and 5 % for $L2_1$, $L1_0$, $4O$ and $5M$, respectively.

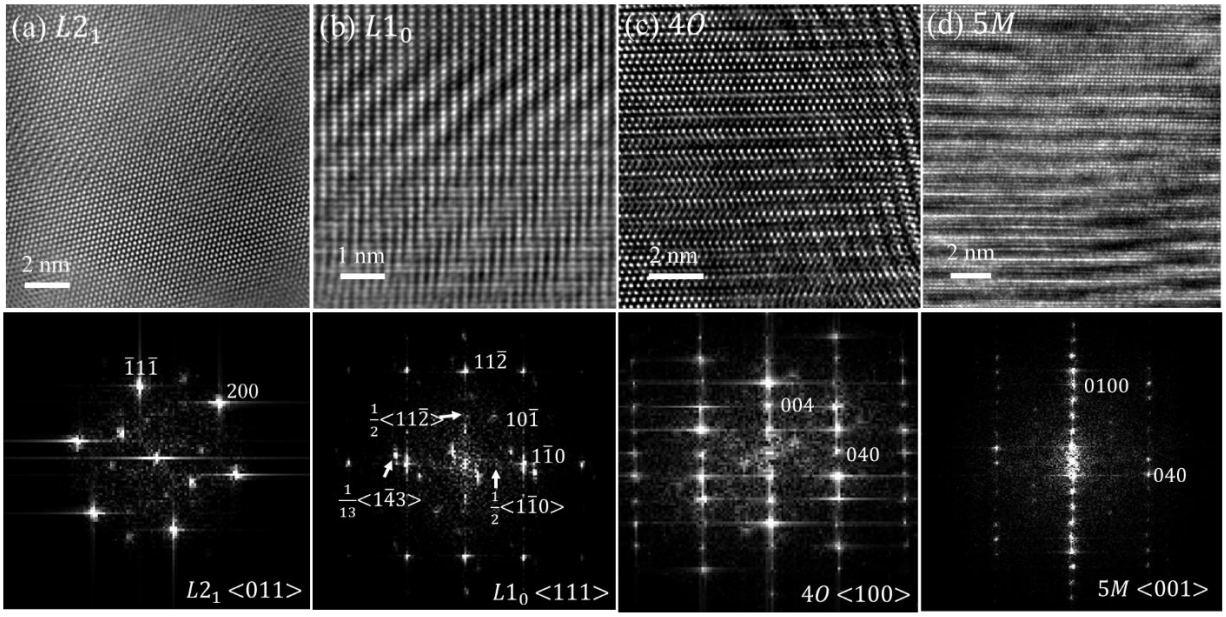

***Figure 6.03**. HRTEM images of $Ni_{50}Mn_{37}Sn_{13}$ film showing various structural phases: (a) untransformed austenite ($L2_1$), and three different martensites (b) $L1_0$, (c) 4O and (d) 5M.*

The dominant (40%) martensitic phase is fully transformed tetragonal $L1_0$ with *c*/*a* ratio of 0.917. Volume fraction of different phases are found to be almost same in both X and Y thin films. HRTEM images and local FFT pattern from different phases are also given in Figure 6.03. The experimental lattice parameter of different phases obtained from HRTEM images are summarized in Table 1. Comparable lattice parameter from literature confirms the targeted stoichiometry has been achieved by PLD. For film X, the cell volume decreases by 0.70, 0.24, and 0.46 % for $L1_0$, $4O$, $5M$, respectively with respect to $L2_1$. Film Y shows decrees in cell volume by 0.41, 0.67, and 0.67 % for $L1_0$, $4O$, $5M$, respectively.

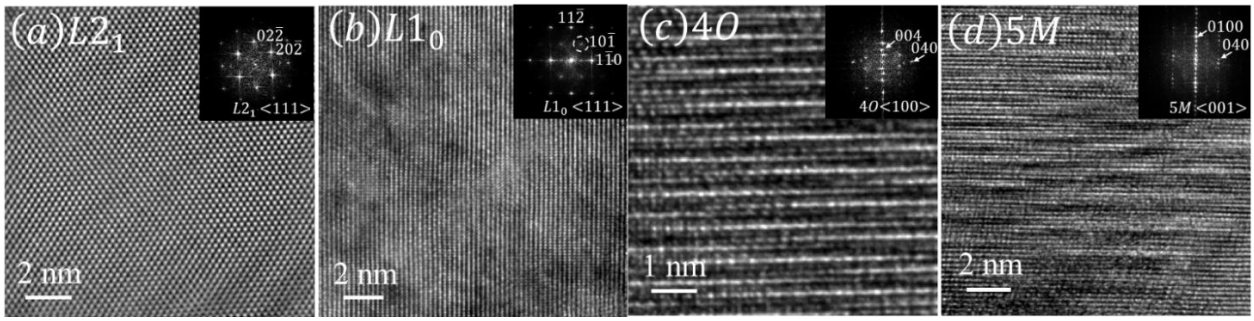

***Figure 6.04**. HRTEM images of $Ni_{50}Mn_{35}Sn_{15}$ film showing various structural phases: (a) untransformed austenite ($L2_1$), and three different martensites (b) $L1_0$, (c) 4O and (d) 5M.*

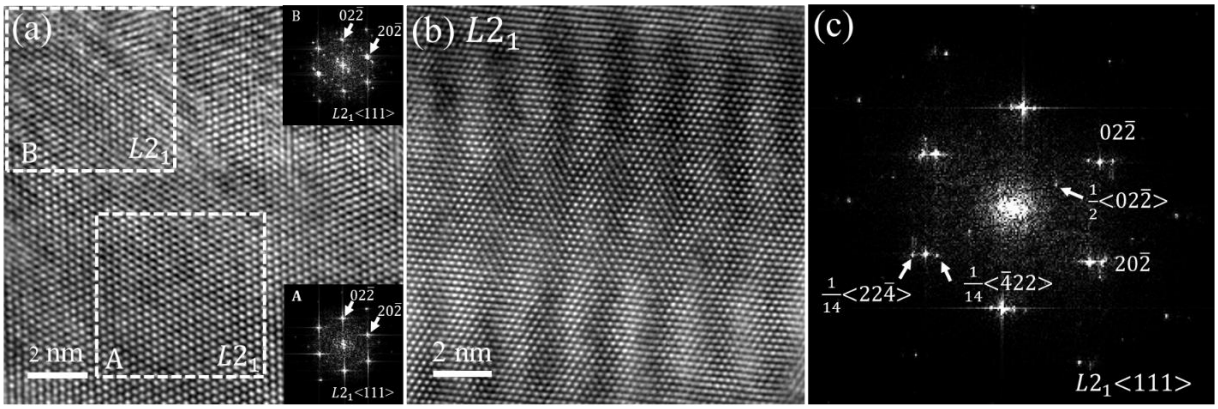

Figure 6.05*. (a) Example HRTEM image of austenitic regions containing both modulated and unmodulated areas. (b) & (c) are the FFT image from the unmodulated and modulated areas, respectively.*

Figure 6.05.(a) is the HRTEM image from an $L2_1$austenitic phase with two different appearance; modulated and unmodulated regions as marked by A and B. The FFT of modulated and unmodulated areas are given in the inset corresponding to area A and B. In the modulated region two different superlattice spots corresponding to 1/14<$22\bar{4}$> and ½<$02\bar{2}$> are observed, [Figure 6.05.(b) & (c)]. These are from partially transformed $14M$ and $2M$ martensitic phases coherent with the $L2_1$ matrix. This is also reflecting in the FFT pattern in terms of absence of any additional spots. Almost similar volume fractions of both modulated and unmodulated areas are observed. This means 50% of total $L2_1$ phase consist of coherent $14M$ and $2M$ phases which appears as modulated $L2_1$ phase in the electron micrograph.

The observation of $14M$ phases suggest that local Sn composition may be depleted in the parent $L2_1$ during crystal growth and cooling which influenced this martensite phase transformation. It is reported that if Sn composition drops from *x* = 15 to 13 with corresponding increase in *e*/*a* ratio from 8.04 to 8.11 stabilizes the $7M$ over $5M$ phase or in other words modulation vector increases [22].

Figure 6.06.(a) & (b) are the HRTEM images of $L2_1$ phase showing twin and stacking fault, respectively. The mirror plane of the twin boundary is $(\bar{2}20)$. Ferromagnetic shape memory alloys (SMA) which exhibit coupling between magnetic and structural order involving motion of twin boundaries results in a large magnetic field induced strain [19].

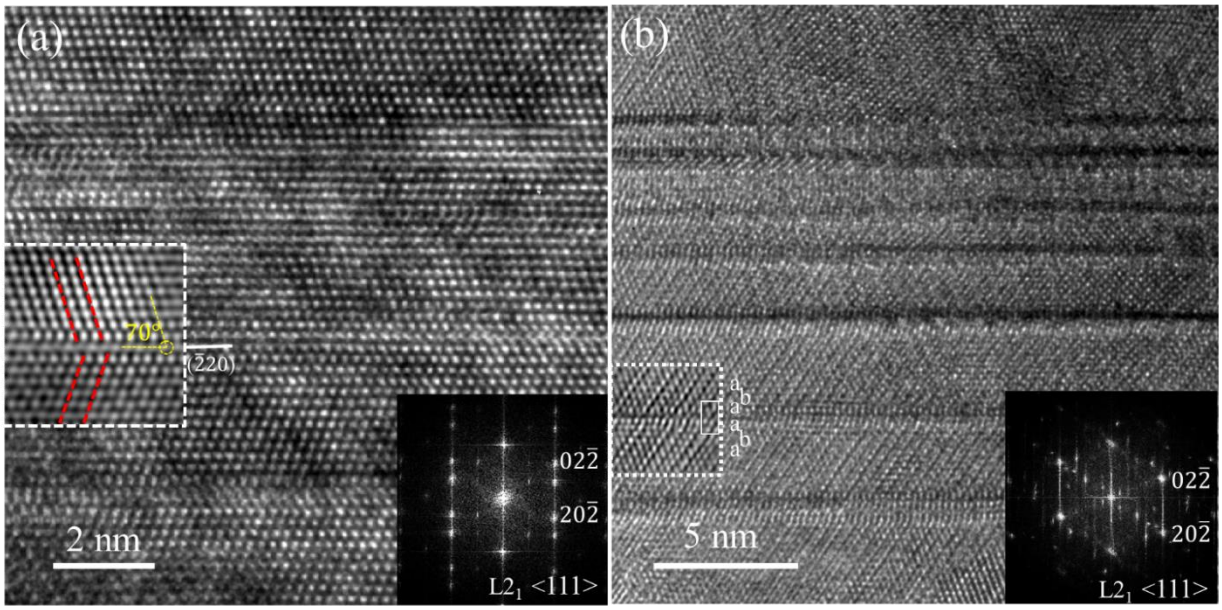

Figure 6.06. *HRTEM image of $L2_1$ phase containing (a) twin and (b) stacking fault boundaries.*

The twinning increases the strength of the AFM exchange interaction by altering the Mn-Mn_{Sn} interatomic spacing [19]. Grain boundaries and defect in shape memory alloys are generally contributing towards the irreversibility during structural transformation [40]. Large grain boundary population affects the transformation range and cause large magnetic hysteresis [41].

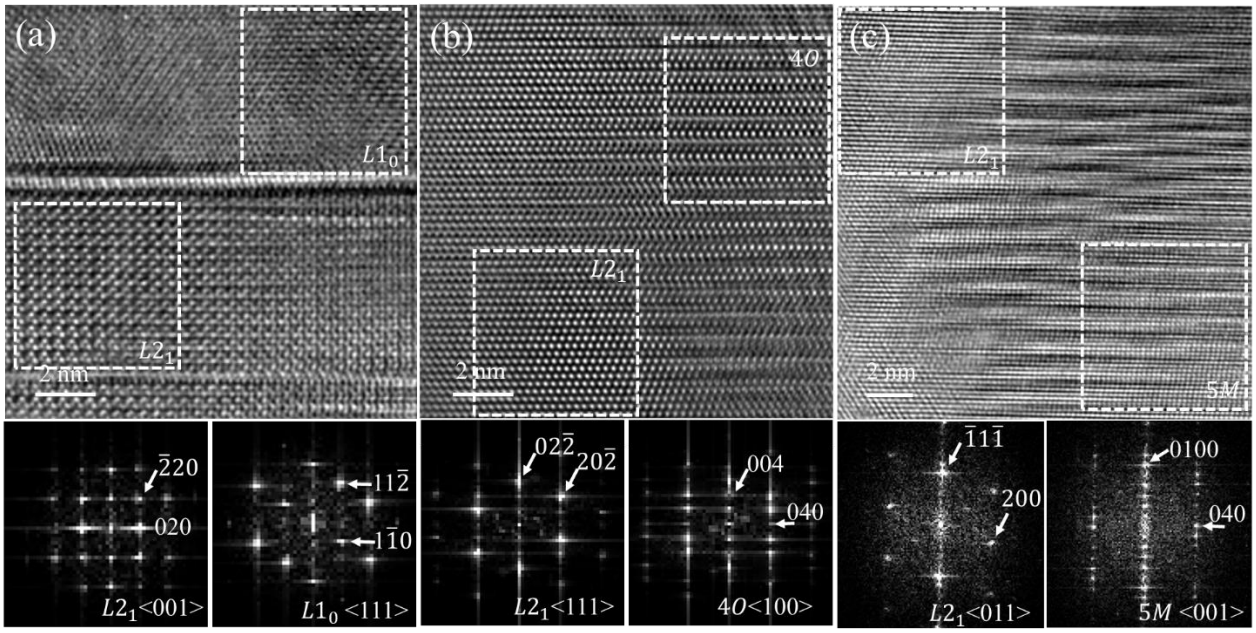

Figure 6.07. *HRTEM image of Interface between $L2_1$ and three different martensite; (a)-(c) $L1_0$, $4O$ and $5M$.*

Figure 6.07.(a) to (c) show interface boundary between untransformed $L2_1$ and three different martensites; $L1_0$, $4O$ and $5M$, respectively. Local FFT pattern from the interface shows no separate spots from two different phases. This suggests that the interface is coherent, and all the martensitic phases are strained. Two types of interfaces are observed between $L2_1$ to $L1_0$: interface containing stacking fault and coherent boundary [Figure 6.07. and Figure 6.08.]. The orientation relationship between the $L2_1$ and $L1_0$ is $L2_1$ <001> ∥ $L1_0$<111>. The austenite in Figure 6.07.(a) has modulation in the structure due to partially transformed $14M$ and $2M$ martensite as already described in Figure 6.05.(c) and Figure 6.07.(b) & (c) show the HRTEM images of the interface between $L2_1$ with $4O$ and $5M$, respectively. Corresponding FFT pattern gives the orientation relationship as $L2_1$ $\{02\bar{2}\}$ ∥ $4O$ {004}, $L2_1$ <111> ∥ <001> $4O$ and $L2_1$ <011> ∥ $5M$ <001>, which is similar to the previous report [42].

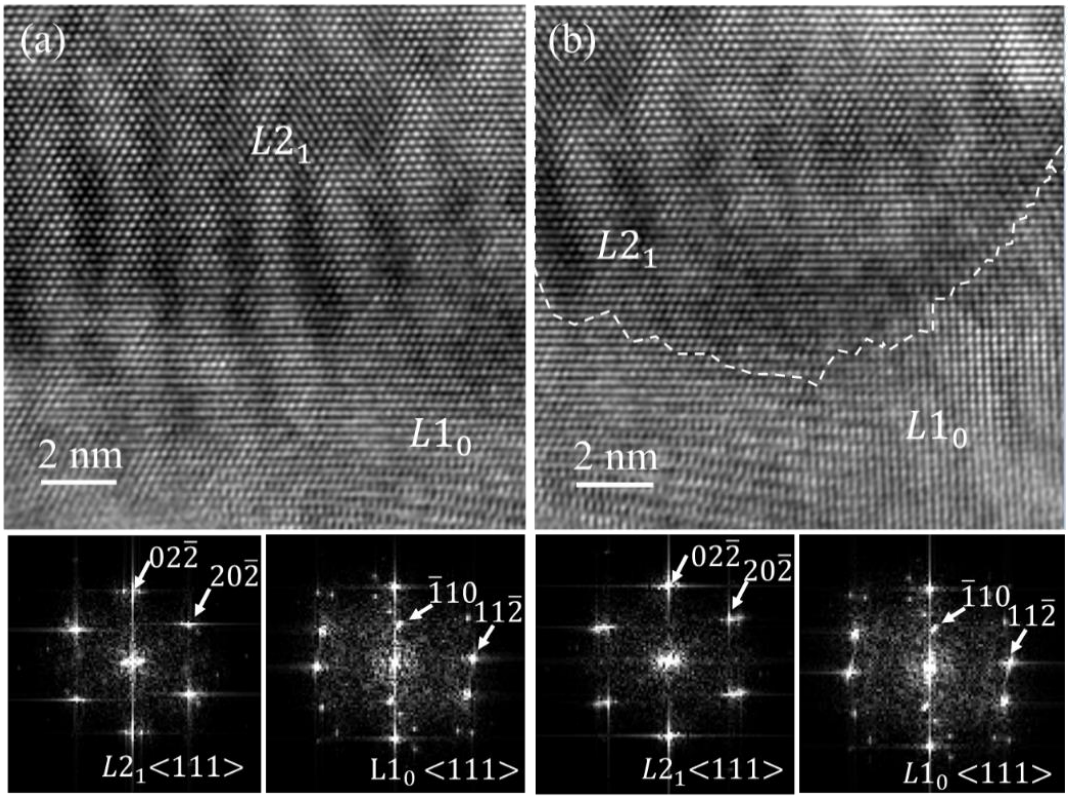

Figure 6.08*. HRTEM image of Interface between $L2_1$ to $L1_0$: interface containing coherent boundary with (a) Modulated $L2_1$ and (b) Un-modulated $L2_1$.*

Figure 6.09.(a)-(c) are the HRTEM image and corresponding FFT patterns of $L2_1$ and sapphire substrate along <$01\bar{1}0$> Z.A. of Al_2O_3. The epitaxial relationship is found to be α-Al_2O_3 [$01\bar{1}0$] ∥

$L2_1$ [011]. The lattice parameter mismatch between $L2_1$ austenite and substrate is 10% [between (111) plane of $L2_1$ and (0002) plane of sapphire]. The schematic in-plane epitaxial relationship between $L2_1$and sapphires is shown in Figure 6.09.(d).

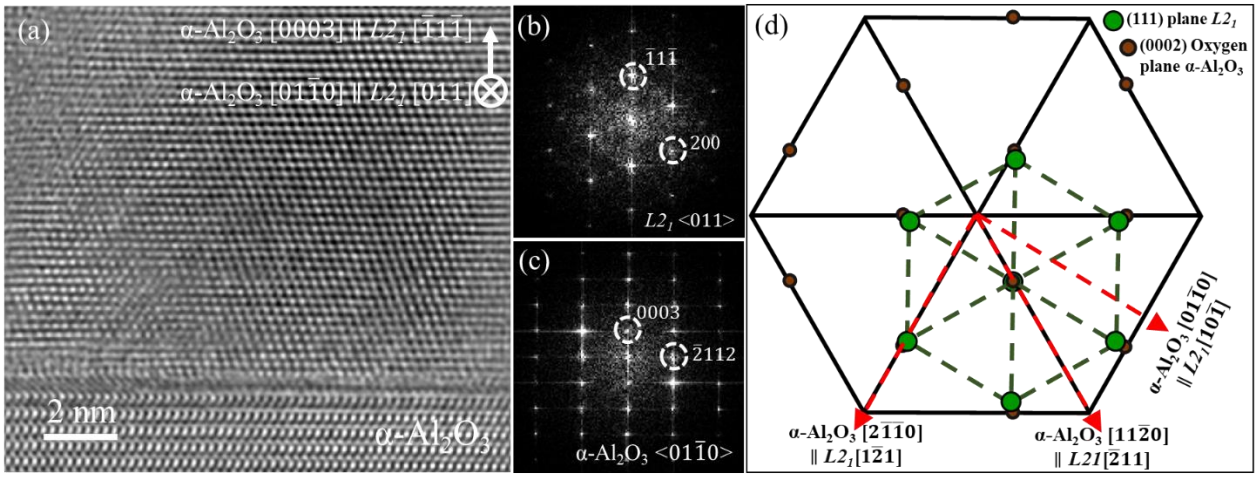

***Figure 6.09**. (a) HRTEM image of $Ni_{50}Mn_{37}Sn_{13}$ thin film on c-plane sapphire substrate along $< 01\bar{1}0 >$ Z.A. with corresponding FFT from (b)Film and (c) substrate .Epitaxial relationship between sapphire and $Ni_{50}Mn_{37}Sn_{13}$ is α-Al_2O_3 $[01\bar{1}0] \parallel L2_1\,[011]$ (d) Schematic showing in-plane epitaxial relationship.*

HRTEM image of the film-substrate interface is shown Figure 6.10. It is found that $L2_1$ phase is retained predominantly near the interface and $L1_0$ near the surface. Few layers of retained $L2_1$ is always observed between the sapphire substrate and $L1_0$ phase [Figure 6.10. Area F]. Transformation of $L1_0$ is responsible for the film roughness. Unmodulated and untransformed remnant $L2_1$ is marked as Area C and F near interface. Which is further transformed into modulated $L2_1$ as thickness increases is marked as Area D and E.

Lattice mismatch and film thickness plays important role on the martensitic phase transition kinetics [28,43-44]. Phase transformation from austenite to martensite is suppressed close to the film-substrate interface due to strain induced by lattice mismatch. Large lattice mismatch can suppress martensitic transformation due to formation of high destiny of misfit dislocations [28].

In case of epitaxial Ni-Mn-Ga film grown on MgO substrate a thin untransformed austenite film remains at the substrate film interface [43]. Moreover, increase in transition temperature (M_S) is attributed to stress induced by the lattice mismatch [44]. For Ni-Mn-Sn film grown on MgO, the

lattice mismatch is 0.7 % and shows both untransformed austenite and increase in the transition temperature. [45].

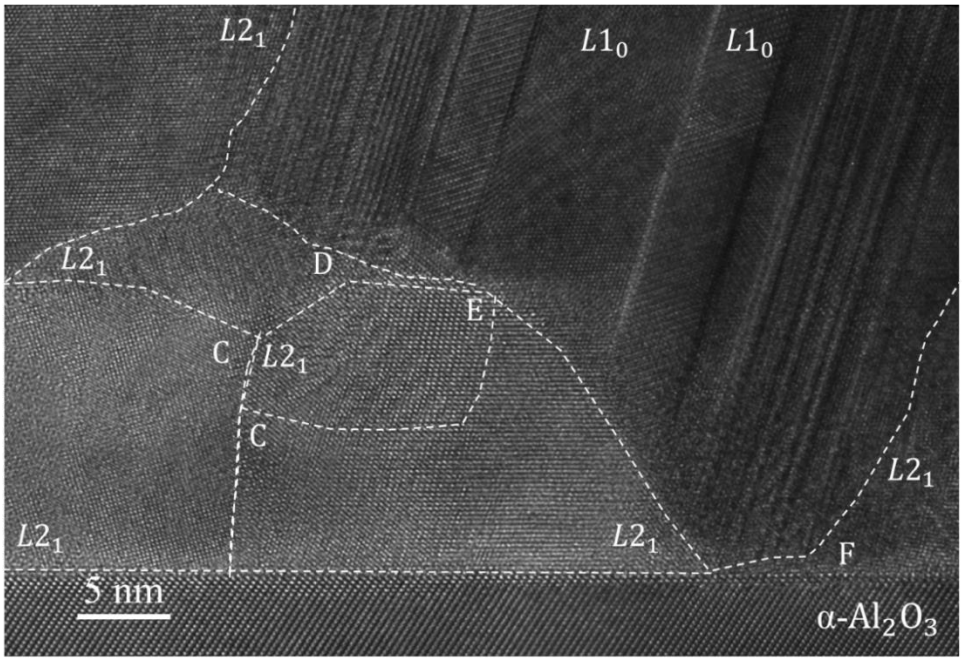

Figure 6.10. *HRTEM image near the surface and film-substrate interface of the film. Showing predominantly* $L2_1$ *phase near the interface and* $L1_0$ *near the surface.* $L1_0$ *is responsible for making the film rough.*

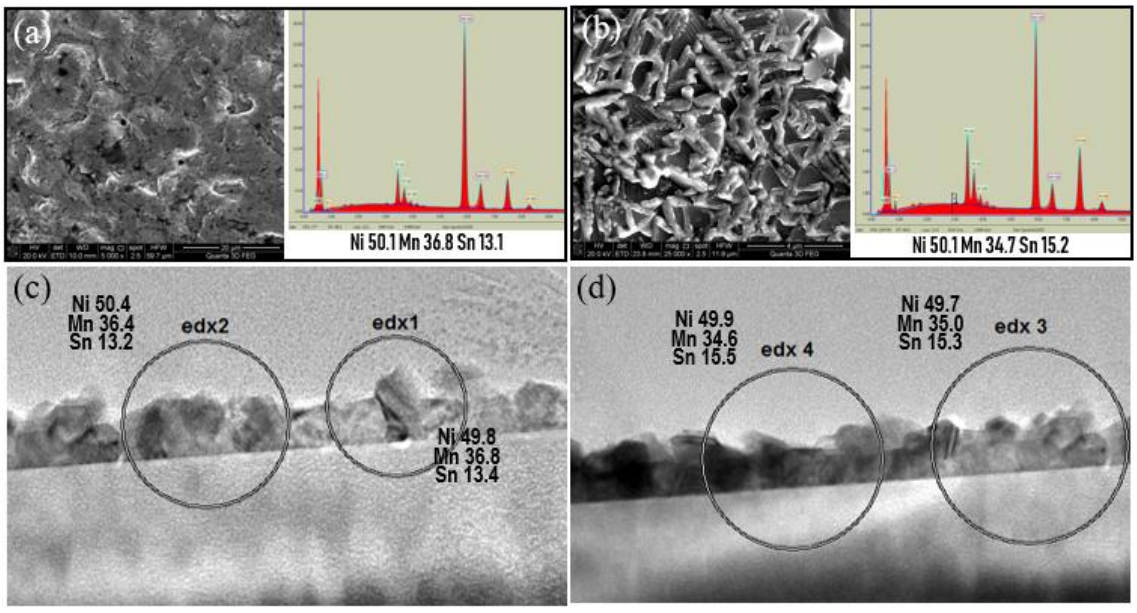

Figure 6.11. *SEM image and corresponding EDS of Heusler alloy ingot with target composition of (a)* $Ni_{50}Mn_{37}Sn_{13}$ *(b)* $Ni_{50}Mn_{35}Sn_{15}$*, similar composition was measured for thin films using TEM EDS for (c)* $Ni_{50}Mn_{37}Sn_{13}$ *(d)* $Ni_{50}Mn_{35}Sn_{15}$ *compositions, respectively.*

In the present case the lattice mismatch is large i.e. 10 % which is the reason behind high volume fraction (~25 %) of retained$L2_1$. Modulated/commensurate $L2_1$ majorly occur little away from substrate interface [Figure 6.10. Mark as Area D and E]. Modulated/commensurate $L2_1$ are converting towards $2M$ and $14M$ are possibly caused during lattice strain relaxation or/and/while during cooling [Figure 6.05.(b) & (c)]. Untransformed $L2_1$ due to lattice strain/ mismatch is responsible for no sharp change in M vs T (100-200K) in alloy A and B (Figure 6.10.(b) & (c)) causing no positive change in entropy hence iMCE, as it reported in Krenke *et al.* and E. Yüzüak *et al.* for the composition [5,29]. Untransformed $L2_1$ due to lattice strain/ mismatch is responsible for no sharp change in M *vs* T (100-200K) in alloy A and B [Figure 6.12.(a) & (b). Causing no positive change in entropy hence iMCE, as it reported in Krenke et al. and APL for the composition [5,29]. Almost same composition is obtained between the target pellet and thin films as examined by SEM and TEM EDS, respectively [Figure 6.11.]. Suggests there are little fluctuation in *e/a* ratio, which makes the possibility of observation some phases show presence of magnetic or non-magnetic in nature observed at RT, the details magnetic study is done in section **6.4.3** with help of density functional theory (DFT) TELNENS3 and experimental EELS spectra.

6.4.2 Magnetic study of HA thin films

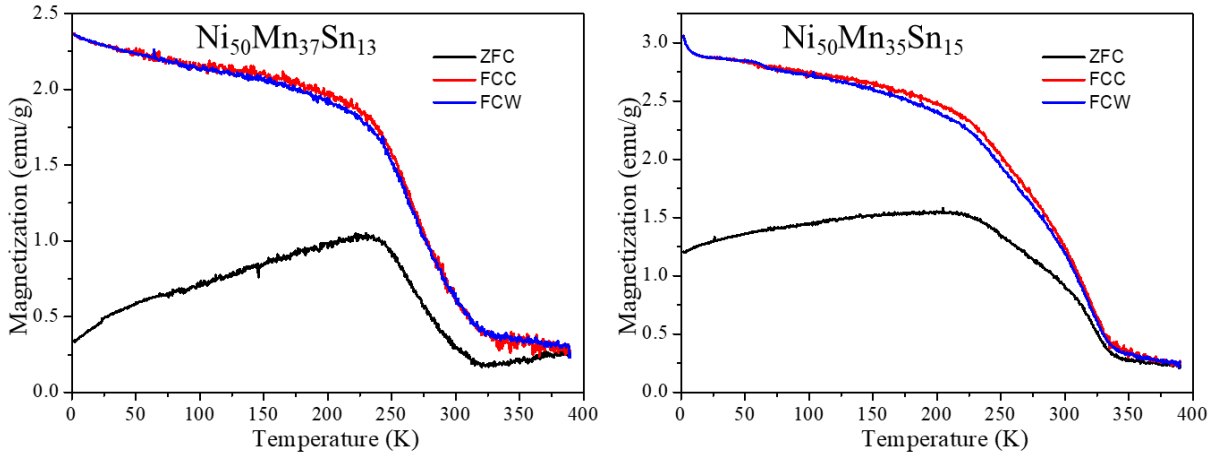

Figure 6.12. *(a) & (b) are ZFC, FC and FW plots for (a) $Ni_{50}Mn_{37}Sn_{13}$ and (b) $Ni_{50}Mn_{35}Sn_{15}$ alloys.*

The magnetization *vs* temperature (M *vs* T) under zero field cool (ZFC), field cool (FC) and field heating (FH) of two different alloys are given in Figure 6.12.. The applied field was 50

Oe for FC measurement. The curie temperature (T_C^A) of austenite is 316 and 334 K for $Ni_{50}Mn_{37}Sn_{13}$ (alloy X) and $Ni_{50}Mn_{35}Sn_{15}$ (alloy Y, respectively. A separate martensitic curie temperature (T_C^M) is observed for alloy B at 260 K. There is drop and increase on the magnetization at lower temperature for ZFC and FC curves, respectively. Near absolute zero there is increase in magnetization in FC curve for both alloys and this feature is generally attributed to para-Magnetic Curie tail and suggests that the samples have both ferromagnetic and paramagnetic phases [46]. Splitting between ZFC and FC curves indicates that the sample is magnetically inhomogeneous and is observed in similar HA alloys Ni–Mn–X (X = Sn, Sb, In) [10,11,24]. Reduction in magnetization with decreasing temperature (230 to 0 K) in ZFC curve for both alloys maybe because of continuous progress in the growth of martensitic phases and their antiferromagnetic coupling with surrounding untransformed $L2_1$ phases. The situation reverses for FC curve due to the application of field which orients all the magnetic phases along same direction.

Table 1. The experimental lattice parameter of different phases obtained from HRTEM images of both Film X (Sn = 13) and Y (for Sn = 15).

Phases	Experimental lattice constants (for Sn 13)	Experimental lattice constants (for Sn 15)
$L2_1$	$a = b = c$ = 0.597 nm	$a = b = c$ = 0.602 nm
$L1_0$	$a = b$ = 0.386 nm c = 0.709 nm ΔV = -0.70 %	$a = b$ = 0.392 nm c = 0.707 nm ΔV = -0.41 %
$4O$	a = 0.443 b = 0.552, c = 0.868 nm ΔV = -0.24 %	a = 0.448 b = 0.556, c = 0.870 nm ΔV = -0.67 %
$5M$	a = 0.428 b = 0.568 nm c = 1.089 nm ΔV = -0.46 %	a = 0.432 b = 0.573 nm c = 1.094 nm ΔV = -0.69 %

In present case the M vs T is similar to the report in Ref. 28. The experimentally observed magnetization below T_C^A is comparable but marginally smaller to the theoretical values. The experimental magnetization values of thin films are also comparable with the literature [29]. Ideal and experimental determine values are summarized in Table 2. There is an increase in magnetization in system from FC to ZFC curve bellow T_C^A. This suggests that either there is a presence of non-mag phases or interfaces between various phases have AFM coupling at random orientations.

Table 2. Theoretical values of different phases for $Ni_2Mn_{1.5}Sn_{0.5}$ ($Ni_{50}Mn_{37.5}Sn_{12.5}$).

Structure	Total magnetic moment (μ_B/f.u.) $Ni_2Mn_{1.5}Sn_{0.5}$	Total magnetic moment (Theo.) $Ni_2Mn_{1.5}Sn_{0.5}$ (emu/g)	Mn (near + away) μ_B	Mn_{Sn}	Ni	Cohesive energy eV/atom magnetic	Cohesive energy eV/atom Non-magnetic
$L2_1$	1.80	3.883	3.24+2.97=6.21	-3.34	0.11	4.691	3.887
$L1_0$	1.58	3.399	3.38+3.09=6.47	-3.26	0.07	4.681	3.488
$4O$	2.03	4.375	3.03+2.98=6.01	-3.02	0.20	4.486	3.748
$5M$	1.88	4.050	3.14+3.04=6.18	-3.25	0.19	4.226	2.935

6.4.3 Magnetic study by EELS and DFT

HREELS experiment and first principle calculation of EELS spectra were carried out to ascertain the presence of any non-magnetic phases in the austenite and various martensitic phases.

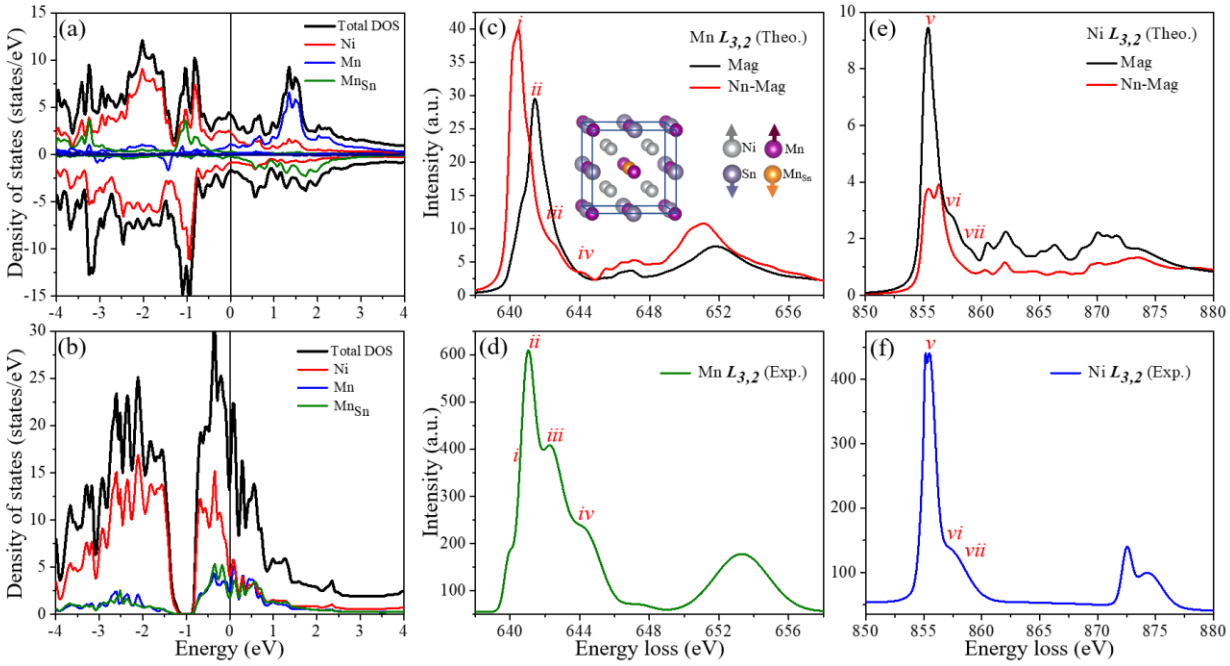

Figure 6.13. *(a) & (b) DOS from various Mn locations in the lattice regular and Sn sites configurations from magnetic and non-magnetic configurations for $L2_1$. (c) Calculated EELS spectra for total Mn for magnetic and non-magnetic lattice. (d) Experimental $L_{3,2}$ spectra, (e) & (f) are the calculated and experimental EELS spectra of Ni, respectively.*

Figure 6.13. (a) is the DOS of various Mn in the lattice i.e., Mn at regular lattice site and Mn at the Sn site (Mn_{Sn}) in $L2_1$ lattice for two different spin configurations; Mn at regular site and Mn at Sn site which are coupled anti-ferromagnetically and non-magnetic configurations.

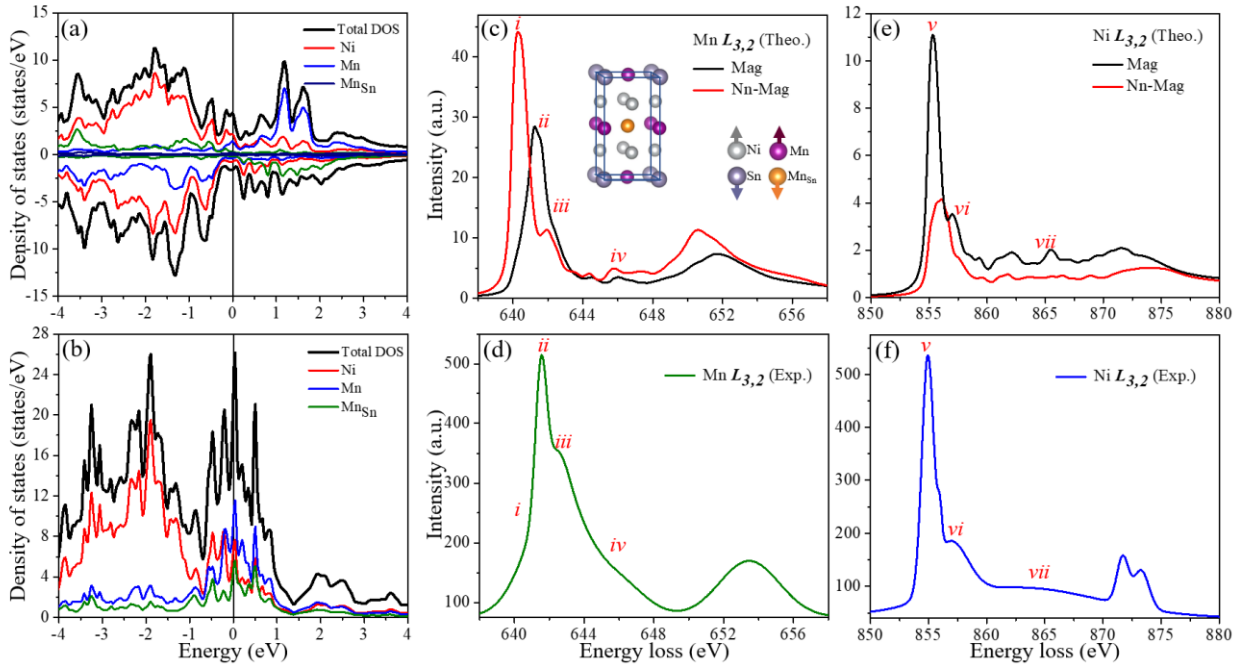

Figure 6.14. *(a) & (b) DOS from various Mn locations in the lattice regular and Sn sites configurations from magnetic and non-magnetic configurations for* $L1_0$. *(c) Calculated EELS spectra for total Mn for magnetic and non-magnetic lattice. (d) Experimental* $L_{3,2}$ *spectra, (e) & (f) are the calculated and experimental EELS spectra of Ni, respectively.*

Mn atoms at the regular sites in the lattice are ferromagnetically aligned. The total Mn moment at the regular site (effective number 2) and Sn site (effective number 1) is 6. 47 and 3.33 μ_B, respectively. Above the Fermi level (E_f), the Mn_{Sn} 3d (d_{xy}, d_{yz}, d_{zx}) unoccupied DOS distributes over broad energy range compared to Mn DOS at the regular site [47]. In case of non-magnetic calculation, all the Mn unoccupied DOS shifts towards the E_f [Figure 6.13.(b).]. The simulated EELS spectra due to the different Mn locations and configurations in the lattice are shown in Figure 6.13.(c). Experimental Mn $L_{3,2}$ is shown in Figure 6.13.(d) and three major peaks are marked in the L_3 part of the spectra. The origin of the peaks can be understood by taking help from simulation results and the peaks '*i*' can be assigned to Mn in the lattice with non-magnetic interactions with other magnetic ions, peak '*ii*' and '*iii*' are due to Mn in the magnetic lattice and

corresponding to FM and AFM alignment, respectively. The Ni in the lattice is ferromagnetically aligned with Mn atoms at the regular site and antiferromagnetically at the Sn site. The total moment contributed by Ni is 0.12 μ_B and is extremely small compared to Mn. This is also reflected in the calculated EELS spectra of Ni in the non-magnetic lattice where no difference is observed in terms of additional peaks [Figure 6.13.(e)]. Figure 6.13. (f) is the experimental EELS spectra of Ni in agreement with the simulated spectra. The details of simulated and experimental EELS spectra for $L1_0$ martensite is given in Figure 6.14.. FM $L2_1$ have large splitting in Mn DOS compared to FM $L1_0$ above E_f. The total moment contributed by Ni in FM $L1_0$ is 0.07 μ_B. In the above two phases peak *'i'* is almost absent in experimental EELS spectra suggesting any significant presence of non-magnetic phases. However, in case of $4O$ and $5M$ martensite phases, pre edge peak *'i'* is clearly visible in the experimental spectra [Figure 6.15.and Figure 6.16.].

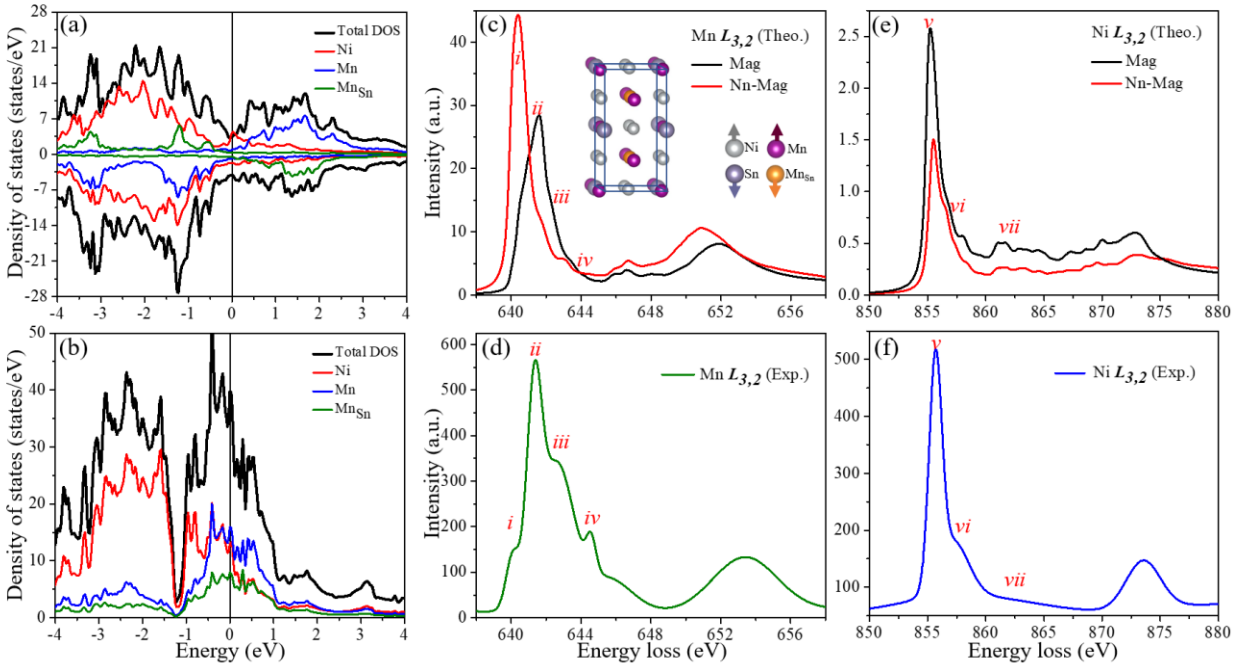

Figure 6.15. *(a) & (b) DOS from various Mn locations in the lattice regular and Sn sites configurations from magnetic and non-magnetic configurations for $4O$. (c) Calculated EELS spectra for total Mn for magnetic and non-magnetic lattice. (d) Experimental Mn $L_{3,2}$ spectra, (e) & (f) are the calculated and experimental EELS spectra of Ni, respectively.*

This suggests that there are significant non-magnetic phases present for these two types of martensite. This is probably due to the lower Curie temperature for these two types of martensite .$L1_0$ Mn DOS shifted above E_f, and causes the relatively higher non-magnetic contribution in $L1_0$, and appear as peak '*i'* in Figure 6.14.(d) . as the magnetic peak '*ii'* and '*iii'* is dominating in experimental EELS spectra, but non-magnetic peak '*i'* is significantly reduce indicating lesser non-magnetic of $L1_0$. It is because $L1_0$ found between 8.025 < *e/a* < 8.150 are FM in nature, which is closer to our targeted composition *e/a* = 8.11 (x = 0.13). And non-magnetic $L1_0$ is observed at 8.25 < *e/a* < 8.50 (mark as area 'X', 'Y' respectably in phase diagram of [Figure 6.17.(a)].

$4O$ is most common martensite observed in bulk for x = 13 (e/a= 8.11), it have strongest Mn-Mn_{Sn} AFM among all martensite [22,25] [Figure 6.17.(b)]. Similar to $L1_0$, non-magnetic DOS of Mn/Mn_{Sn} is more above E_f , and appear as non-magnetic peak '*i'* in Figure 6.15.(d). $4O$ magnetic peak '*ii'* and '*iii'* is dominating in experimental EELS spectra, but non-magnetic peak '*i'* is significantly reduce indicating lesser non-magnetic of $4O$ in Figure 6.15.(d). FM $4O$ is also responsible for absence of magnetization drop/slop in M *vs* T in vicinity of RT, and leads to absence of inverse MCE as it observed in bulk for x = 13 composition [Figure 6.12. (a)].

$5M$ is common martensite observed in bulk for (approx. 8.00 < *e/a* < 8.25) and various temperature range [Figure 6.17.] [22-25]. In case of non-magnetic $5M$ [Figure 6.16.(b)], all Mn unoccupied DOS are at and above E_f, resulting higher non-magnetic peak '*i'* in EELS spectra. $5M$ peak '*i'* corresponds to non-magnetic is dominating in experimental EELS spectra, and magnetic peak '*ii'* and '*iii'* is relatively reduce compare to other martensitic phase in [Figure 6.16.(d)]. Indicating the equal presence of para and ferro-magnetic 5M phase. As shown in phase diagram [Figure 6.17.(a)], at RT (300 K) for *e/a* = 8.11 (x= 13), $5M$ can be non-magnetic (mark as area Z and 'red arrow' in Figure 6.17.(a)), where $5M$ is converted from $L2_1$ during cooling/growth from high temperature.

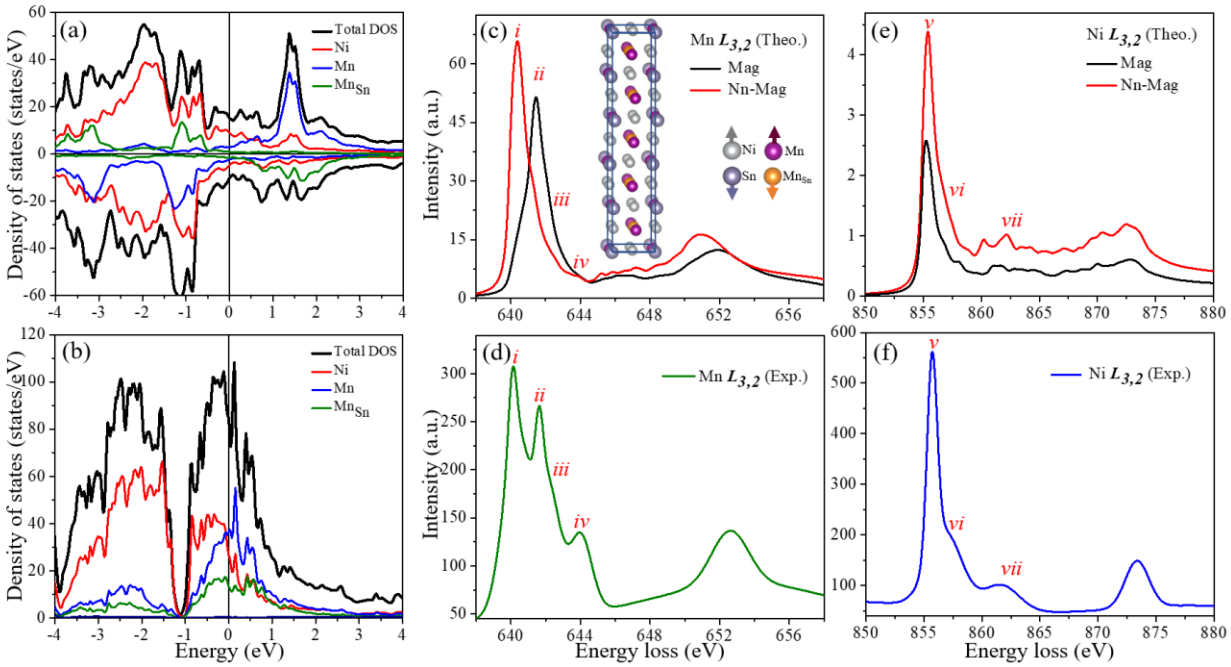

Figure 6.16. *(a) & (b) DOS from various Mn locations in the lattice regular and Sn sites configurations from magnetic and non-magnetic configurations for 5M. (c) Calculated EELS spectra for total Mn for magnetic and non-magnetic lattice. (d) Experimental Mn $L_{3,2}$ spectra, (e) & (f) are the calculated and experimental EELS spectra of Ni, respectively.*

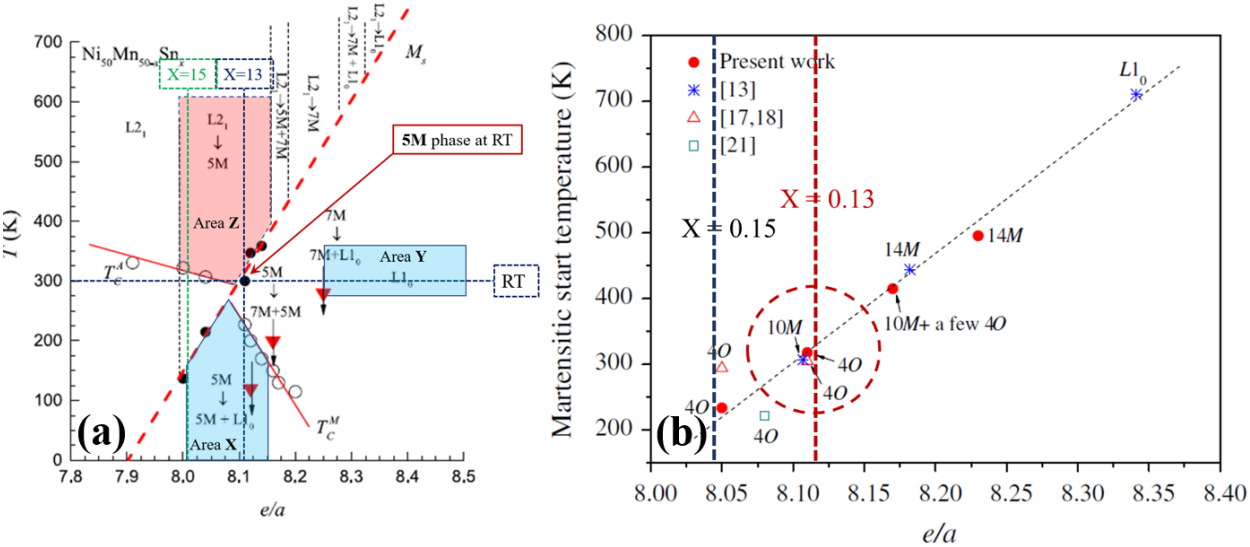

Figure 6.17. *(a) and (b) Experimental Phase diagram of Ni-Mn-Sn Heusler alloys showing the observed structurers and magnetism with respect to the temperature. Copyright 2015 by Elsevier [22].Copyright 2013 by Elsevier [25].*

Among three different martensitic phases observed in the microstructure $L1_0$ is the most dominant (40%). The calculated DOS, EELS spectra for magnetic and non-magnetic calculations and experimental spectra are given in Figure 6.13. From the observation it is clear that the structure may retain some non-magnetic Mn ions on an average length scale and is responsible for overall reduction in the magnetization observed. For $5M$ non-magnetic component is more compared to other phases present in the film.

6.6 Conclusion

In conclusion, Epitaxial $Ni_{50}Mn_{37/35}Sn_{13/15}$ heusler alloy thin films are grown by PLD. Austenite $L2_1$ grows under tensile strain on sapphire (0001) substrate and favours the formation of predominantly $L1_0$ over other martensite phases below the transition temperature. Remnant austenite is found near interface due to substrate strain effect. Volume fraction of the austenite (~50% $L2_1$) and martensite (~40% $L1_0$, *~5%* $4O$ *and* ~5% $5M$). Both Austenite and martensitic are observed and phase transformation is coherent in nature, these Microstructural phase appearance of based on composition, substrate effect. $L2_1$ is found to be in both modulated and unmodulated co-exist coherently, where unmodulated $L2_1$ is tends towards transforming into $2M$ and $7M$ martensitic phase. Local EELS of Mn and Ni $L_{3,2}$ absorption edges measurement and first principle calculation confirms the presence of both magnetic and nonmagnetic phase in thin film alloy system. EELS and TELNES suggests significant presence non-magnetic phases for $4O$ and $5M$. The results give insights on local magnetic ordering by EELS and help to understand magnetic room temperature refrigeration more efficiently.

6.6 Bibliography

[1] O. Gutfleisch, M. A. Willard, E. Brück, C. H. Chen, S. Sankar, and J. P. Liu, Adv. Mater. **23,** 821 (2011).

[2] V. Pecharsky and K. Gschneidner Jr, J. Magn. Magn. Mater. **167,** L179 (1997).

[3] F.-X. Hu, B.-g. Shen, J.-r. Sun, Z.-h. Cheng, G.-h. Rao, and X.-x. Zhang, Appl. Phys. Lett. **78,** 3675 (2001).

[4] A. Fujita, S. Fujieda, Y. Hasegawa, and K. Fukamichi, Phys. Rev. B **67,** 104416 (2003).

[5] T. Krenke, E. Duman, M. Acet, E. F. Wassermann, X. Moya, L. Mañosa, and A. Planes, Nat. Mater. **4,** 450 (2005).

[6] O. Tegus, E. Brück, K. Buschow, and F. De Boer, Nature **415,** 150 (2002).

[7] M. Wood and W. Potter, Cryogenics **25,** 667 (1985).

[8] K. Gschneidner Jr, V. Pecharsky, A. Pecharsky, and C. Zimm ,Materials science forum: Trans Tech Publ) 69-76 (1999).

[9] V. Provenzano, A. J. Shapiro, and R. D. Shull, Nature **429,** 853 (2004).

[10] Y. Sutou, Y. Imano, N. Koeda, T. Omori, R. Kainuma, K. Ishida, and K. Oikawa, Appl. Phys. Lett. **85,** 4358 (2004).

[11] V. Buchelnikov and V. Sokolovskiy, Phys Met Metallogr+ **112,** 633 (2011).

[12] J. Liu, T. Gottschall, K. P. Skokov, J. D. Moore, and O. Gutfleisch, Nat. Mater. **11,** 620 (2012).

[13] H. Xiaoa, C. Yanga, R. Wanga, L. Xua, G. Liub, and V. V. Marchenkovc, Phy. Lett. A **380**, 3414-3420 (2016).

[14] S. Nikitin, G. Myalikgulyev, A. Tishin, M. Annaorazov, K. Asatryan, and A. Tyurin, Phy. Lett. A **148,** 363 (1990).

[15] O. Tegus, E. Brück, L. Zhang, K. Buschow, and F. De Boer, Physica B: Condensed Matter **319,** 174 (2002).

[16] Y. Q. Zhang and Z. D. Zhang, J. Alloys Compd. **365,** 35 (2004).

[17] E. Sªaºıoglu, L. M. Sandratskii, and P. Bruno, Phys. Rev. B **71,** 214412 (2005).

[18] V. V. Sokolovskiy, V. D. Buchelnikov, M. A. Zagrebin, P. Entel, S. Sahoo, and M. Ogura, Phys. Rev. B **86,** 134418 (2012).

[19] T. Krenke, M. Acet, E. F. Wassermann, X. Moya, L. Mañosa, and A. Planes, Phys. Rev. B **72,** 014412 (2005).

[20] S. Aksoy, M. Acet, P. Deen, L. Mañosa, and A. Planes, Phys. Rev. B **79,** 212401 (2009).

[21] X. Wang, J.-X. Shang, F.-H. Wang, C.-B. Jiang, and H.-B. Xu, J. Magn. Magn. Mater. **355**, 173–179 (2014).

[22] A. Çakır, L. Righi, F. Albertini, M. Acet, and M. Farle, Acta Mater. **99,** 140 (2015).

[23] A. Planes, L. Mañosa, and M. Acet, J. Phys. Condens. Matter **21,** 233201 (2009).

[24] J. Santos, T. Sanchez, P. Alvarez, M. Sanchez, J. L. Sánchez Llamazares, B. Hernando, L. Escoda, J. Suñol, and R. Varga, J. Appl. Phy. **103,** 07B326 (2008).

[25] H. Zheng, W. Wang, S. Xue, Q. Zhai, J. Frenzel, and Z. Luo, Acta Mater. **61**, 4648–4656 (2013).

[26] Z. Wang, E. Guo, C. Tan, X. Tian, W. Cai, and J. Zhu, RSC Adv. **7,** 42866 (2017).

[27] J. Liu, N. Scheerbaum, S. Kauffmann-Weiss, and O. Gutfleisch, Adv. Engin. Mater. **14**, No. 8 (2012).

[28] N. Teichert, A. Auge, E. Yüzüak, I. Dincer, Y. Elerman, B. Krumme, H. Wende, O. Yildirim, K. Potzger, and A. Hütten, Acta Mater. **86,** 279 (2015).

[29] E. Yüzüak, I. Dincer, Y. Elerman, A. Auge, N. Teichert, and A. Hütten, Appl. Phys. Lett. **103,** 222403 (2013).

[30] B. Loukya, P. Sowjanya, K. Dileep, R. Shipra, S. Kanuri, L. Panchakarla, and R. Datta, J. Cryst. Growth **329,** 20 (2011).

[31] R. Sahu, D. Radhakrishnan, B. Vishal, D. S. Negi, A. Sil, C. Narayana, and R. Datta, J. Cryst. Growth **470,** 51 (2017).

[32] R. Sahu, H. B. Gholap, G. Mounika, K. Dileep, B. Vishal, S. Ghara, and R. Datta, physica status solidi (b) **253,** 504 (2016).

[33] D. Negi, B. Loukya, K. Ramasamy, A. Gupta, and R. Datta, Appl. Phys. Lett. **106,** 182402 (2015).

[34] D. Negi, H. Sharona, U. Bhat, S. Palchoudhury, A. Gupta, and R. Datta, Phys. Rev. B **95,** 174444 (2017).

[35] P. Blaha, K. Schwarz, G. K. H. Madsen, D. Kvasnicka, and J. Luitz, WIEN2k (Vienna University of Technology, Vienna, Austria, 2001).

[36] J. P. Perdew, K. Burke, and M. Ernzerhof, Phys. Rev. Lett. **77**, 3865 (1996).

[37] B. Krumme, A. Auge, H. C. Herper, I. Opahle, D. Klar, N. Teichert, L. Joly, P. Ohresser, J. Landers, and J. Kappler, Phys. Rev. B **91,** 214417 (2015).

[38] C. Hébert, Micron **38,** 12 (2007).

[39] K. Dileep, R. Sahu, S. Sarkar, S. C. Peter, and R. Datta, , J. Appl. Phys. **119** (11), 114309 (2016).

[40] Y. Zhang, L. Zhang, Q. Zheng, X. Zheng, M. Li, J. Du, and A. Yan, Sci. Rep. **5,** 11010 (2015).

[41] P. J. Shamberger and F. Ohuchi, Phys. Rev. B **79,** 144407 (2009).

[42] P. J. Brown, A. P. Gandy, K. Ishida, R. Kainuma, T. Kanomata, K.-U. Neumann, K. Oikawa, B. Ouladdiaf, and K. R. A. Ziebeck, J. Phys. Condens. Matter **18 (7),** 2249 (2006).

[43] S. Kaufmann, R. Niemann, T. Thersleff, U. K. Rößler, O. Heczko, J. Buschbeck, B. Holzapfel, L. Schultz, and S. Fähler, New J. Phys. **13,** 053029 (2011).

[44] D. C. Dunand and P. Müllner , Adv. Mater., **23** (2), 216-232 (2011).

[45] A. Auge, N. Teichert, M. Meinert, G. Reiss, A. Hütten, E. Yüzüak, I. Dincer, Y. Elerman, I. Ennen, and P. Schattschneider, Phys. Rev. B **85,** 214118 (2012).

[46] B. Loukya, D.S. Negi, K. Dileep, N. Kumar, J. Ghatak, R. Datta, J. Magn. Magn. Mater. **345,** 159-164 (2013).

[47] M. Ye, A. Kimura, Y. Miura, M. Shirai, Y. T. Cui, K. Shimada, H. Namatame, M. Taniguchi, S. Ueda, K. Kobayashi, R. Kainuma, T. Shishido, K. Fukushima, T. Kanomata, Phys. Rev. Lett. **104,** 176401 (2010).

Chapter 7

Future Perspectives

*This chapter outlines the important conclusions drawn from the present thesis. Our contributions towards the growth of MoS_2, WS_2, ReS_2 epitaxial thin films and various types of van der Waals heterostructure summarized. Important role of substrate induced chemically stabilized epitaxial wurtzite-BN thin film and application as hard material. Role of Sb dopant at different site in thermoelectric SnTe to improve z*T. *Microstructural and magnetic details of Heusler compound $Ni_{50}Mn_{37/35}Sn_{13/15}$ thin film for room temperature refrigeration. Subsequent section discusses the promising future of the TMDs, w-BN, thermoelectric and Heusler compound in the context of the recent application based development.*

7.1 Summary of the Thesis

There are three different aspects covered in this thesis. First one is on growth of TMDs, van der Waals (vdW) heterostructure and BN. Second one is on understanding role of dopant Role of Sb dopant at different site in thermoelectric SnTe to improve *z*T. Third one is on Microstructural and magnetic details of Heusler compound $Ni_{50}Mn_{37/35}Sn_{13/15}$ thin film for room temperature refrigeration. The salient features of the work are listed below;

1- We have made significant contributions on the important role of growth of large area MoS_2, WS_2, ReS_2 and van der Waals epitaxial thin films. This work has significant contributions through the thesis of Rajib sahu [1,2]. Complete control over number of layers including monolayer is grown by pulsed laser deposition utilizing slower growth kinetics. Layer numbers is controllable and are 2H in nature for MoS2 and WS_2, whereas ReS_2 has grown vertically [3].

2- MoS_2, WS_2 films grown on c-plane sapphire show stiffening of A_{1g} and E^1_{2g} phonon modes with decreasing number of layers for both MoS_2 and WS_2. HRTEM shows how Mo-Al interaction; indicating 1.11% compression strain Mo-Al interaction shows red shift of E^1_{2g}whereas $A_{1g}$is almost constant because of compression stain. This observed stiffening translate into the compressive strain of 0.52 % & 0.53 % with accompanying increase in fundamental direct band gap to 1.74 and 1.68 eV for monolayer MoS_2 and WS_2, respectively. Band gap is increased for monolayer MoS_2 and WS_2 due to compressive strain. DFT is well agreed with experimental band gap showing increased direct BG for MoS_2 and indirect for WS_2 (ML). the results demonstrate a practical route to stabilize and engineer strain for this class of material over large area device fabrication [2].

3- ReS_2 thin films tend to grow with $(0001)\,ReS_2 \perp (0001)Al_2O_3$ and $(0001)ReS_2 \perp (0001)MoS_2 \parallel (0001)Al_2O_3$ at deposition temperature below 300 °C. Films are polycrystalline grown at temperature above 300°C. The smoothness and epitaxial quality of the films are significantly improved when grown on MoS_2 template compared to sapphire substrate. The results show that PLD is suitable to grow ReS_2 thin film over large area (10×10 mm^2) for practical device application. The results demonstrate a practical route over large area device fabrication. For various

application. Film orientation is truncated in [0001] in Lateral stacking. Two distinct emission peaks are observed at around 1.67 and 1.47 eV with some variation in peak position for different films. Though the films are not monolayer but observing peaks corresponding to both monolayer and multilayers may be because of film orientation which is truncated 0001 plane and presence of both interlayer layer coupling and decoupling effect [3].

4- We have made significant contributions on the important role of growth by PLD can be used to grow large area and TMDs and BN based vdW heterostructure. The layer numbers of TMDs and BN spacer can be controlled by PLD. The nature of BN is grown on MoS_2, WS_2, ReS_2 and three different structure of BN (hexagonal, cubic and wurtzite) depending on the TMDs template layer formation confirmed by Raman. TEM confirms the formation of heterostructure of TMDs with different layers. PL spectra is dominated by 534 nm (2.321 eV) and 580 nm (2.137 eV) for homo-stacks and for hetero stacks heterostructures respectively [4-5].

5- We also able to form of single phase large area epitaxial *wurtzite*-BN thin film on c-plan Al_2O_3 substrate by PLD. *w*-BN has grown under relatively low temperature and pressure condition. Metastable *w*-BN phase is stabilized due to the selective interaction between O and B inducing staggering in the *h*-BN. *w*-BN thin film with hardness value of 37 GPa has potential application in tooling and microelectronic industry [6].

6- We also able to study of microstructural details with help of first principle calculation in low thermal conducting thermoelectric $Sn_{1-x}Sb_xTe$. Results are based observation of superlative structure in $Sb_{0.15}$, which scatters phonon and reduce lattice thermal conductivity. Sb incorporation SnTe lattice can takes place both at the substitutional Sn sites and Te anti-sites. Sb at Sb_{Sn}+Sb_{Te} is energetically more stable than Sb_{Sn}. Phonons are scattered strongly from modulated structure as evident from the strong diffused streak and 2D disordering in the ED pattern of $Sb_{0.15}$ composition. first principle calculation reveals that the areas with Sb_{Sn} large thermo-power, whereas the regions with Sb_{Sn}+Sb_{Te} combination forming superstructure are contributing towards low lattice thermal conductivity and the combined effect increases the zT to ~1 (for

$Sb_{0.15}$). The results give deep insights on Role of Sb dopant at different site in thermoelectric SnTe to improve *zT* [7].

7- We also able to study of the study of Microstructure and magnetic study Heusler alloy ($Ni_{50}Mn_{37/35}Sn_{13/15}$) thin films with help of local EELS measurement and first principle calculation, to understand magnetic ordering in observed various phases of HA. Results confirm the presence of substrate stain effects volume fraction of the austenite ($L2_1$) and martensite ($L1_0$, $4O$ *and* $5M$). Local EELS measurement and first principle calculation confirms the presence of both magnetic and nonmagnetic phase in thin film alloy system. The results give insights on local magnetic ordering by ELLS and help to understand magnetic room temperature refrigeration more efficiently [8].

7.2 Future Perspectives

Recently there have been substantial advancement in the field of thin film growth of 2D materials for electronic, optoelectronic, energy, photocatalytic, HER, and various device applications [9-12]. Making the subject more strong and advanced in both experimental and theoretical aspect. *w*-BN as a new material thin film open to explore. For Thermoelectric materials have various application such as wearable energy conversion devices to provide electricity for portable electronics have attracted increasing attention with the available of novel low-power portable equipment [13-14]. For Heusler alloy thin films have various possibilities for magnetic refrigeration device, actuators, sensors etc. [15-16]. Our future prospectives are;

6.2.1 MoS_2, WS_2, ReS_2 thin film and vdW heterostructure

There are tremendous of scopes in the 2D transition metal dichalcogenides field after our lage area growth of TMDs and CQW vdw heterostructure [1-5]. Now our aim is to study;

- Various device measurement (electronic, optoelectronic, energy, photocatalytic etc.) MoS_2, WS_2, thin film will give better understanding of PLD grown films.
- HER and photocatalytic measurement of vertically grown ReS_2.
- Theoretical understanding of vertical ReS_2 on flat MoS_2 by DFT.
- Life time measurements of excitons.
- Low temperature PL measurements.

- Optimizing the growth process for complete uniformity on the substrate.
- Fabrication of device for optoelectronic and solar based on such heterostructures
- Theoretical understanding of indirect exciton in all homostack and heterostack CQW, MQW vdw heterostructure by DFT.

7.2.2 Metastable *wurtzite*-BN thin film

This the first ever mono-phase wurtzite-BN thin film reported ever [6]. We solve two major problem for any thin film growth epitaxial growth of material with high lattice mismatch and we able to chemically stabilize it. Since *w*-BN is new material with extraordinary properties such as hard material, ultra-wide band gap, thermal and chemical resistant, there are various application for the wurtzite-BN thin film;

- *w*-BN is new material with extraordinary properties such as hard material, ultra-wide band gap, thermal conductive similar to diamond and more chemical resistant 1300°C compare to 800 °C of diamond [17]. *w*-BN have potential of ***alternative of diamond thin film***.
- *w*-BN as a new material thin film with almost all electronic properties is open to exploring.
- Lattice thermal conductivity measurement for thermal management in thin film devices.
- *w*-BN with high hardness and ultra-high band gap have possibility in Surface acoustic wave (SAW) devices.
- Surface thrust study of *w*-BN coating will be useful in tooling, engine pistols industry.
- Fabrication of device for optoelectronic and solar based of TMDs on *w*-BN template.

7.2.3 Thermoelectric ($Sn_{1-x}Sb_xTe$):

- Our finding is very important depends on dopant sites, which extra understanding of point defect to planer defect and superstructure formation. This helps thermoelectric on phonon scattering [7]. We already explain the phonon response from the electron diffraction pattern. On the extended note, the extensive study of phonon can be done by EELS with more precision from the local areas as well as the site [18-19]. This will give an even better understanding of the $Sn_{1-x}Sb_xTe$ and can be extended for any other thermoelectric.

- SnTe has the potential for topological material [20-21]. Theoretically $Sn_{1-x}Sb_xTe$ can provide the possibility of topological material with varying the concentration of Sb. This scientific problem can be studied by first-principle DFT calculation.

7.2.4 Heusler alloy thin film:

Room temperature magnetic refrigeration is a new highly efficient and environmentally protective technology [1-2, 22-23].

- The TELNESS (theoretical DFT) spectra from the unoccupied orbital of Ni or Mn at different site, and the help of experimental local EELS, it will give the understanding of origin of the elemental and orbital spin of the system. The method is already reported by D. S. Negi *et al.* [24-25].
- Selection of another substrate (e.g. MgO, SiO_2) to avid substrate strain in thin film.
- Reversibility and entropy measurements will suggest the overall efficiency of the HA thin film.

7.3 Bibliography

[1] R. Sahu, p-Doping and Valence Band Engineering of ZnO and Epitaxial Growth, Optical Properties, and Alloys of Transition Metal Dichalcogenides (2017).

[2] R. Sahu, D. Radhakrishnan, B. Vishal, D. S. Negi, A. Sil, C. Narayana, R. Datta, J. Cryst. Growth **470,** 51–57 (2017).

[3] B. Vishal, H. Sharona, U. Bhat, A. Paul, M. B. Sreedhara, V. Rajaji, S. C. Sarma, C. Narayana, S. C. Peter, and R. Datta, Thin Solid Films, **685,** 81–87 (2019).

[4] U. Bhat, R. Singh, B. Vishal, A. Sharma, S. Horta, R. Sahu, R. Datta, Phys. Status Solidi B **255,** 1700691(2018).

[5] B. Vishal, U. Bhat, H. Sharona, A. Mukherjee and R. Datta, Heterostructures of hetero-stack of 2D TMDs (MoS_2, WS_2 and ReS_2) and BN, *Manuscript under review*, Bulletin of Materials Science (2020).

[6] B. Vishal, R. Singh, A. Chaturvedi, A. Sharma, M.B. Sreedharaa, R. Sahu, U. Bhat, U. Ramamurty, and R. Datta, Superlattices and Microstructures, **115**, 197-203 (2018).

[7] B. Vishal, R. Sahu, U. Bhat and R. Datta, J. Appl. Phys, **122(5)**, 055102 (2013).

[8] B. Vishal, U. Bhat, H. Sharona, A. Mukherjee, S. Roy, S. C. Peter, and R. Datta,, *Manuscript Under review*, J. Cryst. Growth (2020).

[9] H. S. S. Ramakrishna Matte, A. Gomathi, Arun K. Manna, Dattatray J. Late, R. Datta, S. K. Pati, and C. N. R. Rao, Angew. Chem. **122**4153 –4156 **(**2010).

[10] S. B. Desai, S. R. Madhvapathy, A. B. Sachid, J. P. Llinas, Q. Wang, G. H. Ahn, G. Pitner, M. J. Kim, J. Bokor, C. Hu, H.-S. P. Wong, A. Javey, Science **354,** 6308 (2017).

[11] Y.-C. Lin, H.-P. Komsa, C.-H.Yeh, T.Bjorkman, Z.-Y. Liang, C.-H. Ho, Y.-S. Huang, P.-W. Chiu, A. V. Krasheninnikov, K. Suenaga, ACS Nano **9**, 11(2015).

[12] L. Wang, Z. Sofer, J. Luxa, D. Sedmidubský, A. Ambrosi, M. Pumera, Electrochem. Commun. **63**, 39-43 (2016).

[13] K. Biswas, J. He, I.D. Blum, C.I. Wu, T.P. Hogan, D.N. Seidman, V.P. Dravid, M.G. Kanatzidis, Nature **489**, 414 (2012).

[14] G. Tan, L.-D. Zhao, and M. G. Kanatzidis, Chem. Rev **116,** 12123 (2016).

[15] O. Gutfleisch, M.A. Willard E. Brück, C.H. Chen, S. Sankar, and J. P. Liu , Adv. Mater **23,** 821-42 (2011).

[16] T. Krenke, E. Duman, M. Acet, E.F. Wassermann, X. Moya, L. Mañosa and A. Planes , Nature materials **4,** 450 (2005).

[17] P.W. May, Philosophical Transactions of the Royal Society of London. Series A: Mathematical, Physical and Engineering Sciences, **358** (1766), 473-495 (2000).

[18] J. L. Wilkes, R. E. Palmer, and R. F. Willis., Journal of Electron Spectroscopy and Related Phenomena, 44.1, 355-360 (1987).

[19] Ph. Lambin, J. P. Vigneron, and A. A. Lucas, Physical Review B **32**, 8203 (1985).

[20] Y. Tanaka, Zhi Ren, T. Sato, K. Nakayama, S. Souma, T. Takahashi, K. Segawa, Yoichi Ando, Nature Physics **8**, 800–803 (2012).

[21] T. H. Hsieh, H. Lin, J.Liu, W. Duan, A.Bansil, L. Fu, Nature Communications **3**, 982 (2012)

[22] B.F. Yu, Q. Gao, B. Zhang, X.Z. Meng, Z. Chen, International Journal of Refrigeration **26** 622–636 (2003).

[23] K.A.Gschneidner Jr. V.K. Pecharsky, international journal of refrigeration **31**, 945–961 (2008).

[24] D.S. Negi, B. Loukya, K. Ramasamy, A. Gupta, and R. Datta, Applied Physics Letters, **106** (18), 182402 (2015).

[25] D.S. Negi, H. Sharona, U. Bhat, S. Palchoudhury, A. Gupta, and R. Datta, Physical Review B, **95** (17), 174444 (2017).